Lifetime Measurements of Excited States in ^{163}W and the Properties of Multiparticle Configurations in ^{156}Lu

Thesis submitted in accordance with the requirements of
the University of Liverpool for the degree of Doctor in Philosophy
by

Michael Christopher Lewis

November 2019

"Scientists are not dependent on the ideas of a single man, but on the combined wisdom of thousands of men, all thinking of the same problem, and each doing his little bit to add to the great structure of knowledge which is gradually being erected."

Ernest Rutherford

Acknowledgements

I wish to thank Prof. David Joss for his supervision during my studies, his enthusiasm has been ceaseless and he has always encouraged me in my research. I would also like to thank Prof. Robert Page, who provided valuable expertise and guidance on many occasions.

I am grateful to the STFC for providing the financial support that enabled me to conduct this research. Thank you to everyone at the University of Jyväskylä Accelerator Laboratory, who made sure that the experiments ran smoothly. I would like to thank all of my collaborators, especially Dr. David Cullen, Dr. Michael Giles and Liam Barber for their close collaboration on the lifetime analysis.

Many thanks goes to Dr. Bahadir Sayğı, who always found the time to answer my numerous questions and provided much guidance for the analysis. I would also like to thank Dr. Eddie Parr for his feedback on my thesis chapters and for offering many useful tips regarding data analysis.

A big thank you goes to my fellow Ph.D students, thank you for the welcome curries, the Christmas meals and all the memories over the past four years. In particular, I would like to thank Andy Briscoe, Muneerah Al-Aqeel, Josh Hilton, Tom Calverley and everyone I spent time with on the many trips to Jyväskylä, who made going to experiments a joy. Finally, I would like to thank my family, who I can always rely on for support.

Abstract

The single-particle and collective excitation properties of neutron-deficient $A \sim 160$ nuclides have been measured in fusion-evaporation reactions at the University of Jyväskylä Accelerator Laboratory.

Lifetimes of excited states have been measured using the recoil distance Doppler-shift method employing the JUROGAM II spectrometer and the DPUNS differential plunger. The behaviour of the $B(E2)$ ratios in ^{163}W is found to be consistent with the predictions of the collective model and can be understood in terms of the core polarising effect of the $i_{13/2}$ neutron orbital. This result has provided insights into the discrepancy between observed $B(E2)$ ratios and collective model predictions for heavy even-even transitional nuclei and supports a geometrical origin for these anomalous $B(E2)$ ratios. The results of this work have been published as an article in Physics Letters B.

Excited states in the neutron-deficient nuclide ^{156}Lu have also been measured in a separate experiment. Gamma-ray emissions from a multiparticle spin-trap isomeric state have been measured using the GREAT spectrometer at the focal plane of the RITU separator. The half-life and excitation energy of the isomer above the yrast 10^+ state have been measured. Transitions have been placed into the level scheme based on a γ-ray coincidence analysis, which has indicated that the $[\pi h_{11/2} \otimes \nu f_{7/2}]_{9^+}$ state lies 62 keV above the $[\pi h_{11/2} \otimes \nu h_{9/2}]_{10^+}$ state. The relative ordering of the lowest-lying 9^+ and 10^+ states is inverted in ^{156}Lu compared with its odd-odd isotones. The results of this work have been published as an article in Physical Review C.

Contents

Chapter 1

Introduction

Since the development of the atomic model by Rutherford in 1911 [1], considerable effort has been made to understand the properties of atomic nuclei. Across the nuclear chart, nuclei display a wide variety of phenomena. Despite the complexity and diversity of nuclear phenomena, many of the basic properties of nuclei can be understood with relatively simple models. An early theoretical model of atomic nuclei that found success in explaining nuclear properties was the shell model [2–4], which considered the motion of individual nucleons occupying orbits with quantised angular momentum, in analogy to the shell model of atomic electrons [5, 6]. Excitation of individual nucleons between different orbits successfully explained the structure of γ-ray spectra of nuclei near to closed shells. However, the same could not be said of nuclei far from closed shells and further theoretical models were needed to explain the properties of these nuclei. One such model that accurately describes the behaviour of nuclei far from closed shells is the collective model of Bohr and Mottelson, which considers the motion of the nucleus as a whole [7]. The addition of nucleons to closed-shell configurations leads to a departure from a spherical shape with a deformation along one axis of the nucleus. Such nuclei are depicted in Fig. 1.1. It was recognised that γ-ray spectra of many nuclei could be understood in terms of a rotation of the nucleus about an axis perpendicular to the deformation axis. Furthermore, many nuclear phenomena can be understood

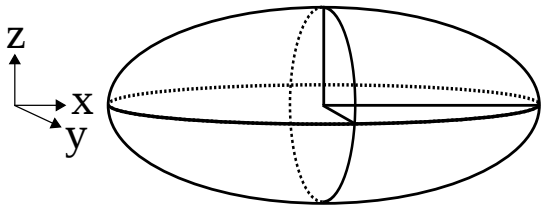

Shape	Number of deformation axes	Side view 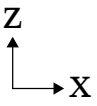	End view 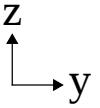
Prolate	1	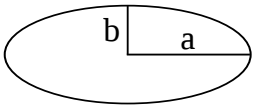	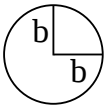
Oblate	1	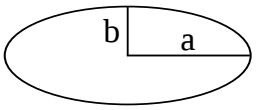	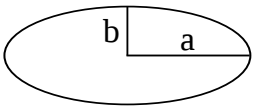
Triaxial	2	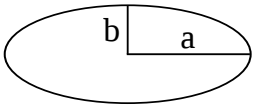	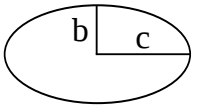

FIGURE 1.1: Definitions of the deformed ellipsoidal shapes available to nuclei. A generic ellipsoid is shown at top. The parameters a, b and c represent lengths of differing magnitude.

by considering the collective motion of the nucleus in tandem with single-particle behaviour.

Excited states in heavy neutron-deficient nuclei above $N = 82$ have been studied extensively. This region of the chart of nuclides is shown in Fig. 1.2. The Nilsson diagram shown in Fig. 1.3 indicates that in these nuclei the Fermi surface is in the vicinity of the $s_{1/2}$, $d_{3/2}$ and $h_{11/2}$ proton orbitals and the $f_{7/2}$, $h_{9/2}$ and $i_{13/2}$ neutron orbitals. The properties of a given nuclide are determined not only by the specific orbitals occupied by valence nucleons, but also the proportion of each proton and neutron shell that is filled. Nuclei in this region are textbook examples of the evolution from single-particle behaviour at the $N = 82$ closed shell to collective behaviour around the midshell at $N = 104$.

The majority of midshell nuclei are interpreted as being deformed along only one axis, and are said to be axially symmetric. Each orbital has a tendency to drive

the nuclear shape towards either a prolate or oblate shape according to the slope of the Nilsson level, which is related to the expectation value of the quadrupole moment

$$\frac{d\epsilon_k}{d\beta} = -\langle k|q|k\rangle, \tag{1.1}$$

where ϵ_k is the energy of the single-particle state $|k\rangle$, β is the deformation parameter and q is the quadrupole operator. Nucleons occupying orbitals inclined in opposite directions therefore produce opposite polarising effects, the competition of which can lead to triaxial deformations. The triaxial deformed shape is depicted in Fig. 1.1. In triaxial or 'axially asymmetric' nuclei, additional deformation axes are introduced. For a given nuclide, a number of different low-lying configurations may exist which possess different shapes. Nuclei with a dynamic degree of triaxiality are said to be γ soft. Gamma-soft deformations tend to arise when protons and neutrons occupy the top and bottom of their shells, respectively, or vice versa [8]. The conditions for γ-soft deformations may therefore be realised in proton-rich $N \sim 90$ nuclei in which the Fermi surfaces are near the top and bottom of the proton $h_{11/2}$ and neutron $i_{13/2}$ subshells, respectively.

Deformed nuclei have nonspherical charge distributions. Consequently, the electromagnetic fields of deformed nuclei have a non-zero electric quadrupole moment, which is reflected in electromagnetic decay patterns. Hence, the measurement of γ-ray emissions and determination of the level structure can reveal details of the nuclear deformation. Lifetimes of excited states are a particularly valuable source of information on the underlying nuclear shape. The $B(E2)$ reduced transition probabilities, which can be extracted from measured lifetimes, are related to the nuclear wavefunctions, which are sensitive to the geometric shapes of nuclei. The lifetimes of excited rotational nuclear states are typically on the order of picoseconds, beyond the timing resolution of currently available detectors [10, 11].

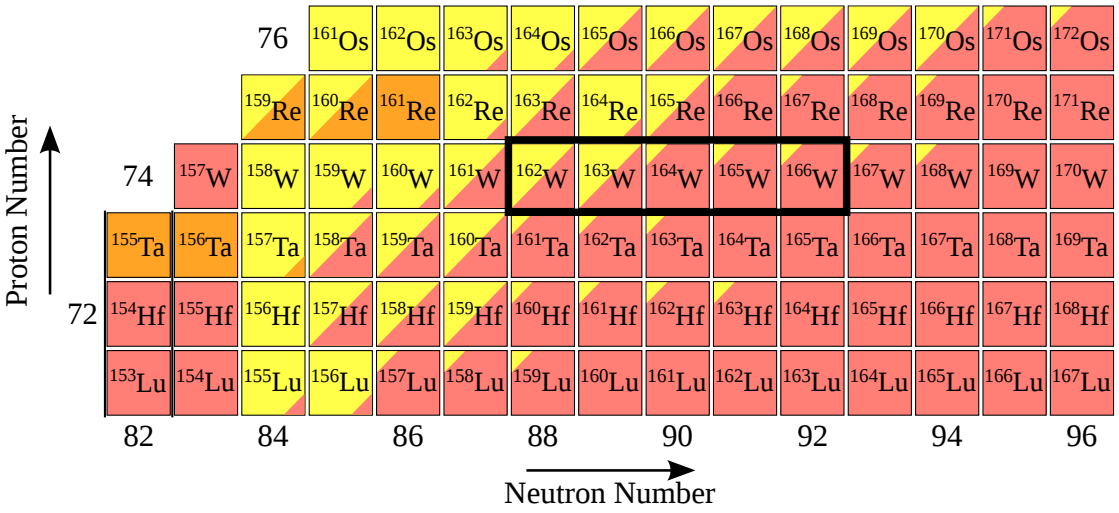

FIGURE 1.2: A section of the chart of nuclides showing heavy neutron-deficient nuclei above $N = 82$. Each nuclide is colour coded according to the known decay branches: α decay (yellow), $\beta+$ decay/EC (red) and proton or double proton decay (orange). A single colour indicates a branching ratio of 100%. Where mixed decay modes occur, coloured triangles are used. The $N \sim 90$ tungsten isotopes are indicated by the black box.

Hence, experimental techniques which do not rely on the timing properties of detectors have been developed to measure the lifetimes of γ-decaying excited states. The recoil distance Doppler-shift (RDDS) technique is an established method of measuring lifetimes of excited states [12]. The use of RDDS in conjunction with recoil-decay tagging (RDT) techniques enables the measurement of lifetimes of excited states in nuclei with low production cross sections, extending the range of nuclei currently accessible to lifetime measurements to the $N \sim 92$ tungsten isotopes.

Spectroscopic studies of the $N \sim 90$ nuclides ^{162}W, ^{164}W and ^{166}W [13, 14] have measured $E(4^+)/E(2^+)$ ratios similar to that predicted for γ-soft nuclei [15]. The presence of γ-soft shapes in this region is also inferred by the signature splitting patterns of rotational bands in the neighbouring even-N Ta ($Z = 73$) [16, 17] and Re ($Z = 75$) [18] isotones. The study of $B(E2)$ reduced transition probabilities of excited states in even-even nuclei in the Os, W, Pt region has revealed apparently anomalous $B(E2)$ ratios [19–21] that are inconsistent with the predictions of the

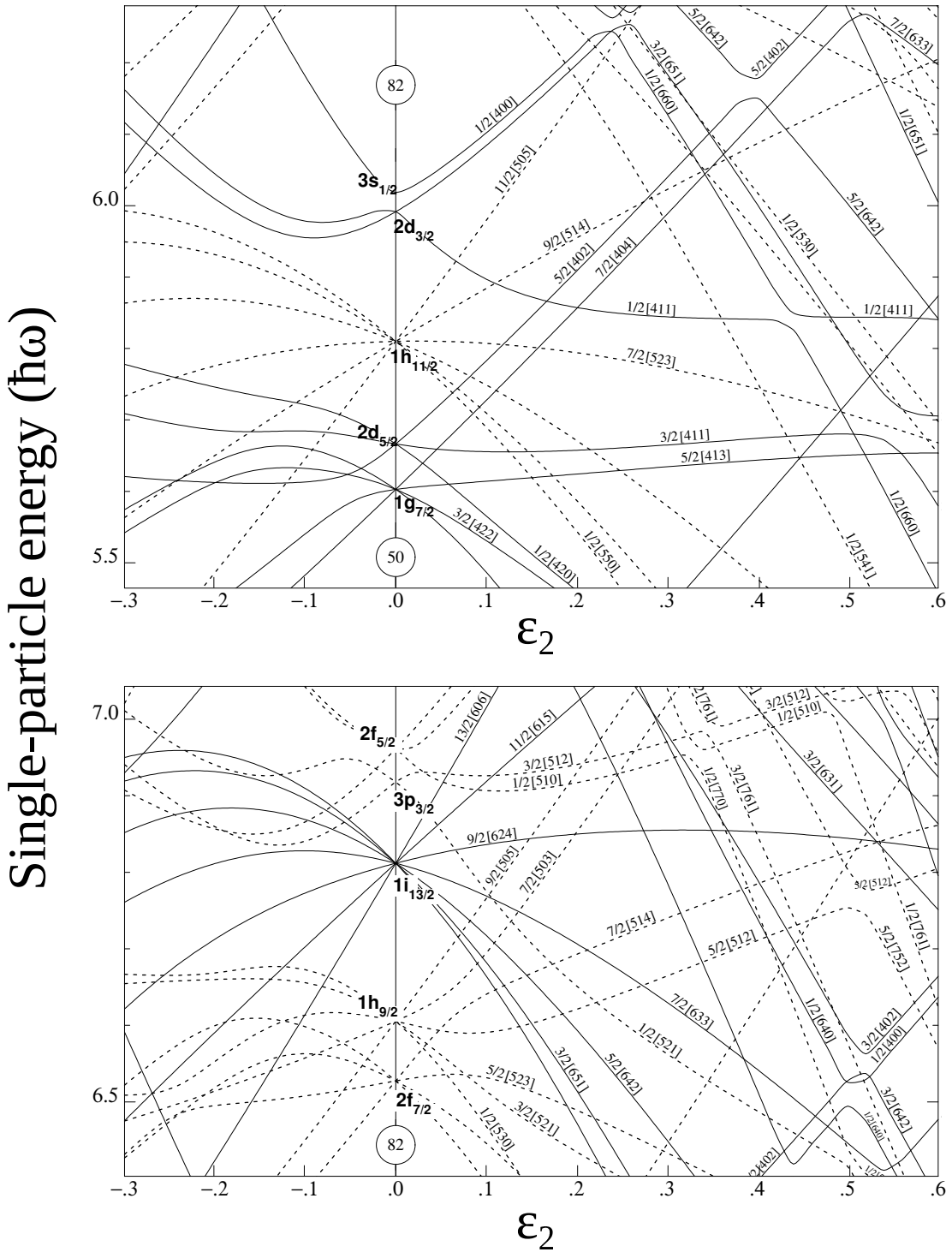

FIGURE 1.3: Nilsson diagrams for protons in the range $50 \leq Z \leq 82$ (top) and neutrons in the range $82 \leq N < 126$ (bottom), which show the variation of single-particle energies with deformation ε [9].

collective model [7]. In the tungsten isotopes, ^{166}W was found to have anomalous $B(E2)$ ratios with a particularly low $B(E2\text{: } 4^+ \rightarrow 2^+)/B(E2\text{: } 2^+ \rightarrow 0^+)$ ratio of 0.33(5) [20]. It has previously been suggested that the anomalous ratios in this region of the nuclear chart could be due to a quantum phase transition between non-collective seniority and collective excitations [21]. However, as noted by Cederwall *et al.*, seniority structures are not expected in these nuclides as they are not in close proximity to a closed shell. Since the $B(E2\text{: } 2^+ \rightarrow 0^+)$ value for ^{166}W is in excess of 100 W.u. the behaviour appears to be collective, and so alternative explanations should be considered.

The apparently anomalous $B(E2)$ ratios in the even-even nuclei raises the question of whether such anomalies exist in odd-A nuclei, where the nuclear shape may be subject to the polarising effects of unpaired nucleons. This work presents the results of lifetime measurements of excited states in the yrast band of the transitional nucleus ^{163}W. $B(E2)$ ratios have been extracted and interpreted in the context of those of the neighbouring tungsten isotopes. A geometric origin for the anomalous $B(E2)$ ratios in ^{166}W is proposed, and may apply to other nearby transitional nuclei. The observed ratio in ^{163}W is explained in terms of the polarisation properties of the unpaired $i_{13/2}$ neutron.

Experimental signatures of triaxial deformations in this region extend to the lutetium isotopes. Spectroscopic studies of the odd-even $^{161–167}$Lu isotopes have revealed triaxial, superdeformed (TSD) rotational bands which display electromagnetic decay patterns indicative of a 'wobbling' motion that is unique to triaxial deformations [7, 22–25]. The existence of three distinct axes provided by the triaxial deformation allows rotation to occur about any of the three axes. In a wobbling nucleus, the axis with the largest moment of inertia is favoured, however the availability of multiple rotational axes allows a proportion of the angular momentum to be transferred away from the principle axis. Wobbling states have not been found in the odd-odd lutetium isotopes, however triaxial deformations are expected as some configurations in ^{164}Lu have local triaxial minima in calculated

potential energy surfaces [26]. TSD bands have been observed in ^{162}Lu [27] and ^{164}Lu [26] which have similar dynamic moments of inertia to those of wobbling bands in ^{163,165}Lu [28–30]. The origin of the triaxial minima has been attributed to large proton and neutron shell gaps in conjunction with the strong deformation inducing effect of the $\pi i_{13/2}$ intruder orbital [28].

It is therefore necessary to understand the evolution of single-particle structures above $N = 82$ entering into this region of triaxiality. The properties of the single-particle orbitals near the Fermi surface in this region can be better understood by studying multiparticle spin-trap isomers generated by the various angular momentum couplings of valence nucleons. Such isomers provide a useful opportunity to constrain the excitation energy of single-particle states. This work presents the results of spectroscopic measurements of the decay of a multiparticle spin-trap isomeric state in ^{156}Lu. Gamma-ray transitions depopulating the isomer have been identified and their paths to an α-decaying 10^+ state have been elucidated. The half-life of the isomeric state has been measured, and through comparison with Weisskopf estimates supports the previous assignment of the isomer as a 19^- state. The results are discussed in the context of the neighbouring $N = 85$ isotones, which reveals that the relative order of the $[\pi h_{11/2} \otimes \nu f_{7/2}]_{9^+}$ and $[\pi h_{11/2} \otimes \nu h_{9/2}]_{10^+}$ states is inverted in ^{156}Lu compared to the neighbouring odd-odd isotones, which can be understood in terms of the attractive interaction between $h_{11/2}$ protons and $h_{9/2}$ neutrons.

Chapter 2

Theoretical Background

2.1 The Nuclear Shell Model

Nuclides are known to show exceptional stability compared to their neighbours when they possess particular numbers of protons and/or neutrons [2–4]. The increased stability at certain proton and neutron numbers is indicative of a shell structure analogous to the structure of atomic electrons [5, 6]. Increased stability occurs when a shell is filled to capacity, with protons and neutrons occupying separate shells. These special numbers of protons and neutrons are referred to as magic numbers. The currently established nuclear magic numbers are 2, 8, 20, 28, 50, 82 and 126[1]. Supporting experimental evidence of the occurrence of magic numbers in nuclei can be found in Ref. [2]. Evidence also supports 40 [32] and 64 [33] as weak magic numbers in some regions of the nuclear chart.

The shell model describes single-particle behaviour where nucleons move independently in the mean field generated by all the other nucleons in the nucleus. The shape of the potential V experienced by a nucleon inside a nucleus is a key feature of the shell model. A realistic potential should correctly predict the magic numbers

[1] 126 has been confirmed as a magic number for neutrons but at present has not been established experimentally for protons, see Ref. [31] for further details.

that are observed in experiment. The infinite square well and harmonic-oscillator potentials are only able to correctly predict the first three shell closures, and they are unrealistic in that they are infinite potentials. A more realistic potential with a shape that follows the density distribution of the nucleus is the Woods-Saxon potential, shown in Fig. 2.1, which has the form

$$V(r) = \frac{-V_0}{1 + \exp(\frac{r-R}{a})}, \tag{2.1}$$

where V_0 is the well depth, R is the mean radius and a is the skin thickness. The single-particle levels calculated for the Woods-Saxon potential shown in Fig. 2.2 again only reproduce the first three magic numbers. The reproduction of the remaining magic numbers requires a modification of the potential to account for the interaction between the orbital angular momentum ℓ and the intrinsic spin angular momentum s of a nucleon [34, 35]. It has become standard practice to label levels according to the notation $N\ell_j$, where N is the principle quantum number, ℓ is the orbital angular momentum[2], and j is the total angular momentum given by $j = \ell \pm 1/2$, since $s = \pm 1/2$ for nucleons. The strength of the spin-orbit interaction is proportional to ℓ and causes an energy splitting between states of equal ℓ but different s. The resulting shifts in the energies of the single-particle levels shown in Fig. 2.2 produce shell gaps at the observed magic numbers.

The shell model is able to make predictions about the properties of nuclei in close proximity to a shell closure. According to the model, the spin of the nucleus as a whole is determined by nucleons occupying partially filled shells. This is because the spins of nucleons in a complete shell pair up such that the net spin is zero. For example, for a nucleus with one neutron in excess of a closed shell, the ground-state nuclear spin would be equal to the j value of the orbital that the unpaired neutron occupies. The spins of nuclei just short of a full shell can also be determined. Each empty orbital below the shell closure is referred to as a hole.

[2] ℓ is commonly written using $s, p, d, f, \ldots$, to indicate $\ell = 0, 1, 2, 3, \ldots$

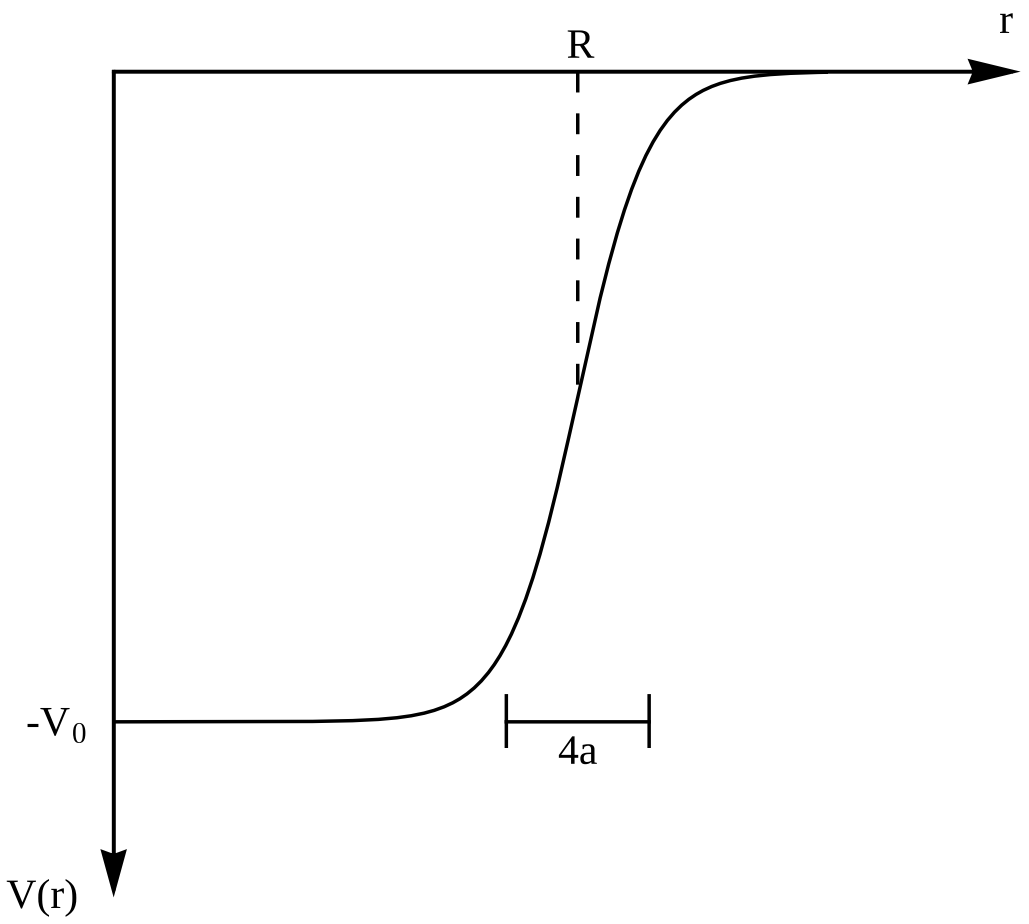

FIGURE 2.1: The Woods-Saxon potential with $V_0 = 50$ MeV, $R = 6.5$ fm and $a = 0.5$ fm [36].

Since a closed shell must have net zero spin, a nucleus with one hole must have a ground state spin equal to the j value of the orbital that the hole occupies. The parity of the ground state of a given nuclide is determined by the ℓ value; even-ℓ levels have positive parity while odd-ℓ levels have negative parity. The shell model has proven accurate for spherical nuclei in the light and medium-heavy range, but is not able to reproduce the spectra of nuclei far from shell closures.

2.2 The Nilsson Model

The Nilsson model [37] predicts single-particle energies for deformed nuclei. The density distribution of a deformed nucleus is assumed to be ellipsoidal with an

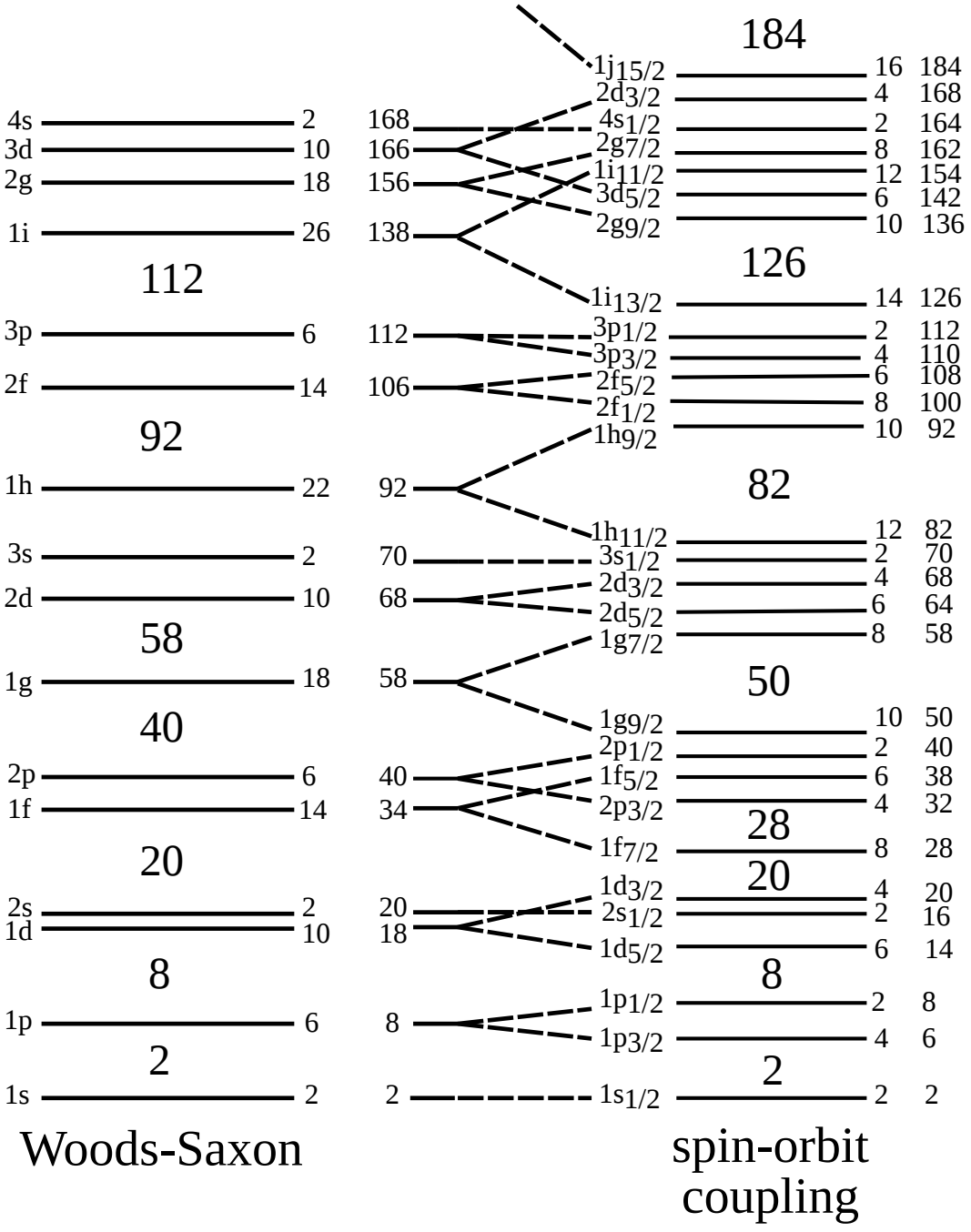

FIGURE 2.2: Single-particle energies calculated using the Woods-Saxon potential without corrections (left) and with the spin-orbit correction (right). Levels are labelled according to the notation $N\ell_j$, where N is the principle quantum number, ℓ is the orbital angular momentum which is written as s, p, d, f, etc, corresponding to $\ell = 0$, 1, 2, 3, etc, and j is the total angular momentum given by $j = \ell + s$. The paired numbers on the right of each level represent, left to right, the number of nucleons that can occupy the level and the cumulative number of nucleons up to and including that level.

average potential that is described using the anisotropic harmonic oscillator

$$V_{AHO} = \frac{1}{2}m(\omega_x^2 + \omega_y^2 + \omega_z^2) \tag{2.2}$$

where $\omega_{x,y,z}$ are the angular frequencies in the x, y and z directions, respectively. Conventionally, the deformation or symmetry axis of axially symmetric nuclei is designated as the z direction, such that the x and y frequencies are equal and may be combined into a single term as $\omega_\perp = \omega_{x,y}$. The magnitude of the deformation may be defined in terms of the angular frequencies according to the deformation parameter

$$\varepsilon = \frac{(\omega_\perp - \omega_z)}{\omega_0}, \tag{2.3}$$

where ω_0 is the average frequency. A positive value of ε corresponds to a prolate shape, while a negative value corresponds to an oblate shape. Each single-particle state has a set of quantum numbers which define its properties. These are the Nilsson labels which are written as

$$\Omega^\pi[Nn_z\Lambda], \tag{2.4}$$

where

Ω = Projection of total angular momentum **J** onto the symmetry axis

π = Parity

N = Oscillator quantum number

n_z = Number of nodes in the wave function along the symmetry axis

Λ = Projection of the orbital angular momentum **L** onto the symmetry axis

Figure. 2.3 depicts the nuclear angular momentum vectors and their projections. The quantum numbers N, n_z and Λ are only good quantum numbers (i.e. their

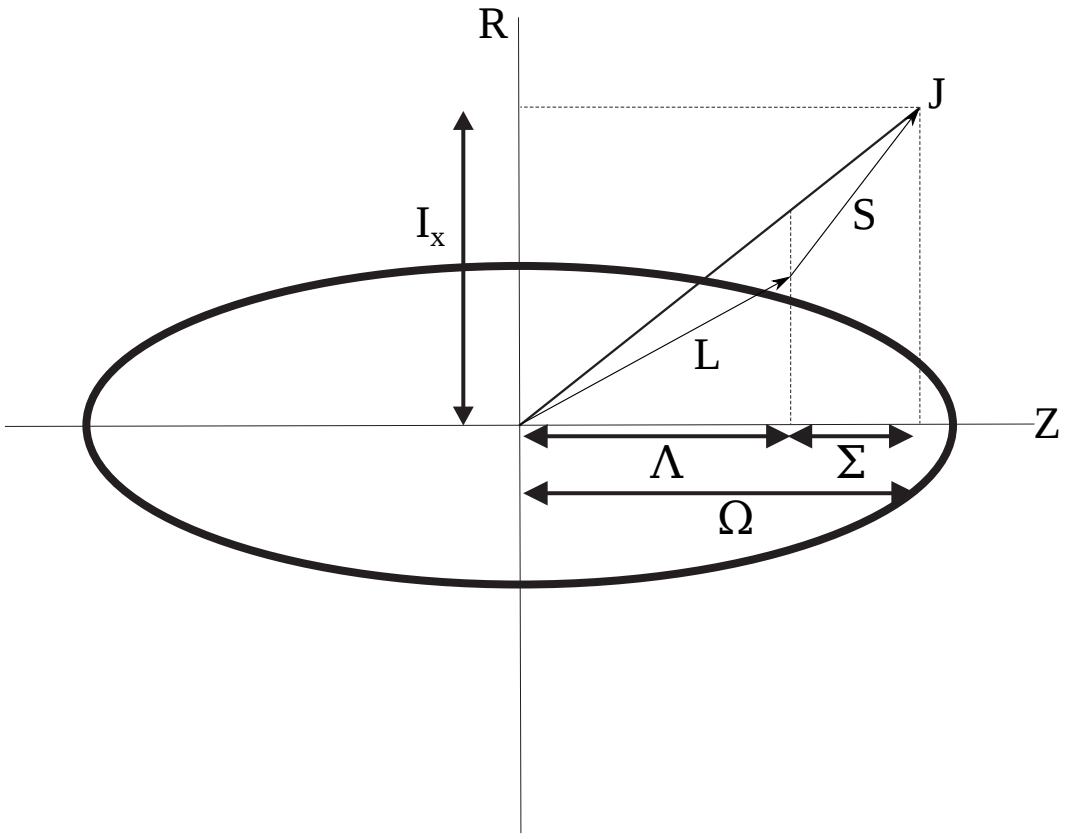

FIGURE 2.3: A schematic diagram defining the projections Λ, Σ and Ω of the orbital (**L**), spin (**S**) and total single-particle (**J**) angular momenta, respectively, on the symmetry axis for an axially deformed nucleus.

operators commute with the Hamiltonian and correspond to conserved quantities) when the deformation is large ($\varepsilon \to \infty$) and are said to be asymptotic quantum numbers. The only good quantum numbers for low and moderate deformations are the projection Ω and the parity π.

Figure 2.4 shows the variation of the single-particle energies with deformation for neutrons in the range $82 \leq N \leq 126$. Positive-parity levels are represented by solid lines while dashed lines indicate negative-parity levels. Each level is doubly degenerate with each nucleon having opposite orientation with $\pm\,\Omega$. The levels are filled according to the Pauli Exclusion principle, with the lowest in energy being filled first.

At $\varepsilon = 0$, each level has a degeneracy of $(2j{+}1)/2$. This degeneracy is lifted

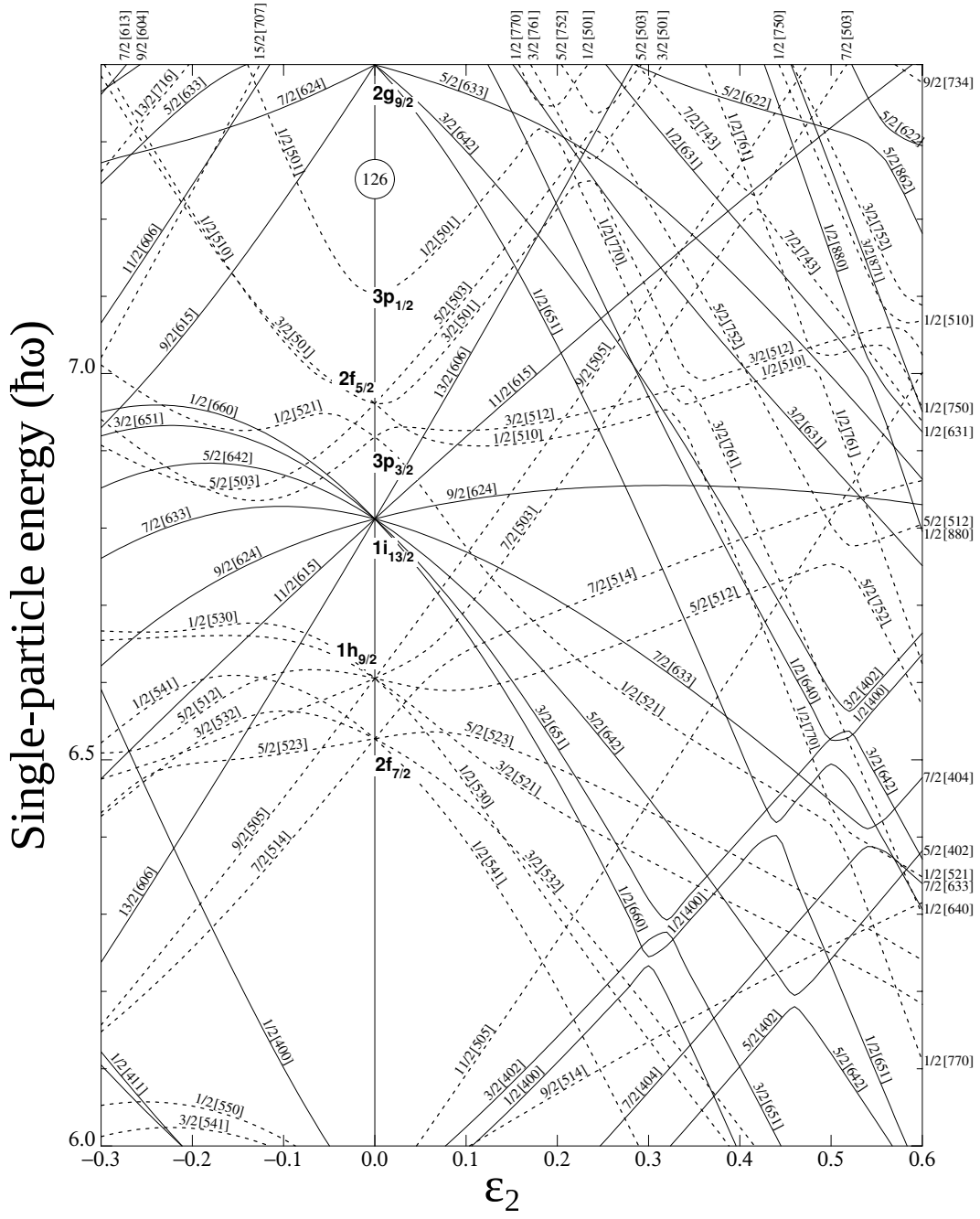

FIGURE 2.4: Nilsson diagram for neutrons in the range $82 \leq N \leq 126$, which gives the variation of single-particle energies with deformation parameter ε [9].

as the nucleus becomes deformed. The deformation introduces configuration mixing, with the quadrupole interaction preferentially mixing configurations that are separated by two units of angular momentum and have the same nucleon spin orientation. The quadrupole interaction determines the order of the levels with respect to Ω; for prolate shapes the lower-Ω levels are shifted to lower energies while for oblate shapes it is the higher-Ω levels that are shifted lower in energy. The ordering can be understood in terms of the orientations of the single-particle orbits. In prolate nuclei, a low-Ω orbit has an orbital plane that strongly overlaps with the spatial distribution of the remaining nucleons. The nuclear force is attractive and therefore a greater overlap results in a lower energy for lower-Ω orbits. In oblate nuclei, the larger overlap with the remaining nucleons occurs for higher-Ω orbits, hence the higher-Ω orbits are lower in energy.

The gradient of the Nilsson levels is related to the expectation value of the quadrupole moment

$$\frac{d\epsilon_k}{d\beta} = -\langle k|q|k\rangle, \tag{2.5}$$

where ϵ_k is the energy of the single-particle state $|k\rangle$, β is the deformation parameter[3] and q is the quadrupole operator. If two levels of the same Ω and π approach each other, they cannot cross due to the Pauli Exclusion principle and instead become mixed and exchange quantum numbers.

The Nilsson model provides a microscopic description of nonrotating, deformed nuclei. Some features of the γ-ray spectra of nuclei can be understood by considering the vibration or rotation of the nucleus as a whole, descriptions of which are given in section 2.3. The Nilsson model predicts the intrinsic structure that rotation may be built on. Certain features of nuclear spectra can be understood by considering the interaction of the intrinsic motion and rotational motion, aspects of which are detailed in section 2.4.

[3]The relation for β is given by equation (2.8) and is related to the alternative deformation parameter ε by the equation $\beta \approx \sqrt{\pi/5}(4/3\varepsilon + 4/9\varepsilon^2)$ [38]

2.3 Collective Models

In the collective model of Bohr and Mottelson, the properties of nonspherical nuclei are a result of the motion of the nucleus as a whole, as opposed to that of single nucleons in the shell model [7]. It provides a macroscopic description of the nucleus that is complementary to the microscopic approach of shell models. There are two main forms of collective behaviour to consider: vibrational and rotational.

2.3.1 Collective Vibration

The shape of a vibrating nucleus is spherical when averaged over time, however at any instant in time the nuclear shape may deviate from spherical. The radial distance of the nuclear surface from the centre is given by

$$R(\theta, \phi, t) = R_0\Big(1 + \alpha_{00} + \sum_{\lambda=1}^{\infty} \sum_{\mu=-\lambda}^{\lambda} \alpha^*_{\lambda\mu}(t) Y_{\lambda\mu}(\theta, \phi)\Big), \tag{2.6}$$

where R_0 is the radius of a sphere with volume equal to that of the nucleus, α_{00} is a constant that is defined such that the volume stays constant for all deformations and $\alpha^*_{\lambda\mu}$ are the amplitudes of the spherical harmonics $Y_{\lambda\mu}(\theta, \phi)$.

A quantum of vibration is known as a phonon, and has a multipolarity λ which quantifies the angular momentum of the vibration. The lowest multipolarity vibrational modes are dipole ($\lambda = 1$), quadrupole ($\lambda = 2$) and octupole ($\lambda = 3$) vibrations. A dipole vibration involves an overall displacement from the nucleus' centre of mass and hence requires external forces to maintain. The quadrupole and octupole vibrations, however, can result from internal nuclear forces. Adding n phonons to the ground state produces vibrational excitation levels with energy equal to $n\hbar\omega$ where ω is the angular frequency of the phonons. The ratio of the excitation energies of the 4^+ and 2^+ states $E(4^+)/E(2^+)$ is predicted by the collective model to be 2.0 in vibrational nuclei. Nuclei which have $E(4^+)/E(2^+) = 2.0$ are known as spherical harmonic vibrators.

2.3.2 Nuclear Rotation

The rotation of a deformed nucleus about an axis perpendicular to the symmetry axis forms a series of states of increasing rotational energy in what is known as a rotational band. For an axially symmetric nucleus, equation (2.6) simplifies to

$$R(\theta, \phi) = R_{av}[1 + \beta Y_{20}(\theta, \phi)]. \tag{2.7}$$

Here, β is the deformation parameter given by

$$\beta = \frac{4}{3}\sqrt{\frac{\pi}{5}}\frac{\Delta R}{R_{av}}, \tag{2.8}$$

where ΔR is the difference between the nucleus' semimajor and semiminor axes.

Classically the energy of a rotating object is given by

$$E = \frac{1}{2}\mathcal{J}\omega^2 = \frac{I^2}{2\mathcal{J}}, \tag{2.9}$$

where $\mathcal{J}$ is the moment of inertia, ω is the angular frequency and I is the total angular momentum. The rotational energy can be transformed into the quantum limit by replacing I^2 with its eigenvalue $\hbar^2 I(I+1)$

$$E = \frac{\hbar^2}{2\mathcal{J}} I(I+1). \tag{2.10}$$

The total angular momentum quantum number I is also referred to as the spin. A deformed nucleus can be excited by adding units of I, which forms a series of states which constitute a rotational band. As a result of nuclear pairing, the ground state for all even-even nuclei is 0^+, and due to the reflection symmetry of even-even nuclei the levels in the ground-state band take on even values of I. Equation (2.10) predicts an $E(4^+)/E(2^+)$ ratio of 3.33 for rotational nuclei. Nuclei which display this energy ratio are known as axially symmetric rotors. Intermediate between spherical harmonic vibrators and axially symmetric rotors are axially *asymmetric*

rotors for which $E(4^+)/E(2^+) = 2.5$ [15]. These nuclei are sometimes referred to as γ-soft nuclei due to the γ parameter not having a rigid value, see section 2.5.

The ability of equation (2.10) to correctly predict excitation energies is limited since $\mathcal{J}$ is not a fixed value. The strong force acts only on a nucleon's immediate neighbours and this short range means that the nucleus does not behave as a rigid body and instead is intermediate between being fluid (weak binding between nucleons) and rigid. Additionally, there is an increase in the moment of inertia as angular momentum increases, an effect known as centrifugal stretching.

The state of a nucleus is described by the wavefunction, which for deformed nuclei has a rotational component given by

$$|\psi\rangle_{rot} = |IMK\rangle = \sqrt{\frac{2I+1}{8\pi^2}} D^I_{MK}(\Theta, \Phi, \Psi), \tag{2.11}$$

where M and K are the projections of the angular momentum onto the z axis in the laboratory frame and onto the symmetry axis in the nuclear frame, respectively, and D^I_{MK} are the rotation matrices for a rotation through (Θ, Φ, Ψ). The dependence of the wavefunction on K is of particular importance in the present study.

Rotational bands can be built upon states with different intrinsic structures. The state that a rotational band is built on is known as an intrinsic state. For example, a rotational band can form with a vibrational state or a pair-breaking particle excitation as its band head. In odd-A nuclei, the unpaired nucleon can occupy a number of Nilsson levels, forming the band head for a rotational band. The single-particle angular momentum of the unpaired nucleon and the rotational angular momentum interact with each other, the consequences of which are considered in the following section.

2.4 Coriolis Effects on Angular Momentum Coupling

In odd-A nuclei, the total angular momentum $\mathbf{I}$ is formed from the vector sum of the collective rotational angular momentum $\mathbf{R}$ and the single-particle angular momentum $\mathbf{j}$. The rotational Hamiltonian in this case is given by the expression

$$H_{rot} = \frac{\hbar^2}{2\mathcal{J}}\mathbf{R}^2 = \frac{\hbar^2}{2\mathcal{J}}(\mathbf{I}-\mathbf{j})^2 = \frac{\hbar^2}{2\mathcal{J}}(\mathbf{I}^2+\mathbf{j}^2-2\mathbf{I}\cdot\mathbf{j}). \tag{2.12}$$

Frequently the rotational Hamiltonian is written in terms of the raising and lowering operators $\mathbf{I}_\pm$[4] and $\mathbf{j}_\pm$ [5] as in the following expression, where eigenvalues have been used in place of operators where applicable

$$E(I) = \frac{\hbar^2}{2\mathcal{J}}\Big[I(I+1) - 2K^2 + \langle\mathbf{j}^2\rangle - (\mathbf{I}_+\mathbf{j}_- + \mathbf{I}_-\mathbf{j}_+)\Big], \tag{2.13}$$

where K is the projection of I onto the symmetry axis. The final two terms in the square brackets are combined into one term known as the Coriolis interaction

$$V_{Coriolis} = -\frac{\hbar^2}{2\mathcal{J}}(\mathbf{I}_+\mathbf{j}_- + \mathbf{I}_-\mathbf{j}_+). \tag{2.14}$$

The nuclear Coriolis interaction is analogous to the classical Coriolis effect for a projectile moving in a rotating reference frame. According to observers in the rotating reference frame there is an apparent deflection of the projectile from its actual path. This deflection is known as the Coriolis effect. In the nuclear case, the Coriolis interaction results from the interplay of the rotational and single-particle angular momenta and causes different K values to mix.

[4] $\mathbf{I}_\pm = \mathbf{I}_x \pm i\mathbf{I}_y$, indices indicate the angular momentum in the direction of the respective axes.
[5] $\mathbf{j}_\pm = \mathbf{j}_x \pm i\mathbf{j}_y$

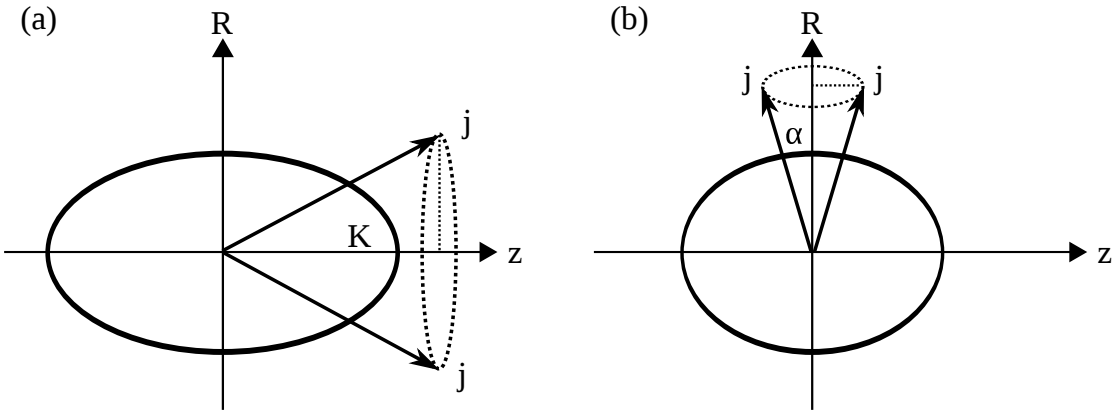

FIGURE 2.5: (a) Strong coupling scheme. The single-particle angular momentum is aligned with the deformation axis. (b) Decoupled scheme. The single-particle angular momentum is aligned with the rotation axis **R**.

The relative strength of the Coriolis interaction has consequences for the spin sequences observed in rotational bands in odd-A nuclei. In the case of well-deformed nuclei, the Coriolis term in equation (2.13) is negligible and solutions to the Hamiltonian conserve the projection K [39]. This situation is referred to as the strong coupling scheme, in which **j** precesses around the symmetry axis as shown in Fig. 2.5(a) and K is well defined. Bands following this scheme are characterised by transitions connecting states with $\Delta I = \pm 1$.

The Coriolis interaction increases with spin I, so at high spin the Coriolis interaction may no longer be negligible. The Coriolis interaction can also be significant at low spin and can occur when the Fermi surface is in close proximity to low-Ω orbitals of a unique parity j shell. This occurs in prolate nuclei when the j shell is nearly empty and in oblate nuclei with a nearly full shell, i.e. in transitional nuclei where the deformation is relatively small. Stephens *et al.* noted that the negative-parity rotational bands based on an $11/2^-$ isomer in odd-A La isotopes have a similar spin sequence and similar excitation energies to those in the ground-state bands of the neighbouring even-N Ba isotopes with one less proton and interpreted this as being due to a Coriolis effect which results in a new coupling scheme in which the projection of **j** on the rotation axis, α, is a good

quantum number [40, 41]. The level excitation energies in this case are given by the expression

$$E(I,\alpha) = const. + \frac{1}{2\mathcal{J}}(I-\alpha)(I-\alpha+1)$$
$$= const. + \frac{1}{2\mathcal{J}}R(R+1).$$

Hence, the lowest lying states are those that are maximally aligned $\alpha = j$ states, and these are known as favoured states. Typically the states with lower alignment (unfavoured states) have greater excitation energies such that they are not populated in a heavy-ion fusion-evaporation reaction. The core rotates with $R = I\text{-}\alpha$, with $\Delta I = 2$ between connecting states, hence the level sequence shares characteristics with that of the even-even core. The Coriolis effect causes **j** to precess around the rotation axis, and as a result K constantly changes and is no longer a good quantum number. Although K is not conserved, averaged over time $K = 0$. A schematic of this coupling scheme, which has become known as the decoupled scheme, is shown in Fig. 2.5(b).

2.5 Nuclear Shapes

The nuclear surface can be defined according to equation (2.6). It is useful to transform the coordinate system to one in which the coordinate axes correspond to the axes of the nucleus. A quadrupole deformation ($\lambda = 2$) can be completely described with only the parameters a_{20}, a_{2-2} and the Euler angles, where a_{20} and a_{2-2} are the α_{20} and α_{2-2} of the new coordinate system. The Euler angles describe the orientation only and do not need to be considered here. It is useful to introduce the Hill-Wheeler variables β and γ [42] which are defined in the following equations

$$a_{20} = \beta\cos\gamma, \tag{2.15}$$

$$a_{22} = \frac{\beta}{\sqrt{2}} \sin\gamma. \tag{2.16}$$

At a given time $R(\theta, \phi)$ can be written in terms of β and γ

$$R(\theta,\phi) = R_0\Big\{1 + \beta\sqrt{5/16\pi}\Big[\cos\gamma(3\cos^2\theta - 1) + \sqrt{3}\sin\gamma\sin^2\theta\cos 2\phi\Big]\Big\}. \tag{2.17}$$

The variable β gives the magnitude of the deformation while γ gives the degree of axial asymmetry. For $\beta \geq 0$, the axially symmetric prolate shapes occur at $\gamma = 0°$, 120° and 240°, while axially symmetric oblate shapes occur at $\gamma = 60°$, 180° and 300°. For $\gamma \neq n60°$, where n is an integer, the nucleus takes on a triaxial deformation. It is unnecessary to consider the whole range of γ values, as nuclear shapes are repeated with the only difference being their relative orientation. Some orientations are however distinct from each other when considering the direction of the rotation axis. When the rotation axis coincides with the symmetry axis, the rotation becomes quantum mechanically indefinable and is therefore distinguishable from rotation about axes perpendicular to the symmetry axis. When rotation occurs about the symmetry axis, the shape is referred to as a non-collective prolate or oblate shape. The range of γ can be reduced to -120° $\leq \gamma \leq$ 60° whilst still distinguishing between collective and non-collective quadrupole shapes in what is known as the Lund convention [43], which is shown in Fig. 2.6.

A nucleus does not necessarily have to adopt a single fixed shape. If the potential energy surface is relatively flat with respect to γ, i.e. there is no clearly defined minimum to constrain γ, the nuclear shape can oscillate between certain limits of γ deformation. A nucleus possessing a γ deformation that does not take on a fixed value is referred to as a γ-soft nucleus.

Soft-triaxial nuclear deformations can occur when the valence protons and neutrons are located at the top and bottom of their shells, respectively, or vice

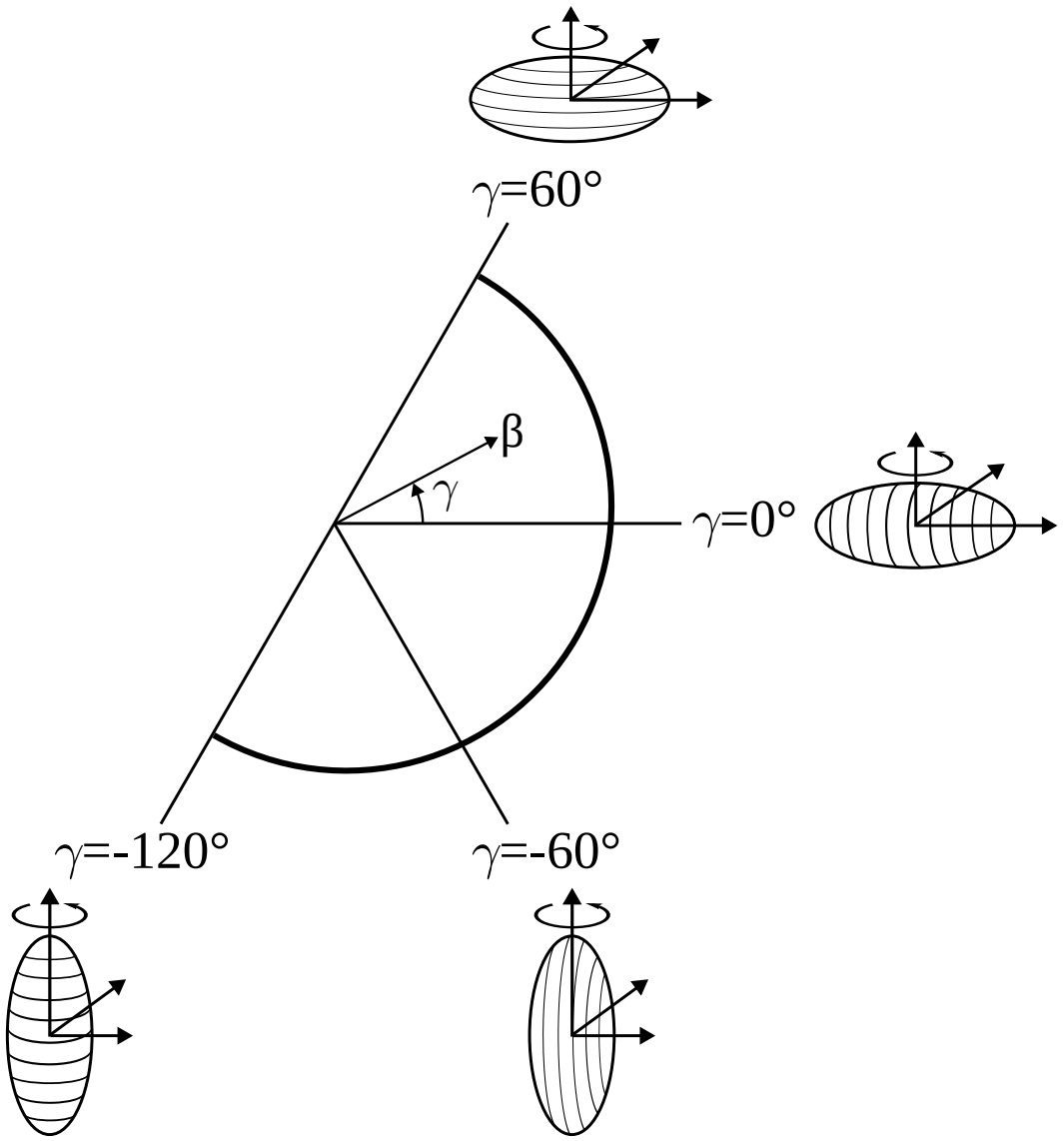

FIGURE 2.6: The Lund convention for rotating quadrupole shapes [43].

versa [8]. In this configuration, one type of nucleon will occupy downward sloping Nilsson orbitals which for positive β drive the nucleus to a prolate shape while the other type occupies upward sloping orbitals, driving the nucleus towards an oblate shape. Hence the competition between these opposing effects results in axial asymmetry.

The lack of axial symmetry causes the projection of the total angular momentum I onto the symmetry axis K to become ill defined, as the shape is constantly changing so that no clearly defined symmetry axis is conserved in time. A result of this is that for γ-soft nuclei, the predictions of the collective model have

limited validity for variables which depend on the projection of the total angular momentum onto the symmetry axis.

2.6 Electromagnetic Transitions

A nucleus in an energetically excited state may release energy in the form of electromagnetic radiation by emission of a photon or by directly transferring energy to one of the atomic electrons which is subsequently released from the atom and is known as a conversion electron. The excited states in nuclei are quantised and so transitions from one state to a lower-energy state produce photons with discrete energies. The process of γ-ray emission must obey the law of angular momentum conservation. For initial and final states with angular momentum $\mathbf{I}_i$ and $\mathbf{I}_f$, respectively, the angular momentum of the emitted γ ray L must follow the relation

$$|I_i - I_f| \leq L \leq I_i + I_f, \tag{2.18}$$

where the angular momenta are in units of $\hbar$ and L takes on integer values [44]. L is frequently referred to as the multipolarity of the γ ray, where a transition which emits a γ ray with multipolarity L is known as a 2^L-pole transition.

There are two polarisations of γ ray that can be emitted by a nucleus: electric and magnetic. Which type is emitted depends on the parities of the initial and final states, π_i and π_f, as well as the multipolarity of the transition. The γ ray will be electric in character if $\pi_i \cdot \pi_f = (\text{-}1)^L$, whereas the γ ray will be magnetic if $\pi_i \cdot \pi_f = (\text{-}1)^{L+1}$. Electric transitions are associated with a change in the charge distribution of the nucleons in the nucleus, whereas for magnetic transitions there is a change in the current distribution.

Nuclei existing in a specific excited state remain in that state for a mean lifetime τ. The mean lifetime and the width Γ of the decay are related by the equation

$$\Gamma\tau = \hbar. \tag{2.19}$$

The probability of decay from an excited state to some lower state is proportional to Γ. This probability depends on the matrix element describing the mode of decay joining the initial and final states. Therefore

$$\Gamma \propto |\langle\psi_f|\hat{O}_{decay}|\psi_i\rangle|^2, \tag{2.20}$$

where $|\psi_i\rangle$ and $|\psi_f\rangle$ are the nuclear wavefunctions describing the initial and final states respectively, and $\hat{O}_{decay}$ is the quantum-mechanical operator for the mode of decay. Considering the system to be subject to a potential V and a weak perturbing potential V', it is the perturbing potential that allows the decay from the initial state in a finite amount of time. The transition rate T is given by Fermi's golden rule

$$T = \frac{2\pi}{\hbar}|V'_{fi}|^2\rho(E_f), \tag{2.21}$$

where V'_{fi} is the expectation value of V' and $\rho(E_f)$ is the density of final states. V'_{fi} is often referred to as the matrix element for the transition. Hence, the measurement of lifetimes allows information to be gained on the matrix elements and can be used to verify nuclear models.

The transition rate T for the emission of a γ ray from a given state is

$$T_{fi}(\sigma L) = \frac{8\pi(L+1)}{\hbar L((2L+1)!!)^2}\left(\frac{E_\gamma}{\hbar c}\right)^{2L+1} B(\sigma L, I_i \rightarrow I_f), \tag{2.22}$$

where σ indicates whether the γ ray is electric or magnetic, L is the multipolarity of the emitted γ ray, E_γ is the γ-ray energy and $B(\sigma L,\ I_i \rightarrow\ I_f)$ is the reduced transition probability, defined as

$$B(\sigma L, I_i \rightarrow I_f) = \frac{1}{2I_i+1}|\langle\psi_f||\hat{O}_{decay}||\psi_i\rangle|^2. \tag{2.23}$$

TABLE 2.1: Weisskopf estimates for electric and magnetic γ-ray transition rates (s^{-1}) in terms of mass number A and transition energy E_γ (MeV).

Electric Transitions	Magnetic Transitions
$T(E1) = 1.0\times10^{14}A^{2/3}E_\gamma^3$	$T(M1) = 3.1\times10^{13}E_\gamma^3$
$T(E2) = 7.3\times10^{7}A^{4/3}E_\gamma^5$	$T(M2) = 2.2\times10^{7}A^{2/3}E_\gamma^5$
$T(E3) = 34A^{2}E_\gamma^7$	$T(M3) = 10A^{4/3}E_\gamma^7$
$T(E4) = 1.1\times10^{-5}A^{8/3}E_\gamma^9$	$T(M4) = 3.3\times10^{-6}A^{2}E_\gamma^9$
$T(E5) = 2.4\times10^{-12}A^{10/3}E_\gamma^{11}$	$T(M5) = 7.4\times10^{-13}A^{8/3}E_\gamma^{11}$

Rotational bands are characterised by a series of $E2$ transitions between states of the band. Using $L = 2$ in equation (2.22) and accounting for internal conversion, the relation can be rearranged into the form

$$B(E2 : I \rightarrow I-2) = \frac{0.0816}{\tau E_\gamma^5(1+\alpha)}, \tag{2.24}$$

where $B(E2\text{: } I_i \rightarrow I_f)$ has units of e^2b^2, E_γ is in units of MeV and τ is in units of ps and is related to T by $\tau = 1/T$. Hence measurements of the excitation energies and lifetimes of excited states allows the reduced transition probability to be calculated.

The Weisskopf unit (W.u.) has become a standard unit for reduced transition probabilities [45]. The Weisskopf estimates assume that out of all of the nucleons in the nucleus, only one proton participates in the transition, so by comparing the Weisskopf estimates to measured reduced transition probabilities the level of collectivity can be assessed, with collective transitions being significantly greater than 1 W.u. In transitions between rotational states, the $B(E2)$ value can reach up to values greater than 1000 W.u., see for example Ref. [46]. The Weisskopf estimates are shown for the lower multipolarities in Tab. 2.1.

2.7 Alpha Decay

In heavy nuclei the emission of an α particle becomes a significant decay mode. This is a consequence of the Coulomb repulsion experienced by protons, which increases in strength at a faster rate than the nuclear force as protons are added to the nucleus.

Within the reference frame of a nucleus A that decays by emission of an α particle into the nuclear species B, conservation of energy requires that

$$m_A c^2 = m_B c^2 + E_B + m_\alpha c^2 + E_\alpha, \tag{2.25}$$

where m are the masses of the respective nuclei, c is the speed of light and E are the respective kinetic energies. The Q value is defined as the total energy released as a result of the decay

$$Q = (m_A - m_B - m_\alpha)c^2 = E_B + E_\alpha. \tag{2.26}$$

If Q is greater than zero the decay can happen spontaneously. From the conservation of linear momentum and using $E = p^2/2m$ (the daughter and α energies are typically non-relativistic), E_α can be written in the form

$$E_\alpha = \frac{Q}{(1 + \frac{m_\alpha}{m_B})}. \tag{2.27}$$

Using the mass number A for the daughter nucleus and the mass number for the α particle, the equation can be rearranged into the form

$$E_\alpha = Q\frac{(A-4)}{A}. \tag{2.28}$$

Figure 2.7 shows the potential experienced by an α particle depending on its distance r from the centre of a nucleus. At a distance $r < r_A$ the α particle is within the interior of the nucleus where the nuclear force dominates. At distances

$r > r_A$, the α particle is beyond the influence of the short range nuclear force and only the Coulomb and centrifugal interactions are significant. In this region the potential is typically modelled as

$$V(r) = \frac{2(Z-2)e^2}{4\pi\epsilon_0 r} + \frac{\hbar^2 l(l+1)}{2mr^2}, \tag{2.29}$$

where Z is the proton number of the parent nucleus, e is the elementary charge, ϵ_0 is the permittivity of free space and l and m are the angular momentum and the mass of the α particle, respectively [47, 48]. The terms on the right-hand side of equation (2.29) represent the Coulomb and centrifugal potentials, respectively. For an α particle with a given energy there exists a potential barrier in the range $r_A < r < r_B$ which classically is forbidden for the α particle to traverse but in quantum mechanics the wavefunction leaks into this region and the α particle can tunnel through the barrier. If the α particle reaches $r > r_B$ it has escaped from the nucleus and the parent nucleus has decayed.

The α particle is said to be preformed in the nucleus and moves within the interior, encountering the potential barrier at the nuclear surface. The width of the barrier and its height relative to the energy of the α particle determines on average how many attempts the α particle requires to penetrate the barrier, which then determines the half-life of the nucleus. The half-life also depends on the probability of preformation of an α particle, P_{pre}, and the frequency with which the α particle encounters the potential barrier, f. Therefore the decay probability λ is given by

$$\lambda = f \cdot P_{barrier} \cdot P_{pre}, \tag{2.30}$$

where $P_{barrier}$ is the barrier penetration probability. The emitted α particle has an energy and half-life characteristic of the transition of the decaying nucleus. Knowledge of the energy and half-life of a particular α decay allows for the recoil-decay tagging technique to be applied, in which the probable nuclear species of the

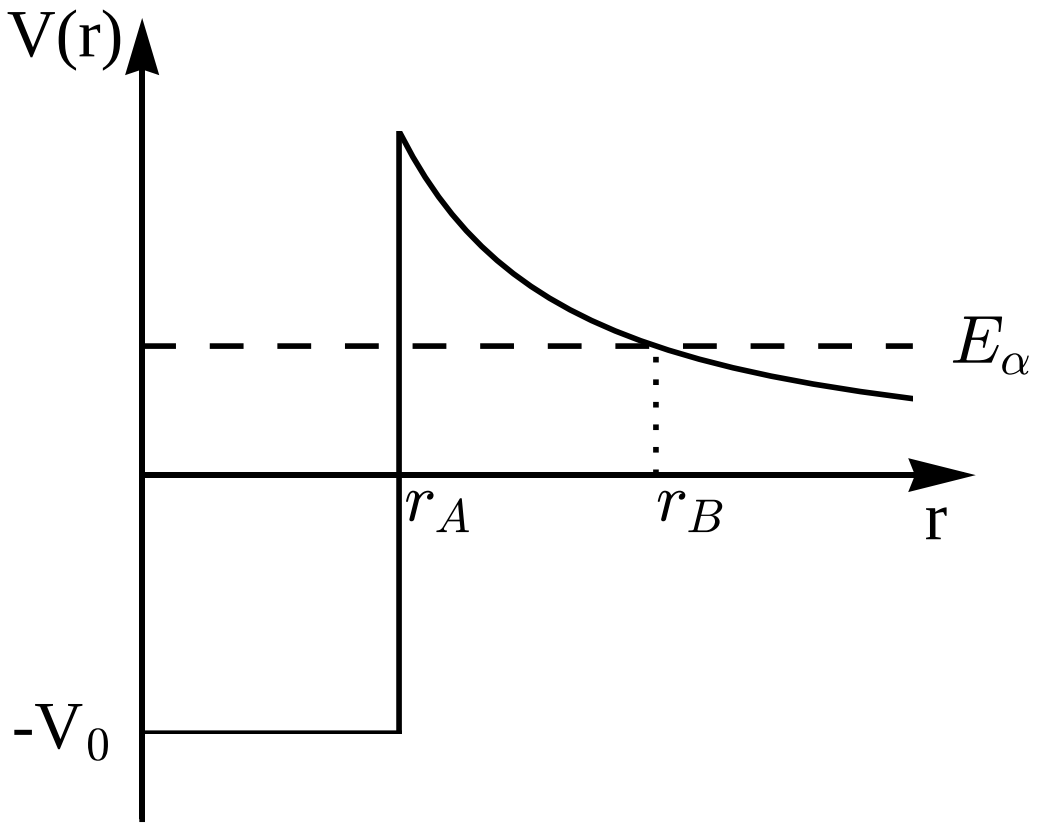

FIGURE 2.7: Potential energy between an α particle and the residual nucleus as a function of the α particle's radial distance from the centre of the nucleus.

decaying nucleus is determined by matching the observed decay energy and half-life to that of a known α decay. The recoil-decay tagging technique is described further in section 3.6.

From α-decay theory it is possible to calculate the half-life expected for even-even nuclei [47, 48]. In nuclei with an unpaired proton or neutron or one of each, α decay is hindered compared to the decay of even-even nuclei. The half-life measured in an experiment $t_{1/2}^{exp}$ and the theoretical half-life expected assuming an even-even nucleus $t_{1/2}^{theo}$ are used to define the hindrance factor:

$$F = \frac{t_{1/2}^{exp}}{t_{1/2}^{theo}}. \tag{2.31}$$

Since $t_{1/2}^{theo}$ has no dependence on the nuclear structure of the emitting nucleus, the hindrance factor gives an indication of the effects of nuclear structure on the decay process.

Chapter 3

Experimental Methodology and Apparatus

3.1 Heavy-Ion Fusion-Evaporation Reactions

Heavy-ion fusion-evaporation reactions are frequently used in nuclear physics experiments to produce short-lived, proton-rich nuclei. The heavy ions collide with target nuclei and form a single fused system consisting of both target and incident nuclei [49]. The beam of incident heavy ions must be energetic enough to overcome the Coulomb barrier, and so the compound nucleus that is formed has a substantial amount of excitation energy and angular momentum. Bulk material is used for the target to ensure that there is a significant probability of a nuclear reaction occurring. When studying nuclei with low production cross sections, thin targets are employed to allow the reaction products to recoil into devices that use electric and/or magnetic fields to physically separate unreacted beam and the reaction products.

Figure 3.1 shows the deexcitation process of a compound nucleus following formation in a fusion-evaporation reaction. In the first stage, a sequential evaporation of nucleons from the nucleus takes place. Particle evaporation ceases when

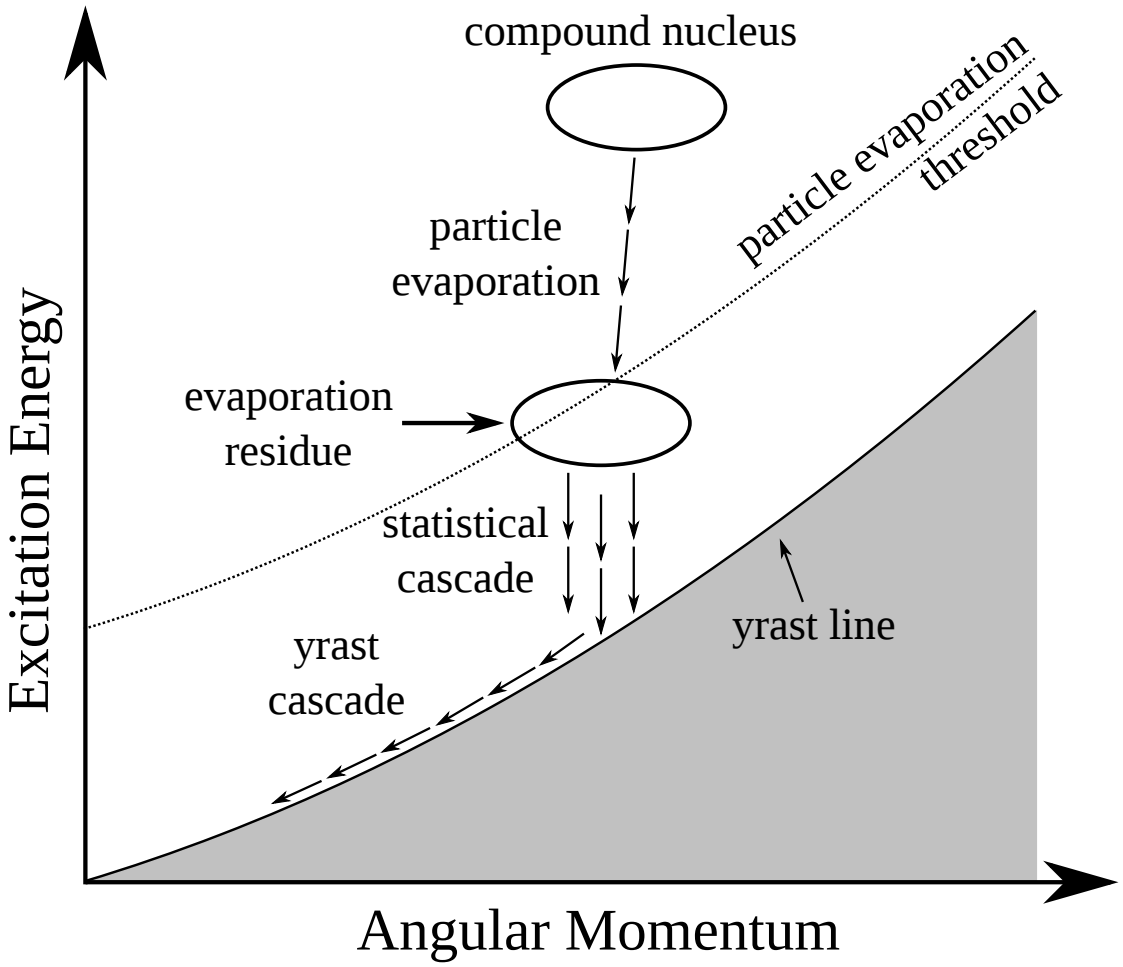

FIGURE 3.1: De-excitation of a compound nucleus following a fusion-evaporation reaction.

the excitation energy of the nucleus is below the particle-evaporation threshold. The nucleus formed at the end of this process is referred to as the evaporation residue. A γ-ray cascade follows, which consists of a statistical cascade and an yrast cascade. The statistical $E1$ transitions (electric transition of multipole order $L = 1$) remove large quantities of energy but only a few units of angular momentum. At a given angular momentum there exists a nuclear state below which there are no further states. Such states form what is known as the yrast line. Upon reaching the yrast line, the nucleus decays via $E2$-transitions, which are dependent on nuclear structure and hence enable the nuclear structure to be studied. The angular momentum dissipates significantly at this stage of deexcitation until the ground state is reached.

3.2 The JUROGAM II Spectrometer Array

JUROGAM II is an array of escape-suppressed hyper-pure germanium (HPGe) detectors. A schematic diagram of the array is shown in Fig. 3.2. JUROGAM II detects prompt γ rays emitted following heavy-ion fusion-evaporation reactions. It comprises of 15 EUROGAM Phase I detectors [50] and 24 EUROGAM II Clover detectors [51] grouped into rings of detectors at fixed polar angles with respect to the beam direction. The angular positions and number of detectors in each ring are detailed in Tab. 3.1. The Phase I detectors have a single Ge crystal each, whereas each Clover detector has four crystals. The shift in the detected energy ΔE due to Doppler broadening is given by

$$\Delta E = \frac{v}{c}\sin(\theta)\Delta\theta, \tag{3.1}$$

where v/c is the reaction fragment velocity, θ is the angle of detection relative to the beam direction and $\Delta\theta$ is the opening angle of the detector. Hence, the higher granularity of the Clover detectors reduces Doppler broadening as the opening angle of the detector is smaller. Clover detectors are used at angles close to 90° as the Doppler broadening effect maximises at this angle. The whole JUROGAM II array is reported to have a photopeak efficiency of 7% at 1332 keV [51]. Each detector is Compton suppressed using a bismuth germanate (BGO) detector. Any signal that is detected in the germanium detector simultaneously with a signal in the corresponding BGO detector is discarded. Compton scattering of γ rays from one germanium detector into another can be accounted for by taking the sum of the energy deposited in each detector to be the full energy of the original γ ray. This process in known as add-back and has been employed in the present analysis.

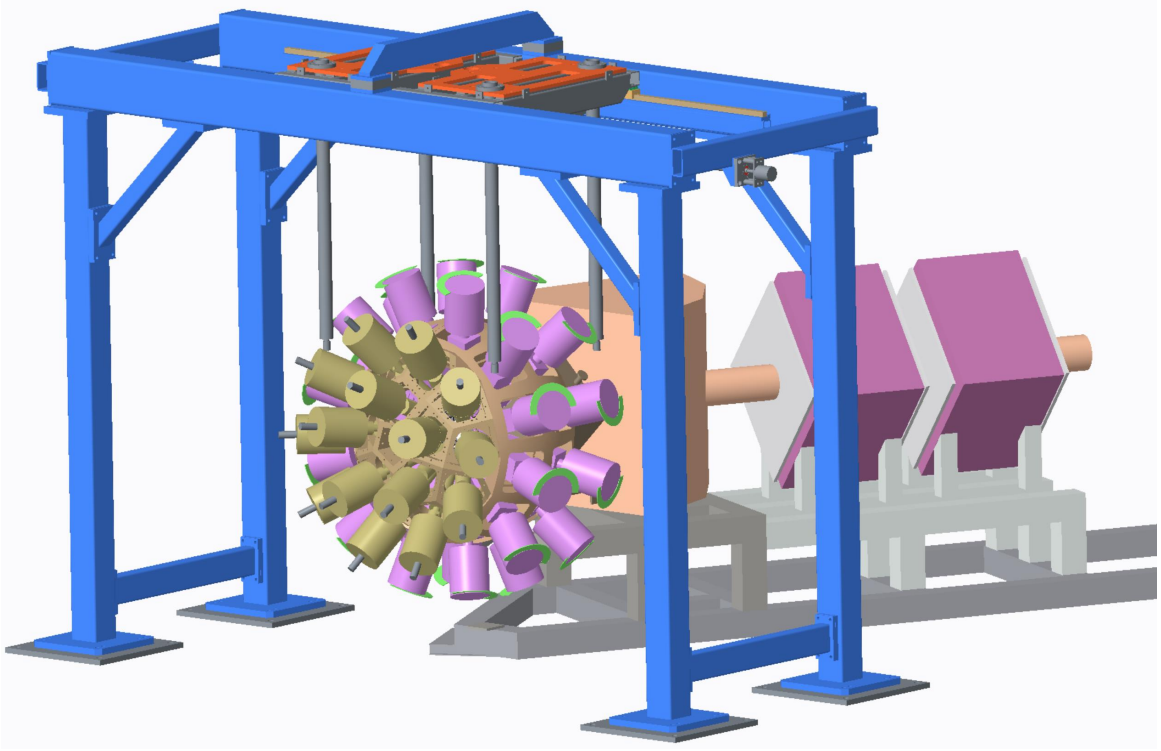

FIGURE 3.2: Schematic diagram of JUROGAM II (left) at the entrance to RITU (right). The beam enters from the left of the figure and impinges on a target placed at the centre of JUROGAM II. Gamma rays emitted by reaction products are detected by JUROGAM II, before the reaction products are transmitted through RITU. Courtesy of Dave Seddon.

TABLE 3.1: JUROGAM II detector angles relative to the beam direction.

Ring	Detector angle (°)	Type of detectors	Number of detectors
1	157.6	Phase I	5
2	133.57	Phase I	10
3	104.5	Clover	12
4	75.5	Clover	12

3.3 The RITU Separator

Nuclei populated in fusion-evaporation reactions recoil away from the target and into the gas-filled separator Recoil Ion Transport Unit (RITU) [52]. RITU separates unreacted beam and fission products from the fusion products, and the fusion products from each other. One dipole (D) and three quadrupole (Q) magnets are arranged in a QDQQ configuration. The separation of the fusion products is achieved by the dipole magnet, while the quadrupole magnets focus the evaporation residues onto the focal plane DSSDs of the GREAT spectrometer. The quadrupole upstream of the dipole magnet is employed to improve matching of the evaporation-residue cone to the dipole acceptance.

RITU is a He gas-filled separator that transports all reaction products in an average charge state to the focal plane. Reaction products of a given species acquire an average charge state independent of their initial charge distribution via the exchange of electrons between reaction products and the filler gas, a process known as charge state focussing [53]. Hence, a greater proportion of the reaction products are collected in comparison with vacuum-mode separators, which typically collect only a few charge states. The increase in transmission efficiency is at the expense of mass resolution which is reduced compared to vacuum-mode separators. The magnetic rigidity $B\rho$ for a gas-filled separator with a dipole magnet is given by

$$B\rho = 0.0227\frac{A}{Z^{1/3}}, \tag{3.2}$$

where B is the magnetic field and ρ is the radius of curvature for an ion with mass number A and atomic number Z. Although the magnetic rigidity provides poor separation between reaction products and primary beam for symmetric reactions, the separation is sufficient for asymmetric reactions such as those employed in the present study.

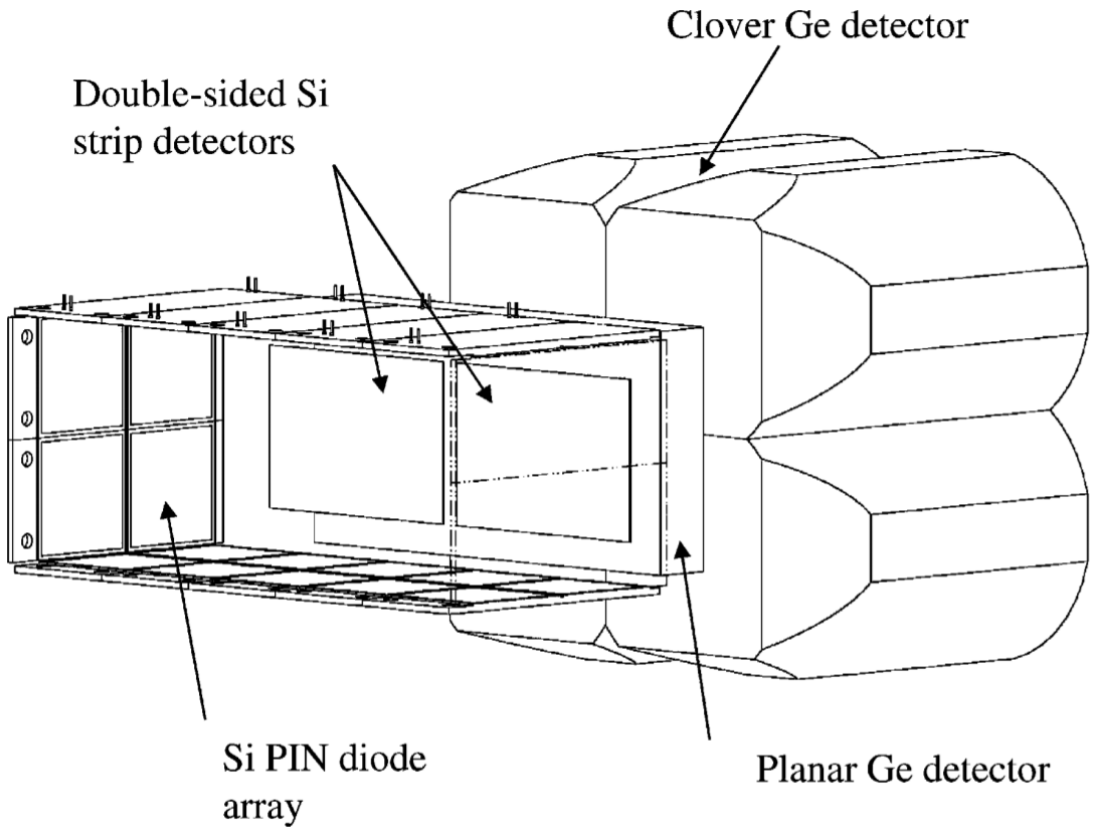

FIGURE 3.3: Schematic diagram of GREAT. One clover detector of a possible five is shown. The MWPC is not shown. Taken from Ref. [54].

3.4 The GREAT Spectrometer

Following their flight through RITU, evaporation residues are implanted into one of a pair of double-sided silicon strip detectors (DSSDs) placed side by side, which form part of the Gamma Recoil Electron Alpha Tagging (GREAT) spectrometer [54]. GREAT consists of silicon, germanium and gas detectors which allow for selective correlations of conversion electrons, γ rays, α particles and protons detected at the target position. GREAT is designed for studying nuclei with production cross sections down to the order of picobarns [54]. A schematic diagram of GREAT is shown in Fig. 3.3.

Each DSSD is a 40×60 array of silicon strips with a strip pitch of 1 mm, resulting in 4800 pixels. Each DSSD has a thickness of 300 μm and measures the

energies of implanted ions and the decays that follow. A multiwire proportional counter (MWPC) is placed in the path of particles transmitted by RITU such that the particles induce a signal in the MWPC before they are implanted into the DSSDs. The MWPC is an isobutane gas detector which is primarily used to distinguish between evaporation residues and their radioactive decays, as outlined in section 3.6. A planar double-sided germanium strip detector was placed a few mm downstream of the DSSDs inside the same vacuum chamber, allowing for the detection of x rays and low-energy ($\lesssim$ 150 keV) γ rays. Three clover-type germanium detectors with four-fold segmentation providing detection of higher-energy ($\gtrsim$ 150 keV) γ rays were placed around the DSSDs in the present experiments: a larger volume detector positioned above the DSSDs and two smaller detectors placed to the left and right of the DSSDs. A PIN diode array with 28 silicon detectors forming a perimeter around the edges of the DSSDs enables detection of conversion electrons and α particles escaping from the DSSDs.

3.5 Data Acquisition

Signals from JUROGAM II and GREAT were received by the total data readout (TDR) acquisition system [55]. TDR is a triggerless data acquisition method which eliminates common dead time and is therefore suitable for high rate data. With TDR, all data is read and timestamped as opposed to the traditional method of recording data only when specific hardware trigger conditions are met. Software in the event builder uses spatial and temporal correlations to reconstruct correlated signals. Timestamping has a precision of 10 ns, giving accurate temporal correlations between target-position γ rays, evaporation-residue implantations and decays at the focal plane.

3.6 Correlation Techniques

Nuclei that decay via the emission of an α particle or a proton do so with a characteristic decay energy and half-life. This provides an opportunity to identify the nuclear species of a specific evaporation residue if the decay energy and half-life are known. This is useful in scenarios in which there are multiple reaction channels that produce nuclei which are not necessarily of interest and generate γ-ray emissions which mask the presence of weaker electromagnetic decays from the nuclide being studied. Fusion-evaporation reactions produce several nuclear species and so it is advantageous to correlate evaporation residues with their decays, a process known as recoil-decay tagging (RDT) [56].

The JUROGAM-RITU-GREAT setup is ideal for employing RDT. Following the reaction at the target position at the centre of JUROGAM II, the fusion-evaporation residues pass through the magnetic field of the gas-filled separator RITU before being implanted into a DSSD. The two side by side DSSDs consist of a total of 4800 pixels. Once a nucleus is implanted into one of these pixels, it will eventually decay, which will produce a signal in the detector.

In order to make correlations between implanted evaporation residues and their subsequent decays, it is necessary to distinguish between the signals that each of these produces. This is achieved by considering the response that each produces in the MWPC. In passing through the MWPC, evaporation residues deposit some of their energy in the detector, inducing a signal. Decays, however, take place in the DSSDs and so do not produce a signal in the MWPC. Hence, a decay and an evaporation-residue implantation can be clearly distinguished. However, a signal in the MWPC may not be due to the passage of an evaporation residue, as unreacted beam transported through RITU can pass through the MWPC if not sufficiently separated by the magnetic field. Further analysis of the MWPC and DSSD signals can distinguish between evaporation residues and unreacted

beam. Evaporation residues have lower momentum than unreacted beam and, due to their greater proton number, deposit more energy in the MWPC than the unreacted beam particles. Selection criteria for the time-of-flight (TOF) between the MWPC and DSSD and the energy deposited in the MWPC can be set such that only particles with a deposited energy and TOF typical of an evaporation residue are accepted, thereby eliminating a significant proportion of background particles.

Upon identifying a signal consistent with a radioactive decay, the preceding signal detected within the same pixel of the DSSDs is checked against the selection criteria for the implantation of an evaporation-residue. If the criteria are met, the energy deposited in the DSSD strip by the radioactive decay and the time between the evaporation-residue implantation and decay signals can be compared to the energy and half-life of a known decay. It is important to select a search time between the evaporation-residue implantation and decay signals that will allow a significant number of decays to be collected without compromising the cleanliness of the selection by including spurious counts due to random implantations in the same pixel. By using a search time of $3t_{1/2}$, 87.5% of decays occur within the acceptance time window. Increasing the correlation time further produces diminishing returns whilst adding background counts to the spectra.

It is possible for this procedure to misidentify the nuclear species of the evaporation residue. There are two sequences of events which each lead to a false correlation. In the first instance, two evaporation-residue implantations may occur within the same pixel, for which the system dead time will prevent the second evaporation residue from being recognised and so the decay will incorrectly be correlated with the first evaporation residue. The second type of false correlation occurs when two consecutive evaporation-residue implantations take place in the same pixel before the first evaporation-residue decays. In this case the decay will be correlated with the second evaporation residue, despite it being due to the first evaporation residue. The effects of false correlations become significant when the

evaporation-residue implantation rate is similar to the half-life of the decay being studied.

Having identified the species of the implanted nucleus, γ rays detected at the target position can be correlated with the nucleus. This is done by setting two-dimensional bounds on the TOF of the evaporation residue between JUROGAM II and implantation in the DSSDs and the TOF between MWPC and DSSDs. Figure 3.4 demonstrates the effectiveness of RDT in reducing background counts. Figure 3.4(a) shows γ rays detected at the target position that have been correlated only with the implantation of an evaporation residue, while Fig. 3.4(b) shows γ rays correlated with an evaporation residue whose implantation is followed by a ^{163}W α decay from the $7/2^-$ level in the same DSSD pixel. RDT can also be used to correlate delayed γ rays detected at the focal plane with evaporation residues, allowing γ rays depopulating isomeric states to be identified.

The observation of characteristic isomer decays at the focal plane provides another tool for identification of the evaporation residue. The procedure, known as recoil-isomer tagging, is suitable for nuclei with isomeric states which have a half-life long enough for a sufficient number of isomeric decays to be observed in the focal plane detectors. Gamma rays observed at the focal plane are accepted if they are detected within a given time limit following an implantation, defined according to the half-life of a known isomeric state. If any of the measured γ-ray energies matches that of a known transition associated with the isomer, the evaporation-residue implant is identified with the nuclear species of the isomeric decay. False correlations occur when Compton-scattered γ rays by chance have an energy coinciding with the selected energy limits. Figure 3.4(c) demonstrates recoil-isomer tagging, where γ rays detected at the target position are correlated with evaporation residues that are followed by the detection of γ rays depopulating the $13/2^+$ isomer of ^{163}W at the focal plane. The peaks associated with the yrast band of ^{163}W are clearly visible, while γ rays from other ^{163}W rotational bands are eliminated.

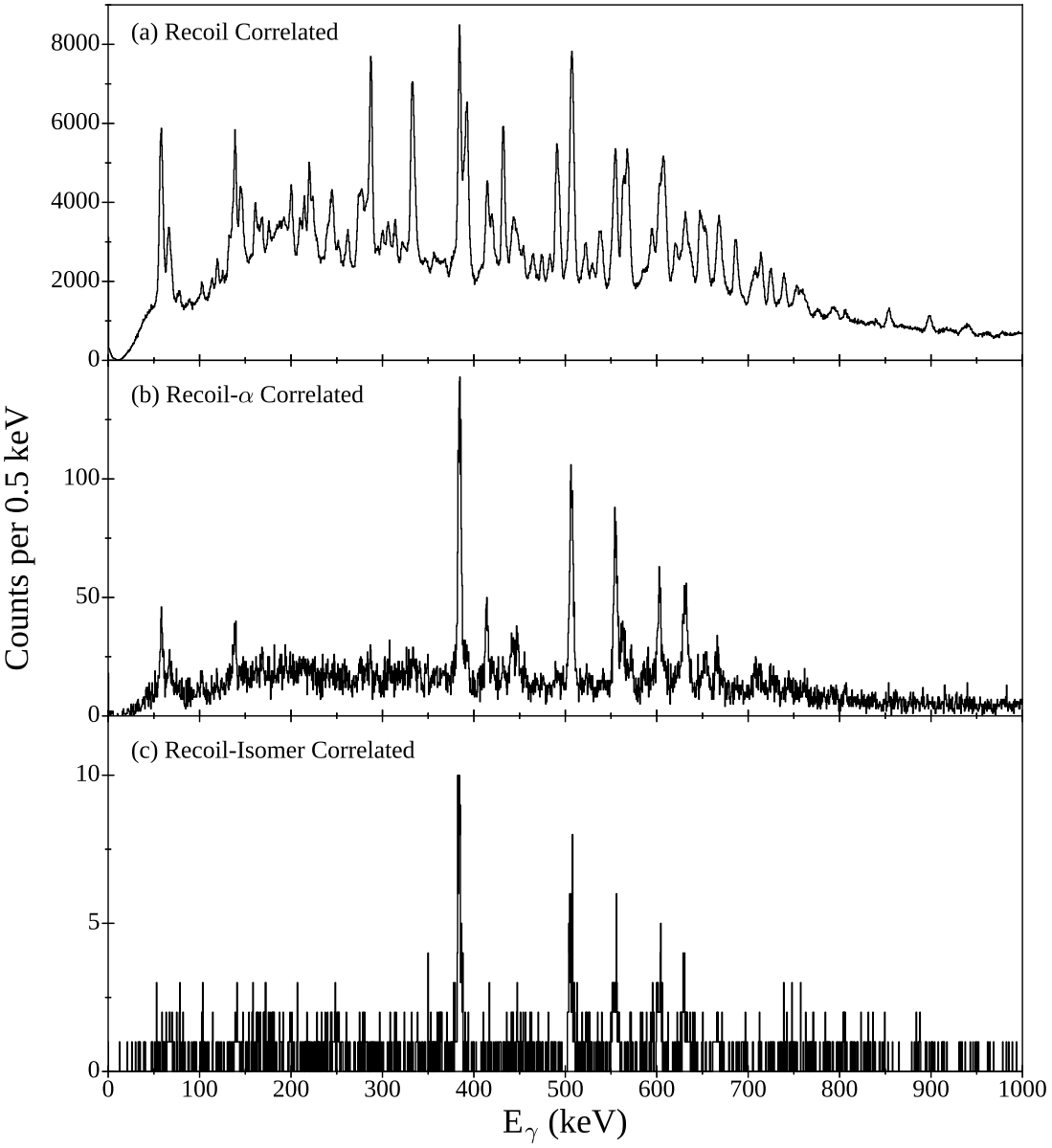

FIGURE 3.4: Gamma-ray spectra measured by JUROGAM II demonstrating the background reduction achieved using RDT. (a) Gamma rays in delayed coincidence with an evaporation-residue implantation in the DSSDs. (b) Gamma rays in delayed coincidence with an evaporation-residue implantation that was followed in the same DSSD pixel by a 5384 keV decay within 8.25 s, characteristic of the ^{163}W α decay from the $7/2^-$ level. (c) Gamma rays in delayed coincidence with an evaporation-residue implantation which is followed within 0.5 μs by a 102, 377 or 441 keV γ ray detected in the planar Ge detector or a 377 or 441 keV γ ray detected in the clover Ge detectors at the RITU focal plane.

3.7 The DPUNS Plunger Device

The Differential Plunger for Unbound Nuclear States (DPUNS) facilitates lifetime measurements for excited states in nuclei with low production cross sections via the recoil distance Doppler-shift technique, which is described in section 3.8. A schematic of the device is shown in Fig. 3.5. DPUNS was installed at the target position of JUROGAM II as shown in Fig. 3.6. The device houses a target and degrader foil and controls the distance between them. Velocity-degraded evaporation residues are transmitted to the entrance of RITU.

The basis for the design of DPUNS was the Köln plunger device [57] with additional modifications included aimed at optimising measurements in nuclei with low production cross sections. Adjustment of the target-to-degrader distance is achieved using a linear piezoelectric stepper motor with an accuracy of approximately 20 nm. A constant target-to-degrader distance is achieved by continuously correcting for variations that can occur in the target-to-degrader distance due, for example, to variations in the temperature of foils. A voltage pulse is applied to the degrader foil which induces a voltage in the target foil. The induced voltage is then used as a feedback signal. The software receiving the feedback signal can then apply a correcting voltage accordingly. The corrections to the target-to-degrader distance can be applied by a piezoelectric actuator, however the movement resolution of the stepper motor allows the distance to be corrected without the need of the actuator. The target and degrader foils are optically aligned to ensure a constant target-to-degrader distance over the entire surface of the foils.

It is necessary to separate the helium gas of RITU from the piezoelectric motors. This is achieved using a differential pumping system which removes helium gas from the beam line using a Roots pump. This system is advantageous compared to using a carbon foil to isolate the piezoelectric motors, as the beam would induce reactions in a carbon foil, producing nuclei whose decays would contribute

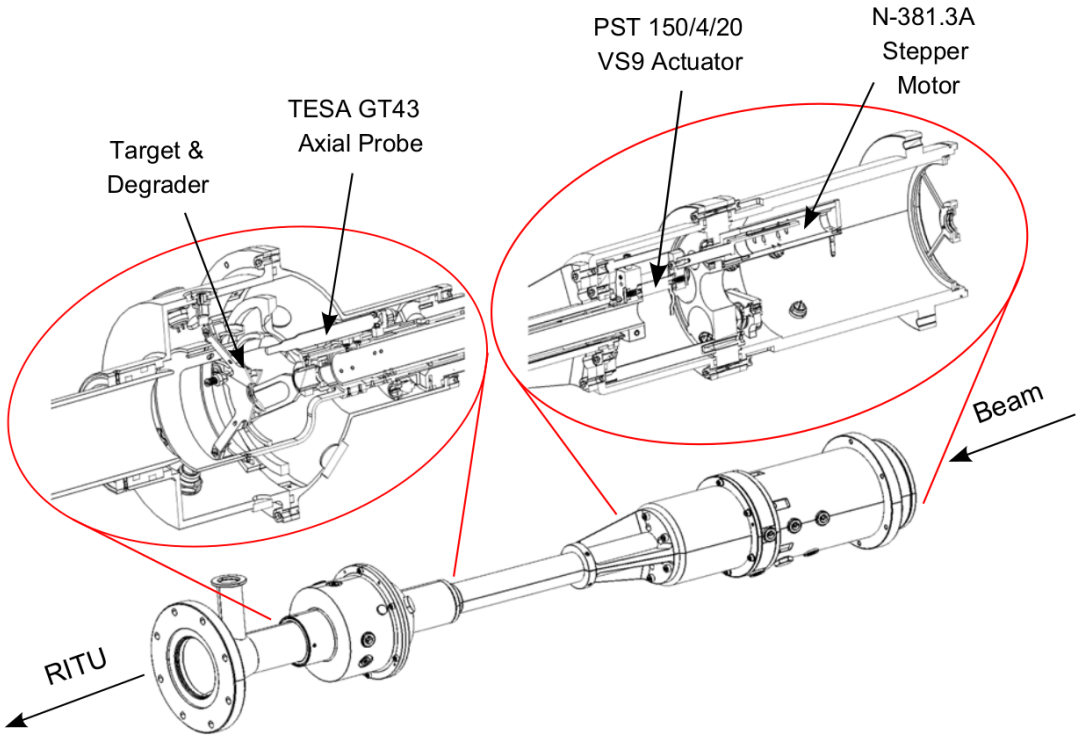

FIGURE 3.5: Schematic of the DPUNS plunger device. Taken from Ref. [58].

to the γ-ray background. This contribution to the background is eliminated when using differential pumping.

3.8 Recoil Distance Doppler-Shift Method

The recoil distance Doppler-shift (RDDS) method is an experimental technique for measuring lifetimes of excited nuclear states [12, 59]. The method measures lifetimes lying in the range 10^{-12}-10^{-9} s and is favourable because lifetimes can be calculated directly from quantities that can be obtained from an in-beam experiment without the need for further theories or nuclear models.

Figure 3.7 shows a schematic illustration of the standard RDDS method. Excited states are populated by a beam-induced nuclear reaction in a thin target. The reaction fragment recoils out of the target with a velocity v and encounters a stopper foil after a flight time $t_f = x/v$, where x is the separation between target

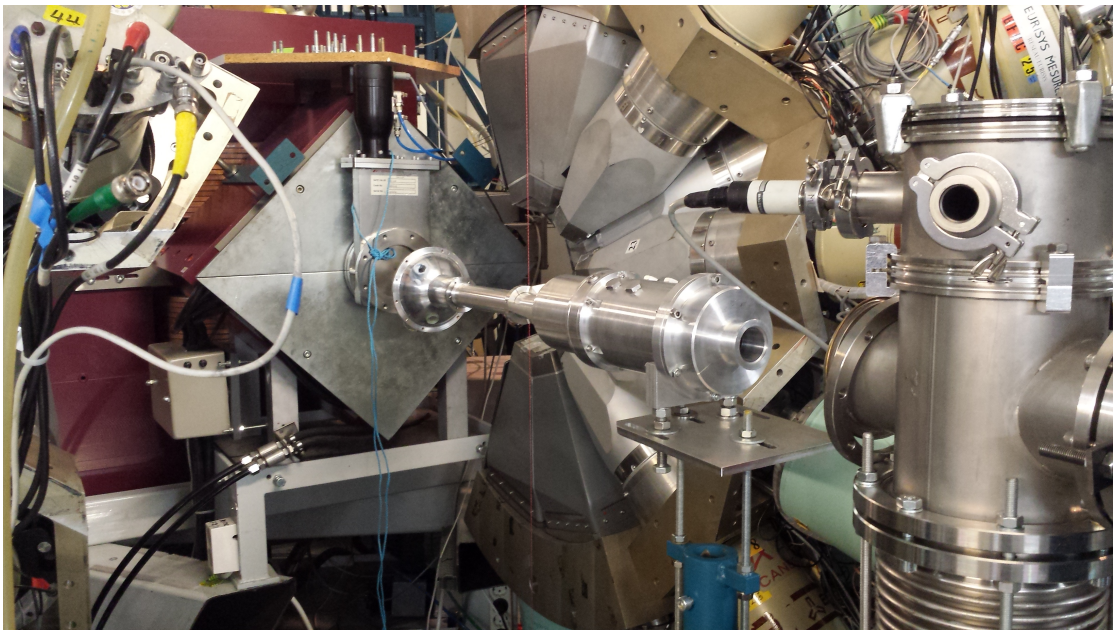

FIGURE 3.6: Photograph of the apparatus during set up of the experiment where the DPUNS plunger device (centre) can be seen.

and stopper. A 'plunger' device houses the target and stopper foil and facilitates the adjustment of the distance between them. The reaction fragment can either decay in flight between target and stopper, or it can decay once it has stopped in the stopper foil. Gamma rays emitted in flight are Doppler shifted in energy. The Doppler-shifted energy of a γ ray is given by the equation

$$E = E_0 \frac{\sqrt{1-\beta^2}}{1-\beta\cos(\theta)}, \tag{3.3}$$

where E_0 is the γ-ray energy when emitted at rest, $\beta = v/c$ and θ is the angle between the emitted γ ray and the reaction-fragment velocity. Hence, for a given transition, energy spectra feature a peak corresponding to unshifted γ rays emitted at rest and a peak corresponding to fully shifted γ rays emitted in flight. The intensity of the fully shifted peak, I_s, of a single excited level is given by

$$I_s = N_0[1 - e^{-\frac{x}{v\tau}}] \tag{3.4}$$

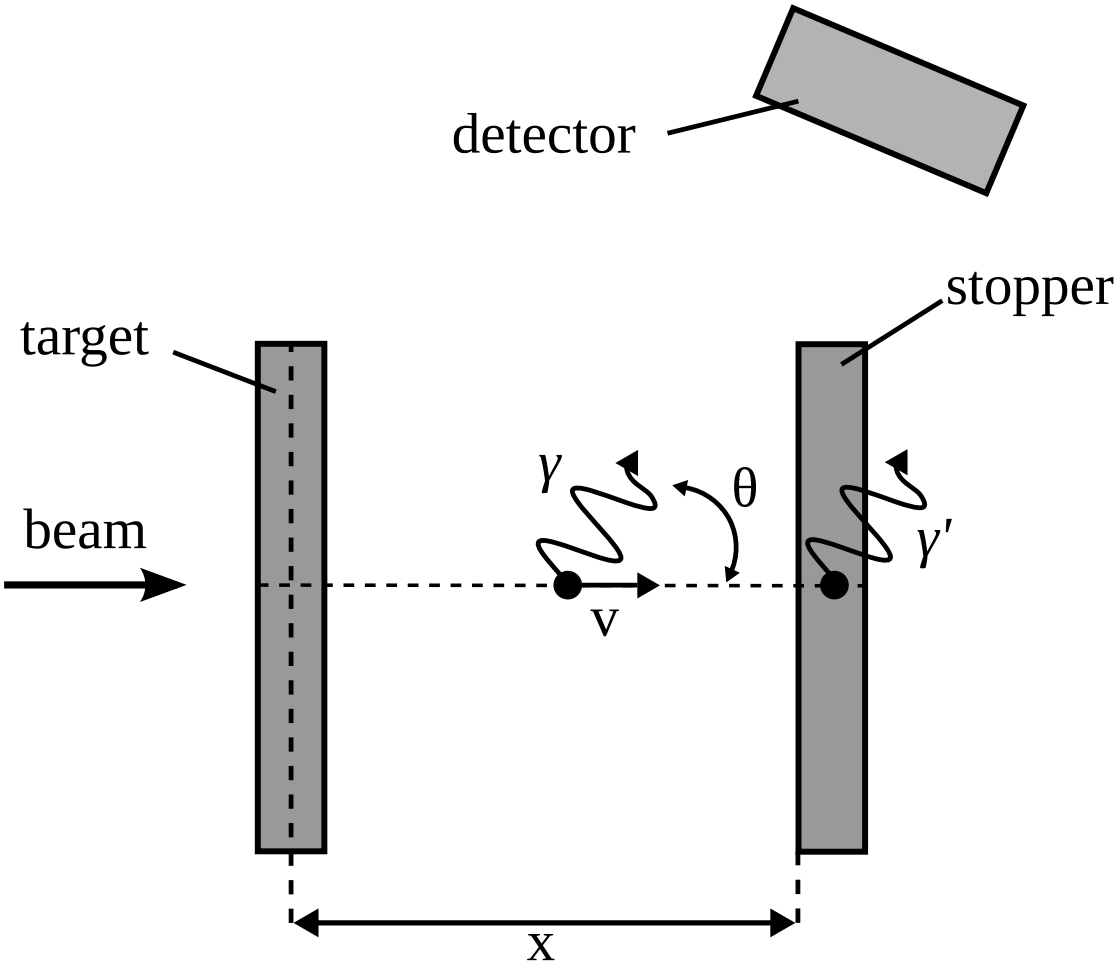

FIGURE 3.7: Schematic of the standard RDDS method. For differential plungers the stopper foil is replaced with a degrader foil.

where N_0 is the initial population of the level which has a lifetime τ. The intensity of the corresponding unshifted peak I_u is given by

$$I_u = N_0 e^{-\frac{x}{v\tau}}, \tag{3.5}$$

The lifetime can then be determined from the ratio of the unshifted intensity to the total intensity

$$\frac{I_u}{I_s + I_u} = e^{-\frac{x}{v\tau}}. \tag{3.6}$$

Measurements are made over a range of target-to-stopper distances, allowing for a lifetime to be calculated for each distance.

The differential plunger is an alternative setup where the stopper foil is replaced with a thin degrader foil. The velocity of a reaction fragment is reduced in the degrader foil, retaining enough momentum to be transmitted through an electromagnetic separator. This is desirable when studying nuclei with low production cross sections, where correlation techniques are required to suppress large γ-ray backgrounds. Reaction fragments that decay after passing through the degrader foil emit γ rays with a Doppler-shifted energy different to that of the fully shifted γ rays due to the difference in fragment velocity. When a differential plunger is employed, the precise location of any nucleus that decays after the degrader is unknown and hence solid-angle effects may need to be considered if the lifetime to be measured is relatively long.

There are a number of effects that can lead to errors in the lifetime measured using RDDS, in addition to the solid angle effects that have already been mentioned. Relativistic effects on lifetimes and observation angles must be considered at velocities greater than 3-4% of the speed of light. Reaction fragments leaving the target have a distribution of velocities due to the randomness of interactions taking place in the target and may have an asymmetry with respect to the mean velocity. The effect becomes more significant with increasing target thickness. Additionally, higher-velocity reaction fragments reach the degrader foil in a shorter time than those with a lower velocity, adding further asymmetry to the flight peak which will consist of fewer counts in the higher-velocity region. As a result, fitting a simple Gaussian distribution to the peaks will not accurately reproduce the spectrum and a more complex lineshape will need to be fitted. The deorientation effect is another source of errors and will be discussed in section 3.9.

3.9 The Differential Decay Curve Method

The Differential Decay Curve Method (DDCM) applies to RDDS data and simplifies the identification of systematic errors in comparison to conventional RDDS

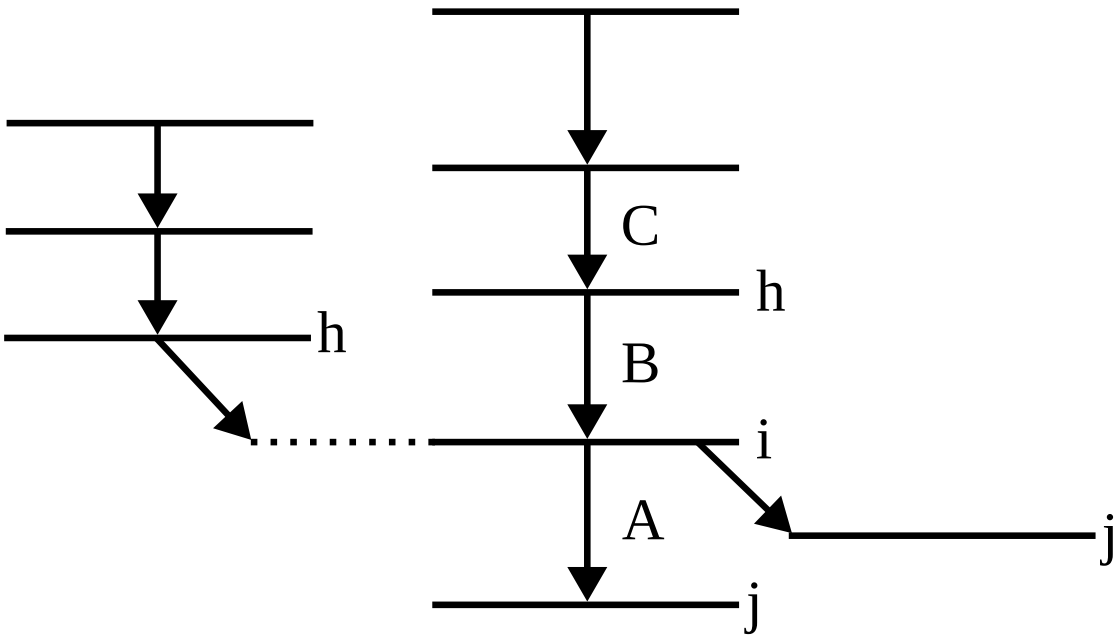

FIGURE 3.8: Example level scheme.

analysis [60, 61]. Only values that are experimentally accessible are used. In a conventional RDDS analysis, absolute flight times are required. However, the DDCM only uses relative flight times, which can be measured to higher precision than absolute flight times and with greater ease.

Excited states in nuclei tend to have complex feeding patterns, for which equation (3.6) is not applicable. An example level scheme is shown in Fig. 3.8. The rate of change in population of a nuclear level i fed by levels h is given by the Bateman equation

$$\frac{d}{dt}n_i(t) = -\lambda_i \cdot n_i(t) + \sum_{h=i+1}^{N} \lambda_h \cdot n_h(t) \cdot b_{hi}, \tag{3.7}$$

where $n_i(t)$ and $n_h(t)$ are the populations of i and h, respectively, at time t, λ are the decay constants of the respective levels, N corresponds to the highest index number of the feeding levels considered and b_{hi} are the branching ratios of the feeding levels. Two procedures are available in the DDCM for extracting level lifetimes from RDDS data. These are the singles and coincidence analyses, which are outlined here.

3.9.1 Singles Analysis

The Bateman equation may be written in terms of variables measured in RDDS experiments and may be rearranged to give the level lifetime τ_i

$$\tau_i(x) = -\frac{Q_{ij}(x) - b_{ij}\sum_h \Big([J_{hi}/J_{ij}]\Big)Q_{hi}(x)}{v\frac{d}{dx}[Q_{ij}(x)]}, \tag{3.8}$$

where the quantity $Q_{ij}(x) = \frac{I^d_{ij}(x)}{I^s_{ij}(x)+I^d_{ij}(x)}$ for a transition from level i to level j, where $I^d_{ij}(x)$ and $I^s_{ij}(x)$ are the degraded and fully shifted component intensities, respectively, J_{hi} and J_{ij} are the relative intensities of the γ-ray transitions populating and depopulating the level i, respectively, and v is the mean reaction-fragment velocity before the degrader.

Equation (3.8) determines the level lifetime for each target-to-degrader distance. A feature of equation (3.8) is that a range of target-to-degrader distances exists where the error on $\tau_i(x)$ minimises. This range is known as the region of sensitivity and corresponds to the region in which the numerator and denominator in equation (3.8) reach their maximum and hence through the propagation of their errors result in a small error on the lifetime. Accurately measured $\tau_i(x)$ values lie on a horizontal line within experimental errors, hence any deviation from a horizontal line indicates systematic errors have occurred.

The apparent lifetime of a particular level is dependent on the feeding time of that level. Feeding can occur from known and unknown discrete levels or from unobserved feeding from the continuum. Any lifetime extracted without accounting for the specific feeding of a level will only be an effective lifetime. If the unobserved feeding is not prompt, the derived lifetimes will deviate from a horizontal line. If required, statistical models can be used to estimate feeding times, or it can be assumed that the unobserved feeding has the same feeding time as the average observed feeding time of the state of interest from discrete feeders [62].

The deorientation effect can lead to significant errors in the extracted lifetime [63]. Reaction fragments initially tend to have their nuclear spins aligned perpendicular to the beam axis. The atomic electron configurations of the recoiling nuclei are disturbed during the reaction and the flight through the target. Immediately after leaving the target, the electrons of the recoiling nuclei rearrange into states that are energetically more favourable. This causes strong and fast changing magnetic hyperfine fields. These fields and the magnetic moments of excited nuclear states interact, causing the nuclear spin orientation to decay over the flight time. As a consequence, the γ radiation becomes more isotropic with increasing flight times [64]. The change in the measured lifetime due to the deorientation effect may be corrected by determining the ratio of decay curves measured at a nominated angle and at 55°, as outlined in Ref. [65], or by deriving a numerical correction from measurements of unshifted and shifted components of a transition in a single detector as outlined in Ref. [64]. However, such corrections may be avoided by application of the coincidence analysis.

3.9.2 Coincidence Analysis

The level lifetime is again derived from the Bateman equation by replacing terms with their observed quantities. In the coincidence analysis, the number of feeding transitions that must be considered is reduced to only the transition whose coincidences are selected, eliminating the problem of unobserved side feeding. In the following, coincident intensities are represented as $\{X,\ Y\}$, where the order indicates that transition X occurs before transition Y. For γ rays coincident with the fully shifted γ rays of the transition labelled B in Fig. 3.8, the lifetime of level i can be calculated using

$$\tau_i(x) = \frac{\{B_s, A_d\}(x)}{\frac{d}{dx}\{B_s, A_s\}(x)} \cdot \frac{1}{v}, \tag{3.9}$$

where A_d and A_s are the degraded and fully shifted components of transition A, respectively, and likewise for transition B. The coincident intensities in equation (3.9) are observed intensities. Alternatively, if coincidences are demanded with the fully shifted γ rays of an *indirect* feeding transition C, the lifetime of level i is calculated using

$$\tau(x) = \frac{\{C_s, A_d\}(x) - \alpha\{C_s, B_d\}(x)}{\frac{d}{dx}\{C_s, A_s\}(x)} \cdot \frac{1}{v}, \tag{3.10}$$

where $\alpha = \langle\alpha(x)\rangle_x$ with

$$\alpha(x) = \frac{\{C_s, A_d\}(x) + \{C_s, A_s\}(x)}{\{C_s, B_d\}(x) + \{C_s, B_s\}(x)}, \tag{3.11}$$

which corrects for differences in the measured intensities in the depopulating and feeding transitions.

The effect of the chosen coincidence selection criteria on measured lifetimes in the presence of the deorientation effect has been investigated by Petkov *et al.* [66]. The study found that when coincidences are demanded with the fully shifted component of the feeding transition, a cancellation occurs in equation (3.9) due to the equal influence of deorientation on each of the required coincident intensities. However, the effect remains present when coincidences are demanded on the unshifted component of the depopulating transition. Hence, the problem of deorientation can be circumvented by analysing γ rays coincident with the fully shifted peak of a transition that directly feeds the level of interest.

The coincidence analysis removes the impact of side feeding and deorientation on measured lifetimes and is therefore preferred over the singles analysis. However, greater levels of statistics are required for a coincidence analysis, therefore the singles analysis still has applicability when low levels of statistics are available.

Chapter 4

Lifetime Measurements of Excited States in ^{163}W

4.1 Introduction

Recent studies of atomic nuclei have focussed on obtaining a detailed understanding of the evolution of nuclei from single-particle behaviour near closed shells to collective behaviour at the midshell. The largest known shell is $82 \leq N \leq 126$, which enables a comprehensive study of the evolution of collective behaviour as a function of neutron number. Nuclei located in the region intermediate between the shell closures and the midshell are known as transitional nuclei, as these nuclei display a mixture of single-particle and collective behaviour. Numerous tungsten isotopes are experimentally accessible in the $82 \leq N \leq 126$ shell, with excited states having been observed in a near-complete chain ranging from ^{158}W ($N = 84$) [67] to ^{192}W ($N = 118$) [68], at the time of writing. Therefore, the tungsten isotopes provide a prime opportunity to study the evolution of collective properties as a function of neutron number.

The study of $B(E2)$ reduced transition probabilities of excited states in nuclei

in the Os, W, Pt region has been initiated in order to gain an intricate understanding of the dependence of structural effects on the neutron number. Studies of transitional even-N nuclei have revealed apparently anomalous $B(E2)$ ratios [19–21] that do not follow the predictions of the collective model [7]. In the tungsten isotopes, ^{166}W was found to have anomalous $B(E2)$ ratios with a particularly low $B(E2\colon 4^+ \rightarrow 2^+)/B(E2\colon 2^+ \rightarrow 0^+)$[1] ratio of 0.33(5) [20]. In this work, lifetimes of excited states in the $i_{13/2}$ band of ^{163}W have been extracted. The corresponding $B(E2)$ values and ratios have been extracted and compared with those of the other tungsten isotopes in the context of the collective model.

4.2 Previous Studies

Studies of the even-even $N \geq 90$ tungsten isotopes have established that in the yrast band, the first crossing is due to the rotational alignment of a pair of $i_{13/2}$ neutrons [14, 69, 70]. This was based on the observed gain in aligned angular momentum being consistent with that expected from cranked Woods-Saxon shell-model calculations for a pair of $i_{13/2}$ neutrons. Dracoulis *et al.* then observed a lower gain in alignment in ^{162}W ($N = 88$) and interpreted this as being an indication that the first rotational alignment in the yrast band of ^{162}W was due to the alignment of a pair of $h_{9/2}$ neutrons [71]. The favouring of the $\nu f_{7/2}$, $h_{9/2}$ orbitals over the $\nu i_{13/2}$ orbitals in ^{162}W is due to the lower deformation, which raises the excitation energy of the $\nu i_{13/2}$ states relative to the Fermi surface. Hence, it was established that ^{163}W is positioned at a critical point in the chain of tungsten isotopes, at which the competition to form the yrast band between the $i_{13/2}$ and $f_{7/2}$, $h_{9/2}$ neutron orbitals is most pronounced.

Excited states in ^{163}W were first establish by Dracoulis *et al.*, who determined that the observed rotational band was based on the $i_{13/2}$ neutron orbital [71]. A subsequent study by Scholey *et al.* identified the $i_{13/2}$ band head as an isomeric

[1] referred as $B_{4/2}$ in following sections.

state and established the decay path to a $7/2^-$ state which subsequently decays by α emission [72]. Concurrently, Thomson *et al.* extended the level scheme with the observation of five new band structures [73]. The level scheme is shown in Fig. 4.1. An irregular alignment pattern was observed in the yrast band, featuring consecutive gains in alignment with increasing rotational frequency. This was interpreted as being due to the alignment of a pair of ($h_{9/2}$, $f_{7/2}$) quasineutrons which was succeeded by the alignment of a pair of $h_{11/2}$ quasiprotons. This was in contrast to heavier odd-A tungsten isotopes in which it is the $i_{13/2}$ quasineutrons that undergo the first rotational alignment in the yrast band [14, 70]. As with the even-N neighbours, this observation was explained as being the result of the decreasing deformation forcing the $\nu i_{13/2}$ states to increasingly higher excitation energies, relative to the Fermi surface.

4.3 Details of Experiment

In order to populate excited states in ^{163}W, the ^{106}Cd(^{60}Ni, 2pn) fusion-evaporation reaction was employed in an experiment at the Accelerator Laboratory of the University of Jyväskylä, Finland. The target was a 1.1 mg/cm^2 thick, self-supporting enriched (>98%) ^{106}Cd foil with a Ta support of thickness 1.3 mg/cm^2. The Ta foil was placed facing the beam, resulting in a bombarding energy of 270 MeV and an initial evaporation-residue velocity of $v/c = 3.1\%$ at the front of the ^{106}Cd layer. The target and a 1.0 mg/cm^2 Mg degrader foil were mounted in the DPUNS differential plunger device [58], which was placed at the centre of the JUROGAM II germanium detector array [50, 51]. The degrader foil reduced the velocity of fusion-evaporation residues to $v/c = 2.1\%$, giving an energy separation of $\Delta E \sim 5$ keV between the fully shifted and degraded components of a 500 keV transition detected at 158° to the beam axis. Measurements were taken at eleven different target-to-degrader distances ranging from 30 to 5000 μm. Velocity-degraded fusion-evaporation residues were transported through RITU and implanted into

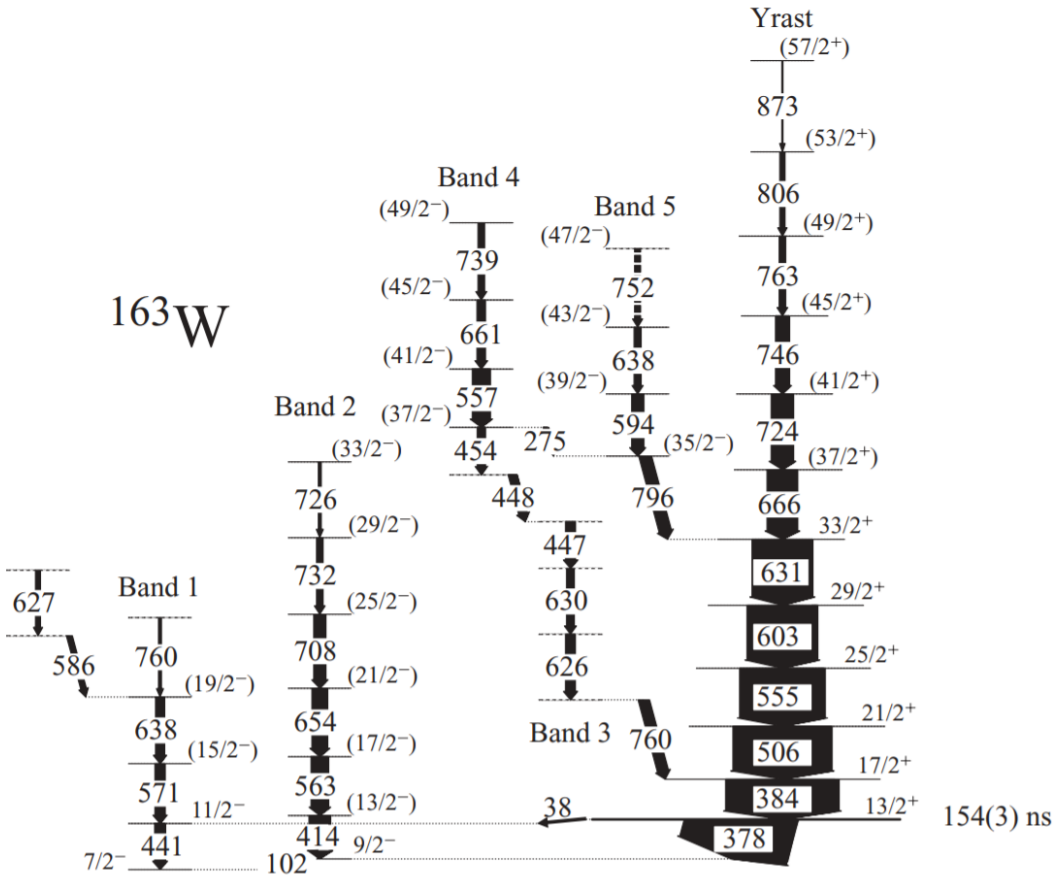

FIGURE 4.1: The level scheme developed by Thomson *et al.*, where the energies are in keV and the widths indicate the intensity of the transition. Taken from reference [73].

the DSSDs of the GREAT spectrometer. Three clover germanium detectors and a planar germanium detector were positioned at the focal plane.

4.4 Results

4.4.1 Preparatory Analysis

Detector Gain Drift

During an experiment the gain of a detector can drift over time. Should the gain of a particular detector drift during an experiment, the measured energy would also change, resulting in a broadening of spectrum peaks. In RDDS experiments,

corresponding fully shifted and degraded components need to be distinguished from each other. It is therefore necessary for peaks to be narrow, as the separation between components is often small. Hence, before a lifetime analysis can be performed it is important to check for gain drift in each detector and to apply a correction where appropriate.

One simple method of observing gain drift is to plot a two-dimensional histogram of the counts recorded by a detector as time progresses and to look for changes in the positions of the peaks. An example of this is shown in Fig. 4.2, which shows the time of detection versus the energy measured for the JUROGAM II detectors at 134° to the beam axis. The counts are correlated with evaporation-residue implantations followed by a characteristic α decay of ^{163}W from the $7/2^-$ state [72]. The top panel corresponds to a target-to-degrader distance of 45 μm (where degraded components dominate) while the bottom panel corresponds to 2000 μm (fully shifted components dominate). The 384 keV $17/2^+ \rightarrow 13/2^+$ transition from ^{163}W is the strongest transition present and is Doppler shifted to $\sim$ 375 keV. If gain drift was present in these detectors, the measured energy of this transition would change over time and a diagonal line would be observed. The line is vertical, suggesting that gain drift is not present in this ring of detectors.

Each ring of JUROGAM II, the DSSDs, the focal plane clovers and the planar detector were all checked for gain drift. No significant gain drift was observed.

Contaminants

Following the formation of a compound nucleus in a fusion-evaporation reaction, the compound nucleus undergoes a particle evaporation process where α particles, protons and/or neutrons are emitted. The process is probabilistic; different nuclear species can be produced by the same compound nucleus. Over the course of an experiment a number of nuclei will be produced in varying quantities according to their production cross sections. Figure 4.3 shows the cross sections as a function of beam energy for the strongest channels in the reaction between a ^{60}Ni beam

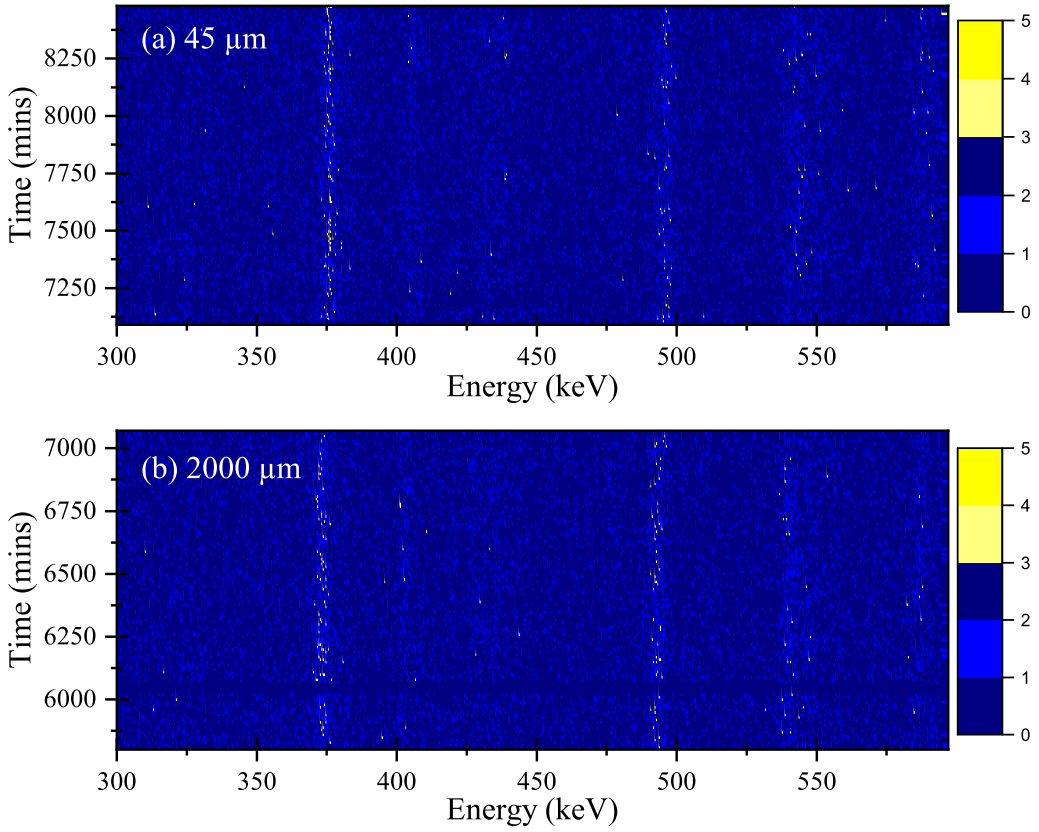

FIGURE 4.2: Two-dimensional histogram of counts measured at 134° to the beam axis, correlated with evaporation-residue implants that were followed within 8.25 s of implantation by a 5384 keV ^{163}W α decay [72], taken at a target-to-degrader distance of (a) 45 μm and (b) 2000 μm. The time axis has a bin width of 10 mins.

and a ^{106}Cd target. The data points are estimates based on the output of the Projection Angular Momentum Coupled Evaporation (PACE4) code [74–76].

Evidently there are strong reaction channels in addition to that producing ^{163}W, and γ rays from the nuclei produced in these channels will be present in γ-ray spectra. This presents a problem for $\gamma\gamma$ coincidence analyses, as γ rays from different nuclei may overlap in energy, preventing a clean selection of a single γ-ray peak. In these cases contamination would enter the spectra of coincident γ rays, introducing errors into the extracted intensities of individual transitions. As discussed in section 3.6, significant amounts of contamination can be removed by employing correlation techniques.

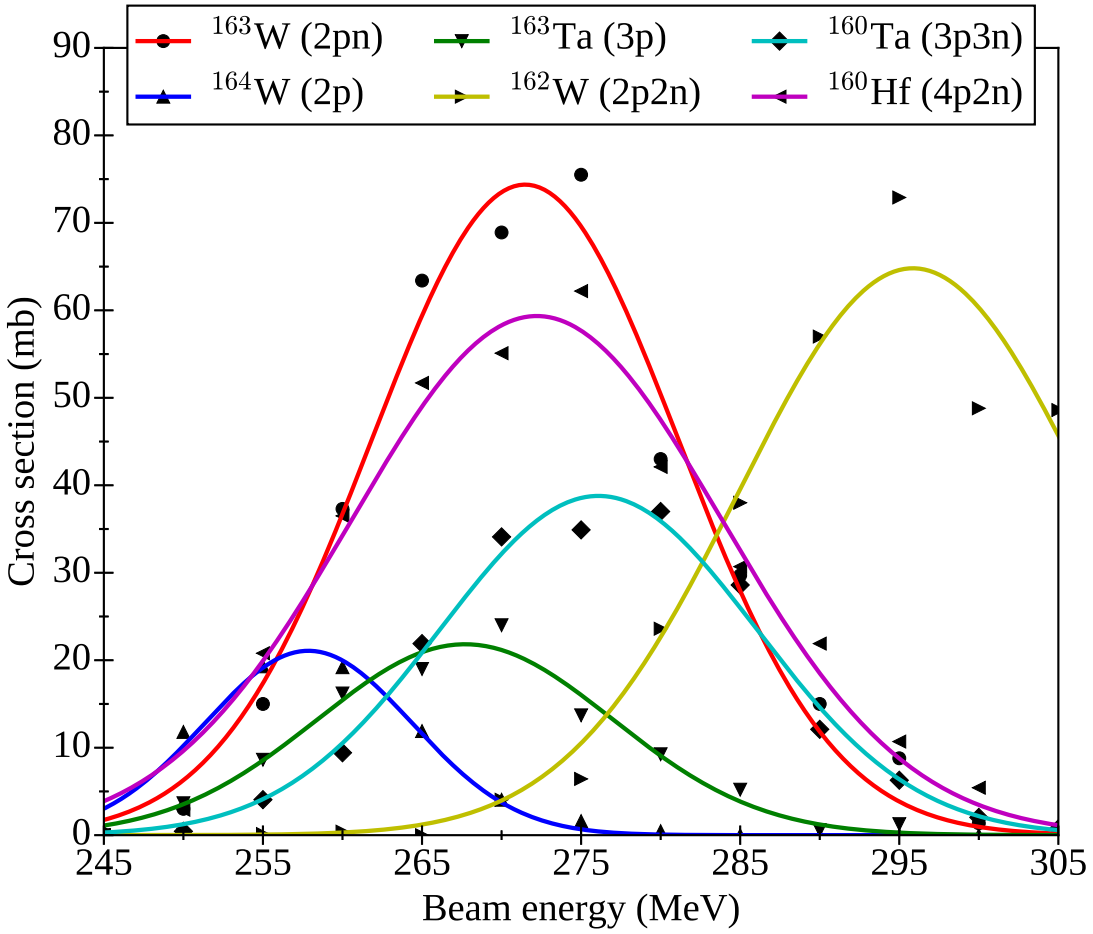

FIGURE 4.3: Reaction cross sections for the strongest exit channels in the reaction between a ^{60}Ni beam and a ^{106}Cd target, estimated using the PACE4 code [74–76].

4.4.2 Evaporation-Residue Velocity Measurement

The evaporation-residue velocity before and after the degrader is an important parameter in RDDS experiments. From equation (3.3), the energies of the fully shifted and degraded γ-ray transitions depend on the velocity of the evaporation residue upon emission. The velocity is needed to calculate lifetimes using equations (3.8) – (3.10). At non-relativistic velocities equation (3.3) simplifies to

$$E = E_0\Big(1 + \beta cos(\theta)\Big). \tag{4.1}$$

Hence, by measuring the detected energy as a function of $\cos(\theta)$ for a given transition, the velocity can be calculated.

The $13/2^+$ band head is isomeric with a half-life of 154(3) ns and is depopulated via two distinct γ-ray cascades to the ground state [72]. These isomer-delayed γ rays may be detected in the GREAT planar and clover detectors at the RITU focal plane and can be used to select γ rays observed in the JUROGAM II detectors at the target position. Recoiling ^{163}W nuclei were selected on the condition that implantations were followed within 0.5 μs by a 102, 377 or 441 keV γ ray detected in the planar Ge detector or a 377 or 441 keV γ ray detected in the clover Ge detectors at the RITU focal plane. Gamma rays observed at the target position in delayed coincidence with selected ^{163}W implantations in the DSSDs were sorted into energy spectra for each target-to-degrader distance. At a target-to-degrader distance of 45 μm the fully shifted component was absent for a number of transitions, allowing the measured energy of the degraded component to be determined. Hence spectra taken at this distance provided an accurate measurement of the evaporation-residue velocity after the degrader. Similarly, spectra taken at 2000 μm were used to measure the evaporation-residue velocity before the degrader using transitions in which the fully shifted component was dominant. For each of these distances, several transitions were used to extract the evaporation-residue velocity by applying a linear fit to the measured energy as a function of $\cos(\theta)$, examples of which can be seen in Fig. 4.4. The measured velocities are summarised in Tab. 4.1, where weighted averages have been calculated giving $v/c = 3.11(4)\%$ before the degrader and $v/c = 2.08(5)\%$ after the degrader.

It is useful to apply a Doppler-shift correction to the detected γ-ray energies using the measured evaporation-residue velocity. In the lifetime analysis presented here, the spectra have been corrected using the velocity measured before the degrader. Hence, the fully shifted components of transitions each have a corrected energy measurement that is equal to the energy emitted by an evaporation residue at rest.

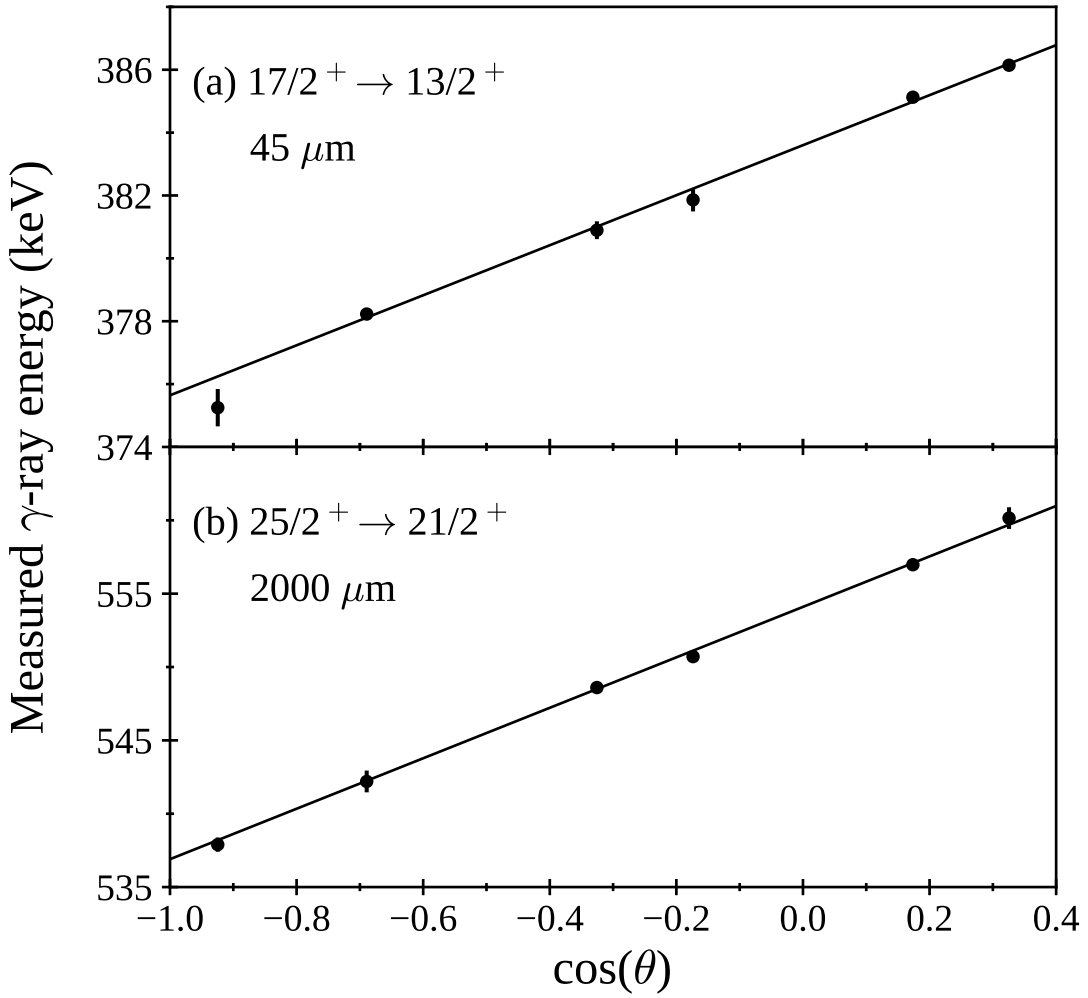

FIGURE 4.4: (a) Energy of the 384 keV $17/2^+ \rightarrow 13/2^+$ transition in ^{163}W as a function of $\cos(\theta)$ at 45 μm. (b) Energy of the 555 keV $25/2^+ \rightarrow 21/2^+$ transition in ^{163}W as a function of $\cos(\theta)$ at 2000 μm. The solid line shows the least-squares fit for each case.

TABLE 4.1: Measurements of evaporation-residue velocity before and after the degrader.

E (keV)	$I_i^\pi \rightarrow I_f^\pi$ ($\hbar$)	v/c (%)	
		Before degrader	After degrader
384	$17/2^+ \rightarrow 13/2^+$		2.07(5)
506	$21/2^+ \rightarrow 17/2^+$	3.29(9)	2.17(19)
555	$25/2^+ \rightarrow 21/2^+$	3.10(6)	
603	$29/2^+ \rightarrow 25/2^+$	3.05(8)	
	Average	3.11(4)	2.08(5)

4.4.3 Half-Life of the $13/2^+$ Isomer

The $13/2^+$ band head is known to be isomeric with a measured half-life of 154(3) ns [72]. To repeat this measurement, decay curves for the 378 and 441 keV transitions below the isomer were produced. The decay curves shown in Fig. 4.5 were generated from the time difference between an evaporation-residue implantation into the DSSDs and a γ ray of the required energy observed either in one of the clover detectors or in the planar detector. From a weighted least-squares fit of an exponential plus a constant to each decay curve, half-lives of 157(4) and 154(2) ns were extracted for the 378 and 441 keV transitions, respectively. The half-lives are consistent with these transitions occurring after the decay of a common isomer.

The decay curves for the 378 and 441 keV transitions were combined and a weighted least-squares fit was again performed, shown in Fig. 4.6. The 38 and 102 keV γ rays were not used, as the contribution from the Compton background is large in this energy range. The fit to the combined data gave $t_{1/2} = 155(2)$ ns, which is consistent with the half-life measured by Scholey *et al.*

4.4.4 Lifetimes of the $17/2^+$ and $21/2^+$ States

Recoil-Correlated Coincidence Analysis

Gamma-ray coincidence measurements are a convenient means of eliminating the side feeding of a state whose lifetime is to be measured. For each distance measured, γ rays observed in JUROGAM II in delayed coincidence with implantations of fusion-evaporation residues in the DSSDs were sorted into two separate asymmetric two-dimensional matrices; one consisting of γ rays detected at $\theta = 158°$ to the beam axis versus coincident γ rays detected either at $\theta = 158°$ or $\theta = 134°$ and the other consisting of γ rays detected at $\theta = 134°$ versus coincident γ rays detected either at $\theta = 158°$ or $\theta = 134°$.

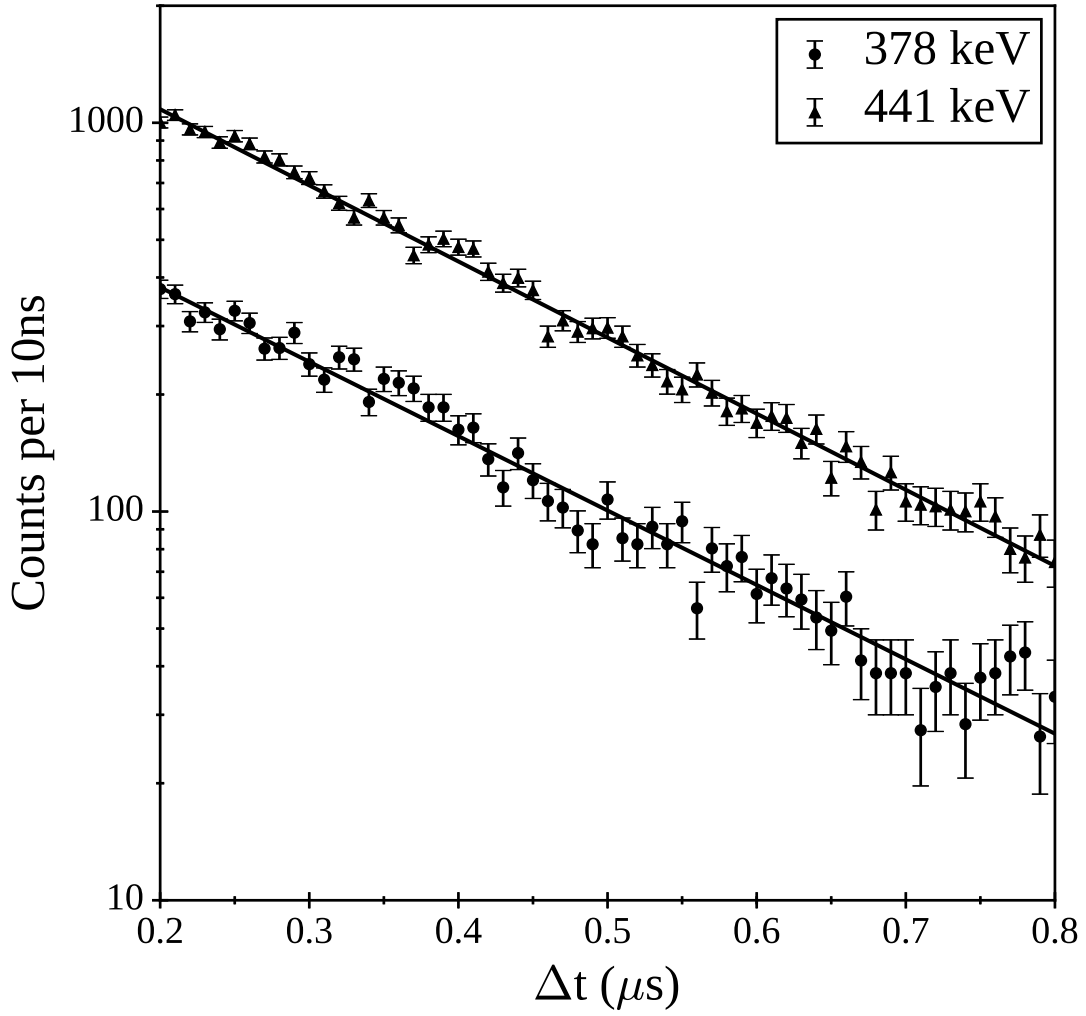

FIGURE 4.5: Decay curves for γ rays of energy 378 keV (circles) or 441 keV (triangles) following the implantation of an evaporation-residue into the DSSDs. Each line is a weighted fit of an exponential plus a constant background, with $t_{1/2} = 157(4)$ ns for the 378 keV γ rays and $t_{1/2} = 154(2)$ ns for the 441 keV γ rays.

Given optimal experimental conditions, demanding coincidences with the fully shifted component of the feeding transition is advantageous, as it has been shown that the influence of the deorientation effect is eliminated when using this method [66]. However, the multiplicity of γ rays in this experiment was high, which resulted in overlapping γ-ray peaks. As such, it was not always possible to make a clean selection on fully shifted γ rays detected at $\theta = 158°$ or $\theta = 134°$. Figure. 4.7 shows an energy spectrum of γ rays detected at $\theta = 158°$ or $\theta = 134°$

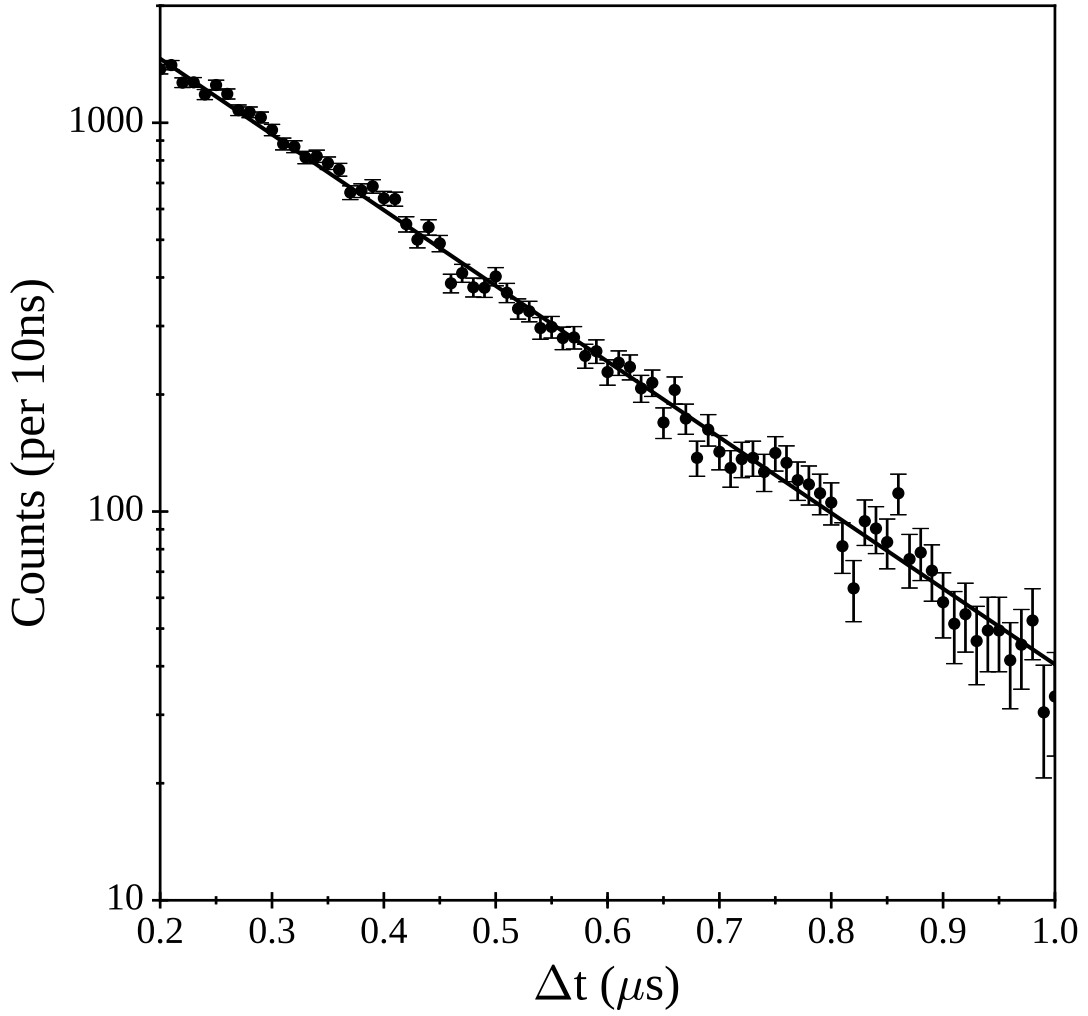

FIGURE 4.6: Decay curve generated from the time difference between a 378 or 441 keV γ ray in the clover or planar detector and an evaporation-residue implantation into the DSSDs. The line is a weighted fit of an exponential plus a constant background, giving a half-life of 155(2) ns.

in coincidence with any γ ray detected at $\theta = 134°$. The spectra shown are for target-to-degrader distances of 45 μm and 2000 μm, in which the degraded and fully shifted components of the 555 keV $25/2^+ \rightarrow 21/2^+$ transition can be seen, respectively. Contamination from the 552 keV $(15^-) \rightarrow (13^-)$ transition from ^{164}W obscures the limits of the degraded component of the 555 keV transition. By demanding coincidences with the low-energy half of the fully shifted component of the 555 keV transition, spectra were produced in which the contribution of the degraded component of the 555 keV transition was minimised. Typical energy

spectra are shown in Fig. 4.8. No background has been subtracted due to the lack of a clean background region on which to sample the Compton background. Contamination from ^{164}W is present in the spectra due to the overlap of the fully shifted component of the 555 keV transition with the 552 keV transition from ^{164}W. The transitions known to be coincident with the 552 keV transition do not have energies that overlap with the 384 and 506 keV transitions that depopulate the $17/2^+$ and $21/2^+$ levels, respectively, in ^{163}W. Therefore it is not expected that the contamination will affect the measured lifetimes. The fits to the spectra consist of a Gaussian distribution for each of the fully shifted and degraded components and a polynomial distribution for the Compton background.

The decay curves and lifetimes for the $17/2^+$ level are shown in Fig. 4.9. The intensities were normalised using the total intensity of the singles $2^+ \rightarrow 0^+$ transition in ^{164}W. This normalisation was used for a number of reasons: (1) the $2^+ \rightarrow 0^+$ transition is strongly populated in the spectra, (2) this transition is well separated from other γ-ray peaks, (3) by using the intensity from a singles measurement there are no angular correlations that might bias the intensity depending on the plunger distance. This method of normalising requires a constant beam energy over the duration of the experiment in order to be accurate, since the cross section for a given reaction product depends on the beam energy. The beam energy provided by the K-130 cyclotron used in the current work was not expected to vary significantly.

Demanding coincidences with lower-energy γ rays from the fully shifted component of the 555 keV transition selected ^{163}W nuclei with higher velocities than the mean value. Consequently, the lifetimes have been calculated using the mean velocity of the selected evaporation residues as opposed to the mean of the entire distribution. The velocity distribution can be obtained by fitting a Gaussian to the peak in the energy spectrum and using equation (3.3) to convert this into a velocity distribution. Due to the overlap with the 552 keV transition, the velocity distribution could not be determined directly from selected γ rays. Instead, the

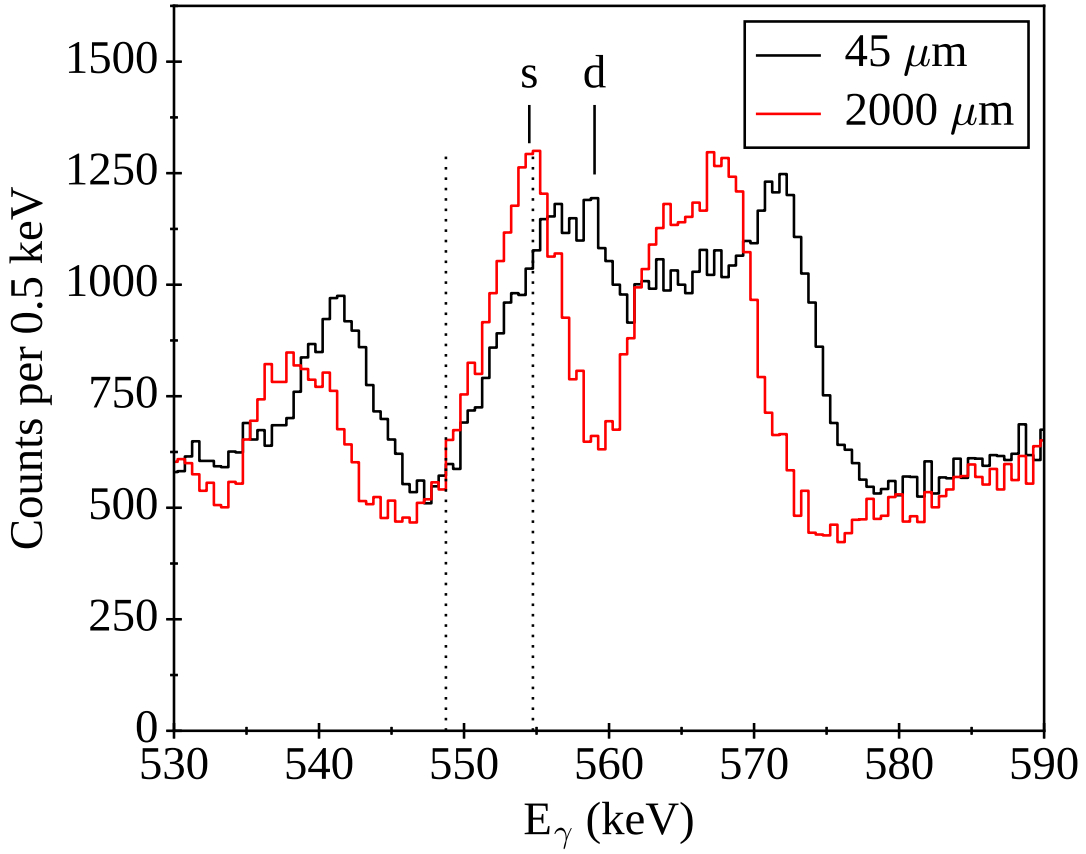

FIGURE 4.7: Gamma-ray coincidence spectra correlated with implantations of fusion-evaporation residues in the focal plane DSSDs. The black (red) spectrum corresponds to γ rays detected at $\theta = 158°$ or $\theta = 134°$ in coincidence with any γ ray detected at $\theta = 134°$ at a target-to-degrader distance of 45 μm (2000 μm). The positions of the fully shifted (s) and degraded (d) components of the 555 keV $25/2^+ \rightarrow 21/2^+$ transition of ^{163}W are labelled. The dotted lines indicate the selected range of fully shifted γ rays whose coincident γ rays detected at $\theta = 134°$ are shown in Fig. 4.8.

velocity distribution was determined for the spectra correlated with the decay of the $13/2^+$ isomeric state in ^{163}W previously described in section 4.4.2. The velocity distribution is assumed to be the same in the isomer-correlated spectra as it is for ^{163}W nuclei in Fig. 4.7. The detectors at angles of $\theta = 134°$ and $\theta = 158°$ were analysed separately, as the difference in angle results in a different range of velocities entering the selection limits. The velocity used to determine the level lifetime was the mean of velocities determined for $\theta = 134°$ and $\theta = 158°$, weighted

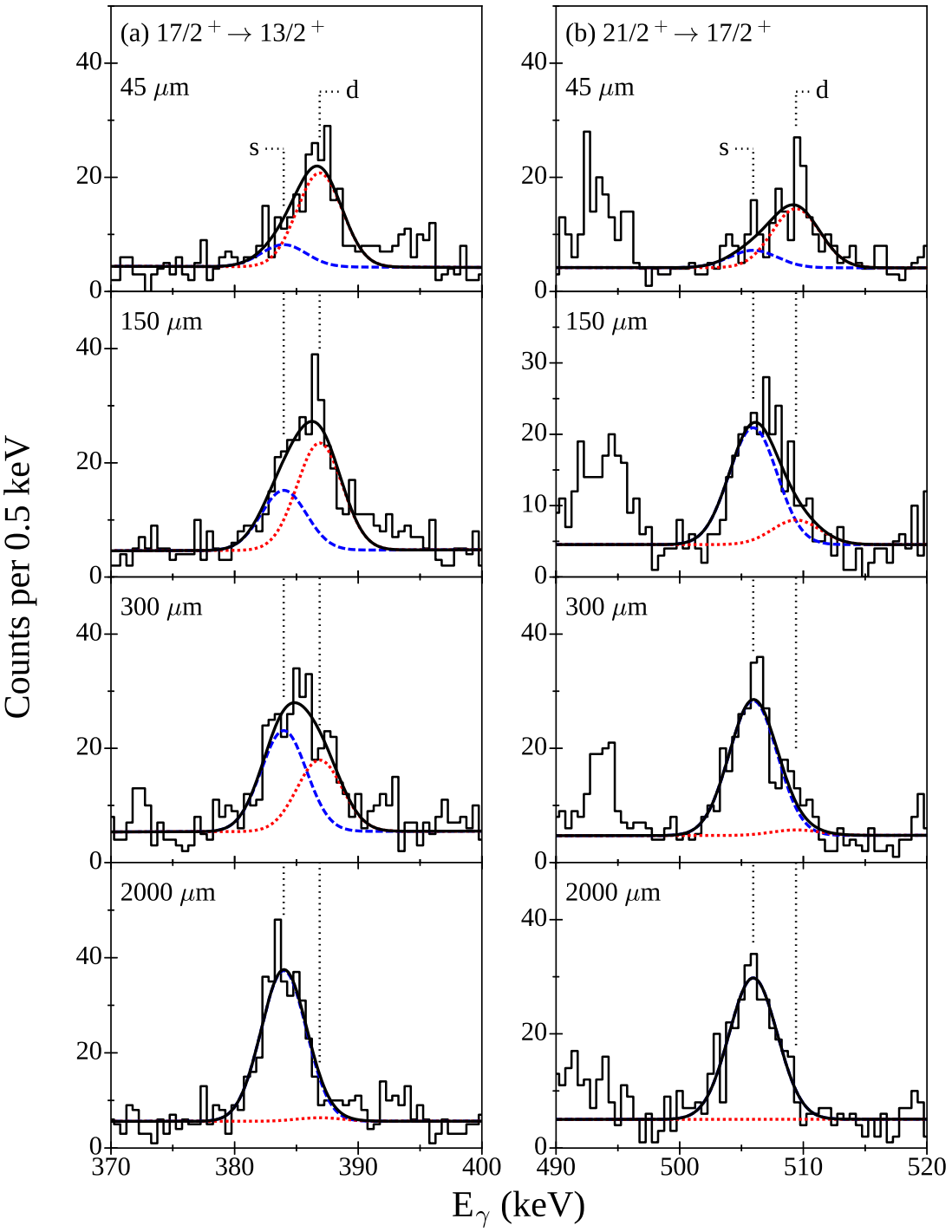

FIGURE 4.8: Gamma-ray coincidence spectra correlated with an evaporation-residue implantation in the DSSDs, measured at 134° to the beam axis. Coincidences were demanded with the fully shifted component of the 555 keV transition detected at the $\theta = 134°$ or 158° positions for all spectra shown. (a) Transitions depopulating the $17/2^+$ level. (b) Transitions feeding the $17/2^+$ level. Fits for the fully Doppler-shifted (s) and degraded (d) components are shown by the blue dashed and red dotted lines, respectively, while the total is shown by the black solid line.

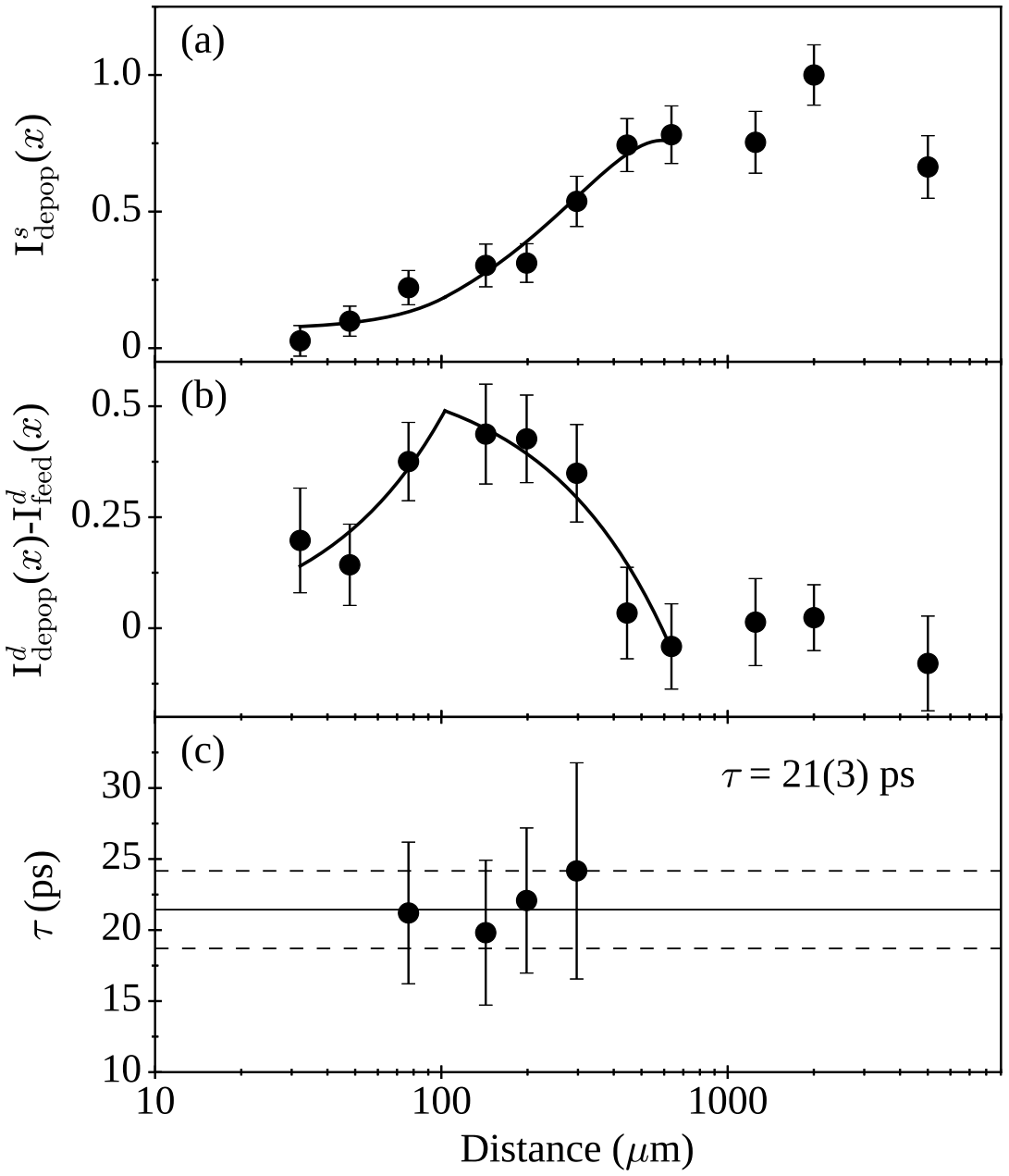

FIGURE 4.9: (a) Normalised fully shifted intensity of the transition depopulating the $17/2^+$ level measured at $\theta = 134°$. (b) Difference in intensity between the degraded components of the depopulating and feeding transitions. (c) Lifetimes measured for the $17/2^+$ level at distances within the region of sensitivity. The solid line indicates the weighted average while the dashed lines indicate the experimental uncertainty.

according to the number of counts at each θ.

The lifetimes plotted in Fig. 4.9(c) are approximately constant within the region of sensitivity. This suggests that there are no significant systematic errors, which can occur if the time behaviour of feeding transitions is not accounted for correctly. No systematic errors were expected since by demanding coincidences with an observed feeder any side-feeding transitions will be eliminated. The mean lifetime was obtained by a weighted average of the values at each distance within the region of sensitivity.

The same coincidence conditions that were used for the measurement of the lifetime of the $17/2^+$ level were used for that of the $21/2^+$ level. Decay curves for the $21/2^+$ level were plotted using the intensities extracted from the spectra shown in Fig. 4.8(b). These are shown in Fig. 4.10 along with the measured lifetimes. Again, for distances within the region of sensitivity the lifetimes plotted in Fig. 4.10(c) are approximately constant, implying that any systematic errors are minimal.

Recoil-Isomer Correlated Singles Analysis

Although the contamination present in the $\gamma\gamma$ coincidence analysis is not expected to influence the measured lifetimes, the validity of this assumption can be confirmed by attempting to eliminate the contamination and extracting the lifetimes of the levels. The recoil-isomer tagging technique employed in the measurement of the evaporation-residue velocity in section 4.4.2 was effective at removing the contamination. Gamma rays observed at $\theta = 134°$ that were selected using this method are shown in Fig. 4.11. A consequence of using this method was that the statistics were reduced to a level at which a coincidence analysis could no longer be performed and a singles analysis had to be implemented instead. It was possible to extract a lifetime using the detectors positioned at $\theta = 134°$, however there were fewer detectors at $\theta = 158°$, which meant that distinct peaks were not observed for the feeding transition at this angle.

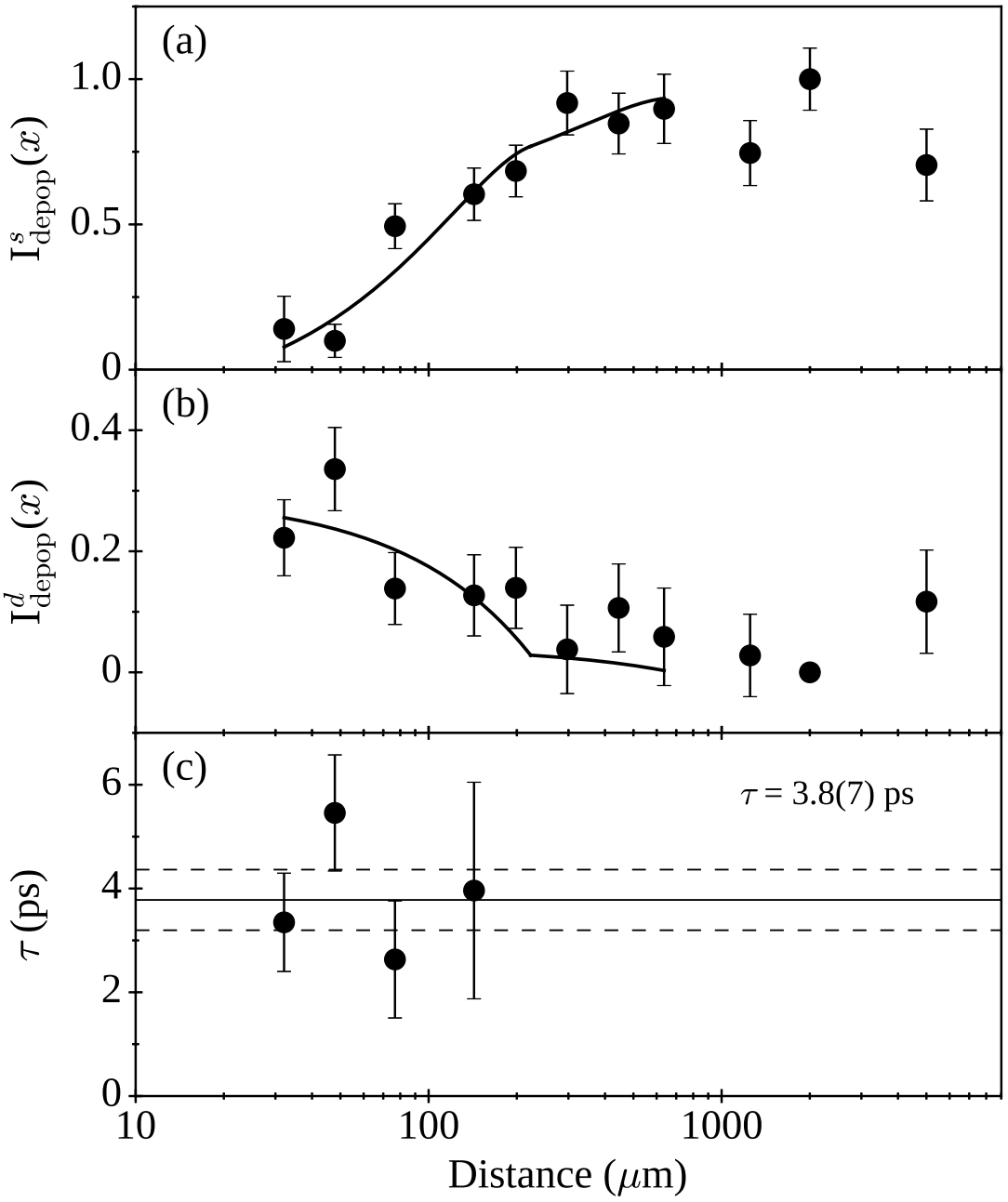

FIGURE 4.10: (a) Normalised fully shifted intensity of the transition depopulating the $21/2^+$ level measured at $\theta = 134°$. (b) Normalised degraded intensity of the transition depopulating the $21/2^+$ level. (c) Lifetimes measured for the $21/2^+$ level at distances within the region of sensitivity. The solid line indicates the weighted average while the dashed lines indicate the experimental uncertainty.

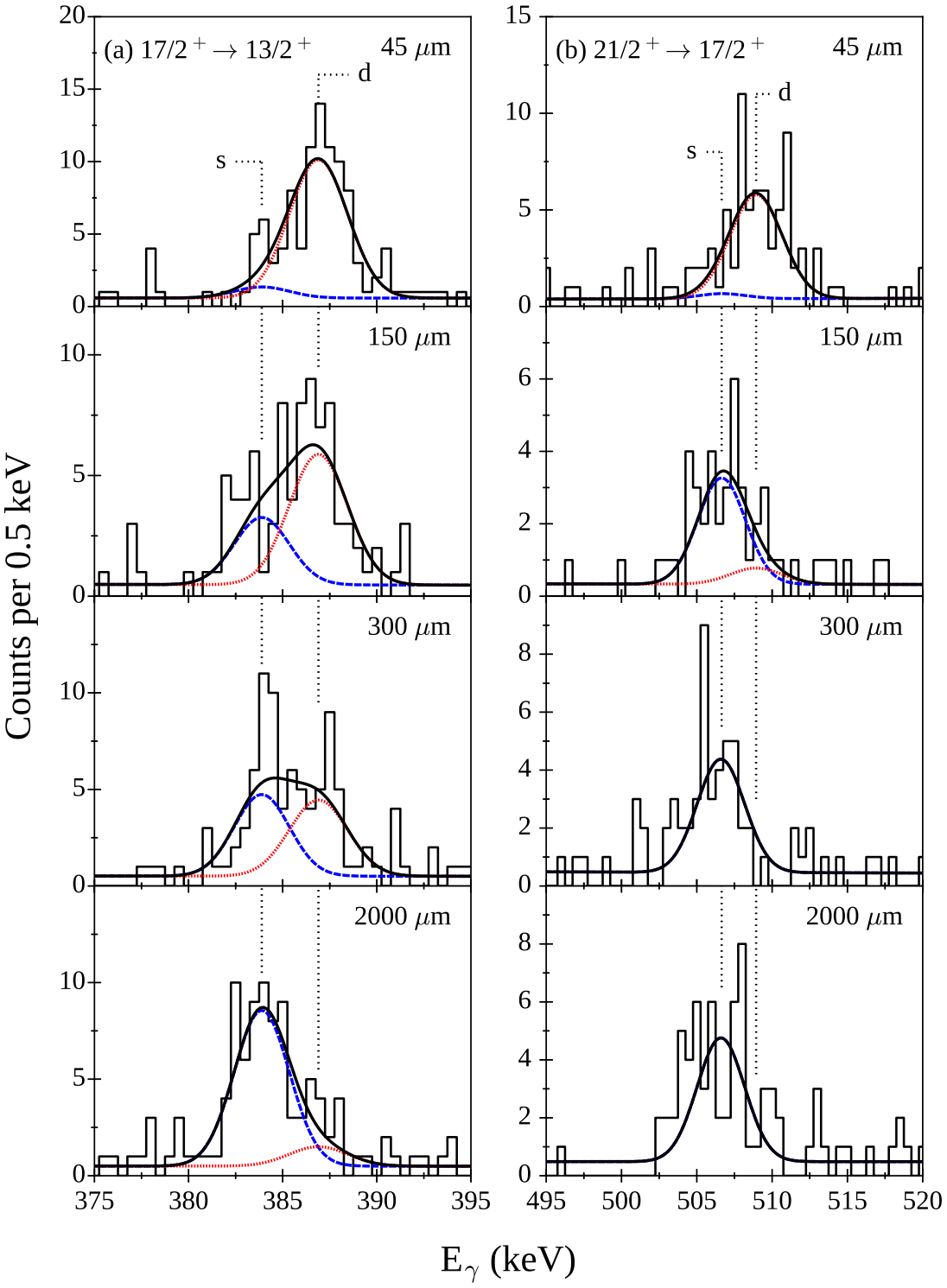

FIGURE 4.11: Gamma rays measured at 134° to the beam axis correlated with an evaporation-residue implantation that was followed within 0.5 μs by a 102, 377 or 441 keV γ ray detected in the planar Ge detector or a 377 or 441 keV γ ray detected in the clover Ge detectors at the RITU focal plane. (a) Transitions depopulating the $17/2^+$ level. (b) Transitions depopulating the $21/2^+$ level. The dotted lines show the positions of the centroids of the fully Doppler-shifted (s) and degraded (d) components.

A thorough lifetime analysis of the $17/2^+$ level should in principle account for the deorientation effect. In the present analysis however, the statistics were insufficient to make conclusions about the extent of the deorientation effect.

The decay curves and lifetimes extracted from the fitted intensities are shown in Fig. 4.12. The lifetimes measured at distances within the region of sensitivity show a constant trend within experimental uncertainties. This suggests that there are no significant systematic errors, implying that the deorientation effect has not significantly altered the measured lifetime and that the timing of the unobserved feeding has been accounted for correctly. This is particularly important in a singles analysis as the time behaviour of all sources of feeding of the level of interest must be considered. In this analysis, the assumption was made that the unobserved feeding of the $17/2^+$ level has the same time dependence as that of the observed feeding. The constant lifetimes measured at different target-to-degrader distances within the region of sensitivity suggests that this assumption is correct.

A lifetime consistent with that obtained in the coincidence analysis was extracted. This indicates that the overlap of the 552 keV transition of ^{164}W with the 555 keV transition of ^{163}W has not significantly altered the measured lifetime of the $17/2^+$ level. A summary of the measured lifetimes is shown in Tab. 4.2, which includes weighted averages for the $17/2^+$ and $21/2^+$ levels and the corresponding $B(E2)$ values, calculated using equation (2.24).

4.4.5 Upper Limit of the $25/2^+$ State

The $25/2^+$ state in ^{163}W is directly fed by the 603 keV $29/2^+ \rightarrow 25/2^+$ transition. Spectra were produced by demanding coincidences with the fully shifted component of the 603 keV direct feeder, however in these spectra the 555 keV $25/2^+ \rightarrow 21/2^+$ transition was fully shifted at all target-to-degrader distances and therefore the DDCM could not be applied. The shortest target-to-degrader distance at which measurements were performed corresponds to a flight time of

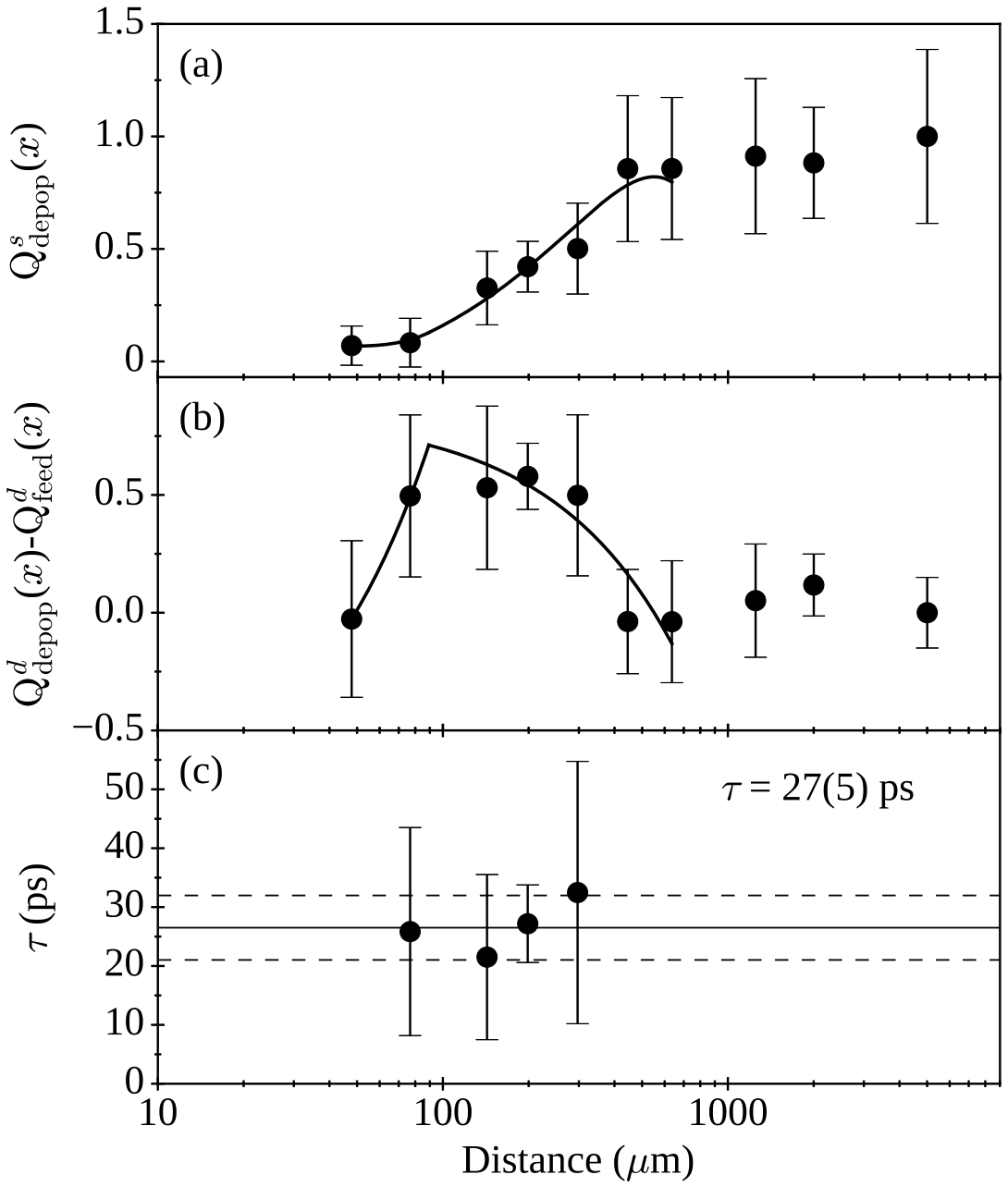

FIGURE 4.12: (a) Normalised fully shifted intensity of the transition depopulating the $17/2^+$ level measured at $\theta = 134°$. (b) Difference in intensity between the degraded components of the depopulating and feeding transitions. (c) Lifetimes measured for the $17/2^+$ level at distances within the region of sensitivity. The solid line indicates the weighted average while the dashed lines indicate the experimental uncertainty.

TABLE 4.2: Measured lifetimes and reduced transition probabilities for excited states in ^{163}W.

E_γ (keV)	$I_i^\pi \rightarrow I_f^\pi$ ($\hbar$)	Detector Angle	Recoil-correlated γ-ray coincidences	Isomer-correlated singles	Average Values	
			τ (ps)	τ (ps)	τ (ps)	$B(E2)\downarrow$ (W.u.)
384.1	$17/2^+ \rightarrow 13/2^+$	158°	21.3(30)			
		134°	21.4(30)			
		134°		26.5(50)		
					22(2)	80(8)
506.2	$21/2^+ \rightarrow 17/2^+$	158°	2.3(6)			
		134°	3.8(7)			
					3.0(4)	154(23)
554.6	$25/2^+ \rightarrow 21/2^+$	134°	$\leq$ 3.9(7)			
					$\leq$ 3.9(7)	$\geq$ 74(14)

0.1 ps. The lifetime of the $25/2^+$ state must be shorter than this flight time for the degraded component to be absent at all measured distances, setting an upper limit of 0.1 ps.

For comparison, another transition with coincidences from which to extract a lifetime was sought. The 631 keV transition is the next feeding transition in the band, however this is coincident with the 557 keV $(41/2)^- \rightarrow (37/2)^-$ transition, which would contaminate the 555 keV peak. Above the 631 keV transition is the 666 keV $(37/2)^+ \rightarrow 33/2^+$ transition, which is not coincident with the 557 keV transition, and so coincidences were demanded with this transition. In the resulting spectra, a degraded component was observed at shorter distances for the depopulating transition. As the 666 keV transition is not a direct feeder of the $25/2^+$ level, the intensity of the degraded component of the 603 keV direct feeder was required to determine the lifetime. However, the spectra produced are contaminated by transitions from a rotational band of ^{164}W featuring a 666 keV transition. This results in a strong peak at 607 keV from the $6^+ \rightarrow 4^+$ transition of this band. The degraded component of the 603 keV transition is shifted to an energy where it coincides with the contaminant 607 keV peak, and so the degraded feeding intensity could not be ascertained.

It was still possible to obtain an upper limit for the lifetime of the $25/2^+$ level by assuming that the degraded feeding intensity is equal to zero. Typical spectra of γ rays observed at $\theta = 134°$ in coincidence with the fully shifted component of the 666 keV transition are shown in Fig. 4.13. The decay curves extracted from the coincidence spectra are shown in Fig. 4.14 and give an upper limit of 3.9(7) ps.

Due to the contamination present in the spectra of γ rays coincident with the 666 keV transition, no lifetime or upper limit could be measured for the $29/2^+$ level. At higher spins, only fully shifted peaks were observed, preventing the application of the DDCM. Due to the increase of Clebsch-Gordan coefficients with increasing nuclear spin, the reduced transition probabilities typically increase moving towards

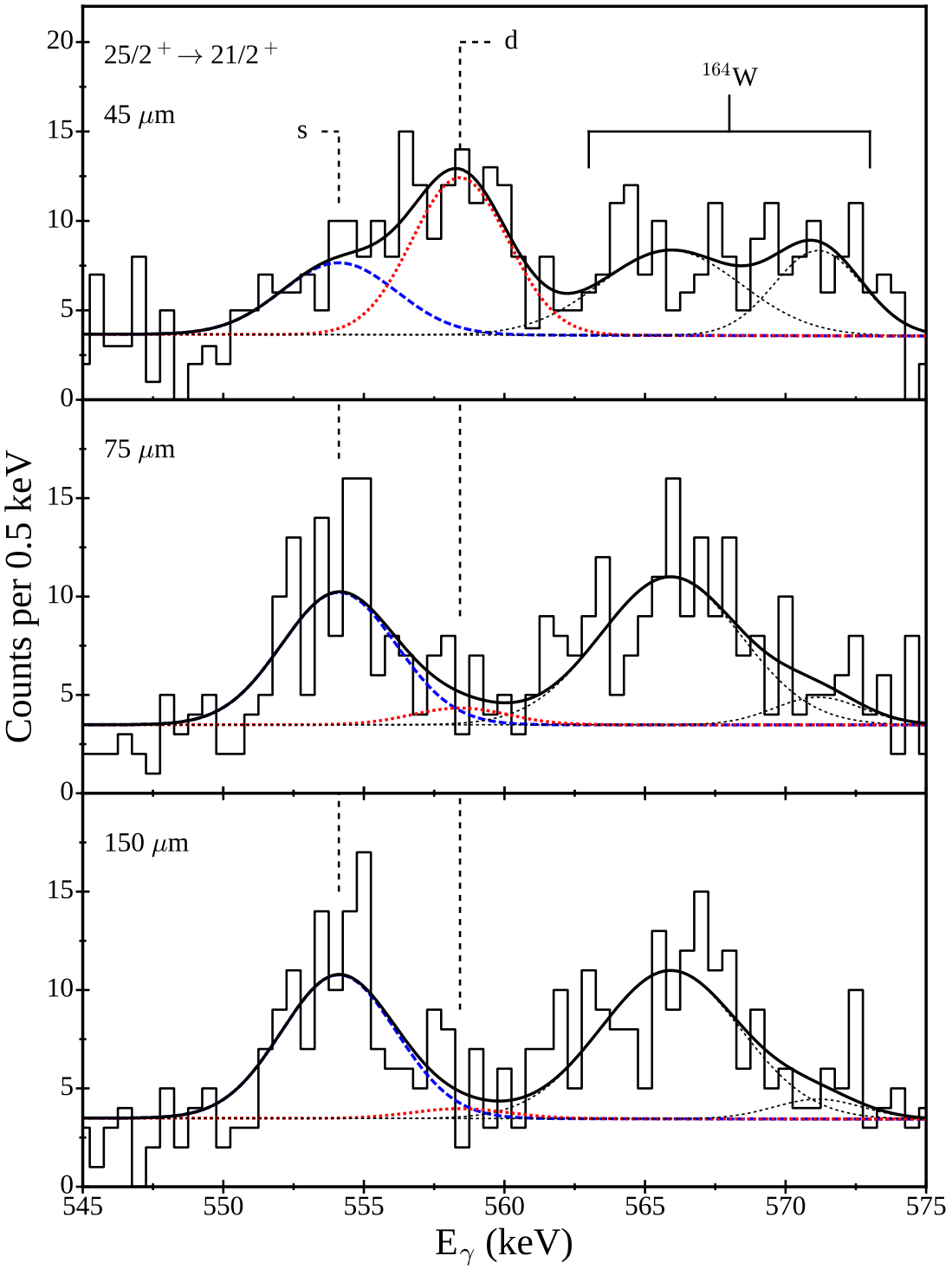

FIGURE 4.13: Gamma-ray coincidence spectra correlated with an evaporation-residue implantation in the DSSDs, measured at $\theta = 134°$. Coincidences were demanded with the fully shifted component of the 666 keV transition detected at the $\theta = 134°$ or 158° positions for all spectra shown. The dotted lines show the positions of the centroids of the fully Doppler-shifted (s) and degraded (d) components of the transition depopulating the $25/2^+$ level.

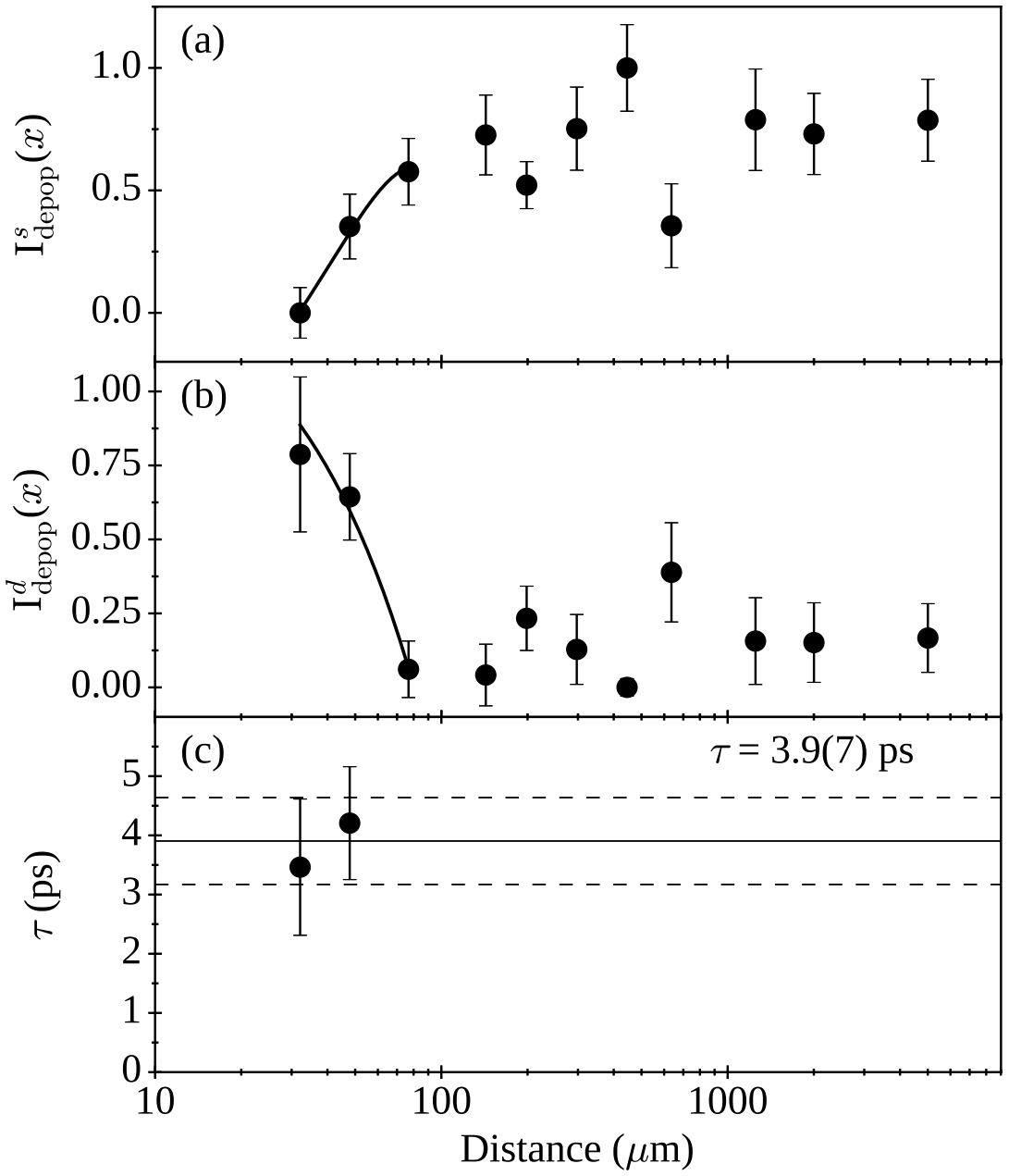

FIGURE 4.14: (a) Normalised fully shifted intensity of the transition depopulating the $25/2^+$ level measured at $\theta = 134°$. (b) Normalised degraded intensity the transition depopulating the $25/2^+$. (c) Lifetimes measured for the $25/2^+$ level at distances within the region of sensitivity. The solid line indicates the weighted average while the dashed lines indicate the experimental uncertainty.

higher spin, leading to shorter lifetimes. Eventually, the lifetimes reach the sub-picosecond level and require alternative methods to be measured, such as the Doppler-shift attenuation method (DSAM) in which lifetimes are extracted from measurements of nuclei decelerating in a stopping material.

4.5 Discussion

4.5.1 $B(E2)$ Systematics

$B(E2)$ values are a useful tool for studying nuclei due to their increased sensitivity to structural effects compared to transition energies. The $B(E2)$ values for the lowest transition in the yrast band of light tungsten isotopes are shown in Fig. 4.15(a). The even-N isotopes show a typical trend as a function of N, with maximal values in the region of the $N = 104$ midshell and dropping towards the shell closures. This is consistent with the collective model, which predicts that $B(E2)$ values increase with deformation, which is expected in midshell nuclei [7]. Although there are only two odd-N isotopes for which $B(E2)$ values have been measured, these two data points fit the established trend of the $B(E2)$ values in even-N isotopes.

The behaviour of the yrast band in ^{163}W depends on whether the unpaired neutron follows the strong coupling or decoupled scheme. Figure 4.16 shows the energy levels for states in the yrast bands of the light tungsten isotopes. The isotopes heavier than $N = 97$ feature strongly coupled bands and each of the signature partner bands is observed. With decreasing N towards $N = 97$, the positions of the levels remains largely unchanged. $N = 97$ represents a transition point at which the ordering of the signature partner levels become inverted. For $N < 97$ the unfavoured signature partner band is no longer observed, establishing a spin sequence with $\Delta I = 2$ between observed levels. The lowest levels in the odd-N isotopes follow the same trend as the corresponding levels in the neighbouring

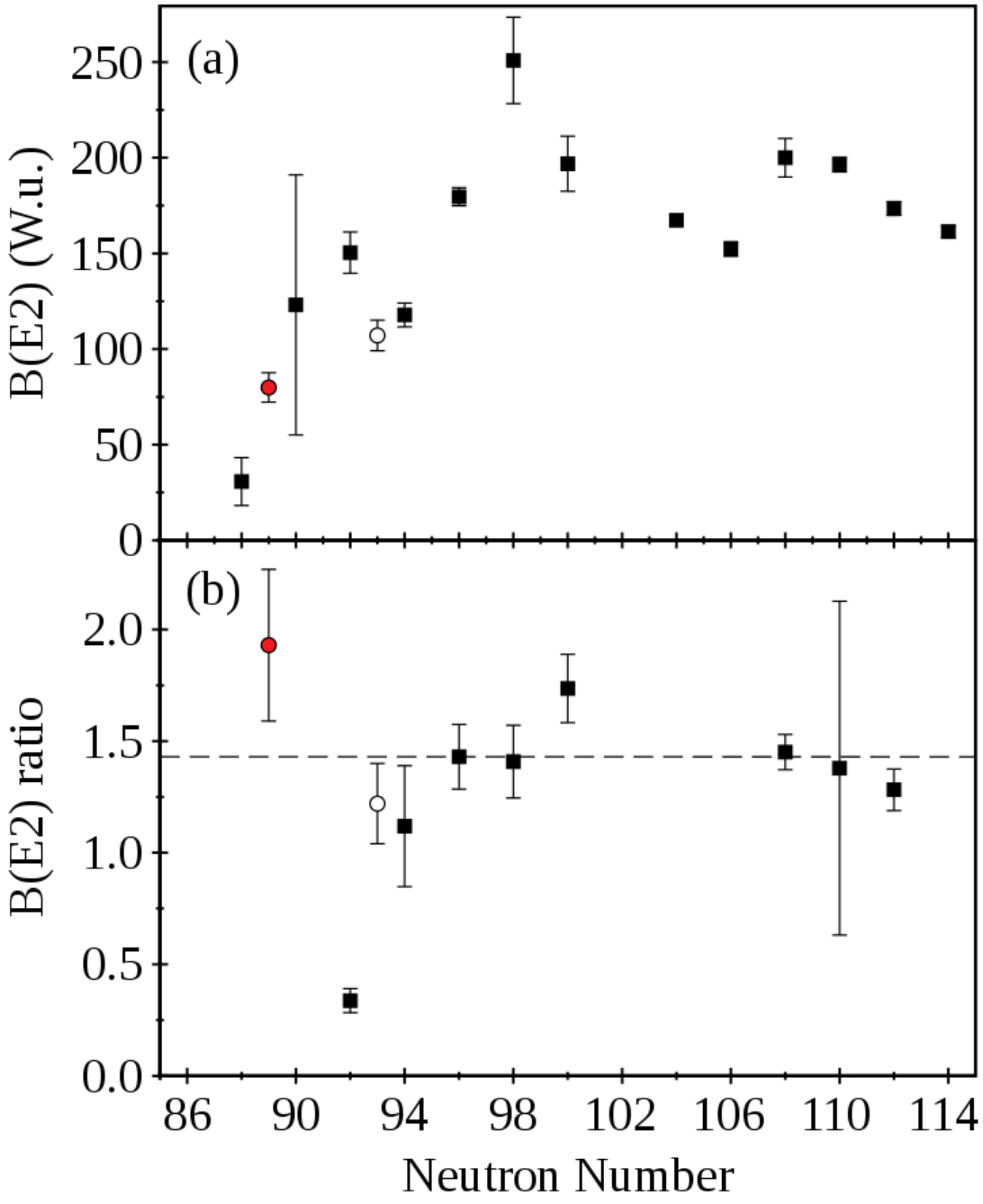

FIGURE 4.15: (a) $B(E2\colon 17/2^+ \rightarrow 13/2^+)$ values for odd-N (circles) and $B(E2\colon 2^+ \rightarrow 0^+)$ for even-N tungsten isotopes (filled squares). (b) $B(E2\colon 21/2^+ \rightarrow 17/2^+)/B(E2\colon 17/2^+ \rightarrow 13/2^+)$ ratios for odd-N isotopes and $B(E2\colon 4^+ \rightarrow 2^+)/B(E2\colon 2^+ \rightarrow 0^+)$ ratios for even-N isotopes. The dashed line is the ratio predicted by the collective rotational model for even-even nuclei. The measurements for ^{163}W are indicated by red circles. Data taken from refs. [77–88].

even-N isotopes, displaying the typical behaviour of a decoupled band. A measure of the level of decoupling can be obtained by calculating the ratio of the energy of a transition in an odd-A nucleus to the average energy of the corresponding transitions in the even-even neighbours. A completely decoupled band is expected to have $E_\gamma(17/2^+ \rightarrow 13/2^+)/E_\gamma(2^+ \rightarrow 0^+)$ and $E_\gamma(21/2^+ \rightarrow 17/2^+)/E_\gamma(4^+ \rightarrow 2^+)$ each equal to 1.0, whereas for strongly coupled bands these ratios are 5.3 and 2.9, respectively [39]. For ^{163}W, the ratios $E_\gamma(17/2^+ \rightarrow\ 13/2^+)/E_\gamma(2^+ \rightarrow 0^+) = 0.98$ and $E_\gamma(21/2^+ \rightarrow\ 17/2^+)/E_\gamma(4^+ \rightarrow 2^+) = 0.96$ identify the yrast band distinctly as following the decoupled scheme.

Taking ratios of reduced transition probabilities is useful when studying transitions between states in the same rotational band, as the contribution from the intrinsic structure is removed leaving only the dependence on geometrical factors. Recent studies have compared the ratio $B_{4/2}$ in even-N W [91], Os [19] and Pt [21] nuclei and have found anomalously low ratios in comparison to the collective model. This ratio is plotted in Fig. 4.15(b) for the tungsten isotopes. In the collective model the reduced transition probability for the transition $I{+}2 \rightarrow I$ is given by

$$B(E2:\ I+2 \rightarrow I) = \frac{15e^2Q_0^2}{32\pi}\frac{(I+1-K)(I+1+K)(I+2-K)(I+2+K)}{(I+1)(2I+3)(I+2)(2I+5)}, \tag{4.2}$$

where e is the elementary charge and Q_0 is the intrinsic quadrupole moment. In axially symmetric even-even nuclei, the projection of the total angular momentum onto the symmetry axis, K, is equal to zero. Hence, assuming that Q_0 is constant within a rotational band, a $B_{4/2}$ ratio of 1.43 is expected for an even-even ideal rotor. This ratio is known as the Alaga rule [92] and is represented as a dashed line in Fig. 4.15. In ^{163}W and ^{167}W, the neutron Fermi surface is in close proximity to high-j, low-Ω orbitals, leading to a significant Coriolis interaction which effectively decouples the odd neutron from the core rotation [39]. Consequently, **j** precesses about the rotation axis as shown in Fig. 2.5(b), resulting in an average K equal

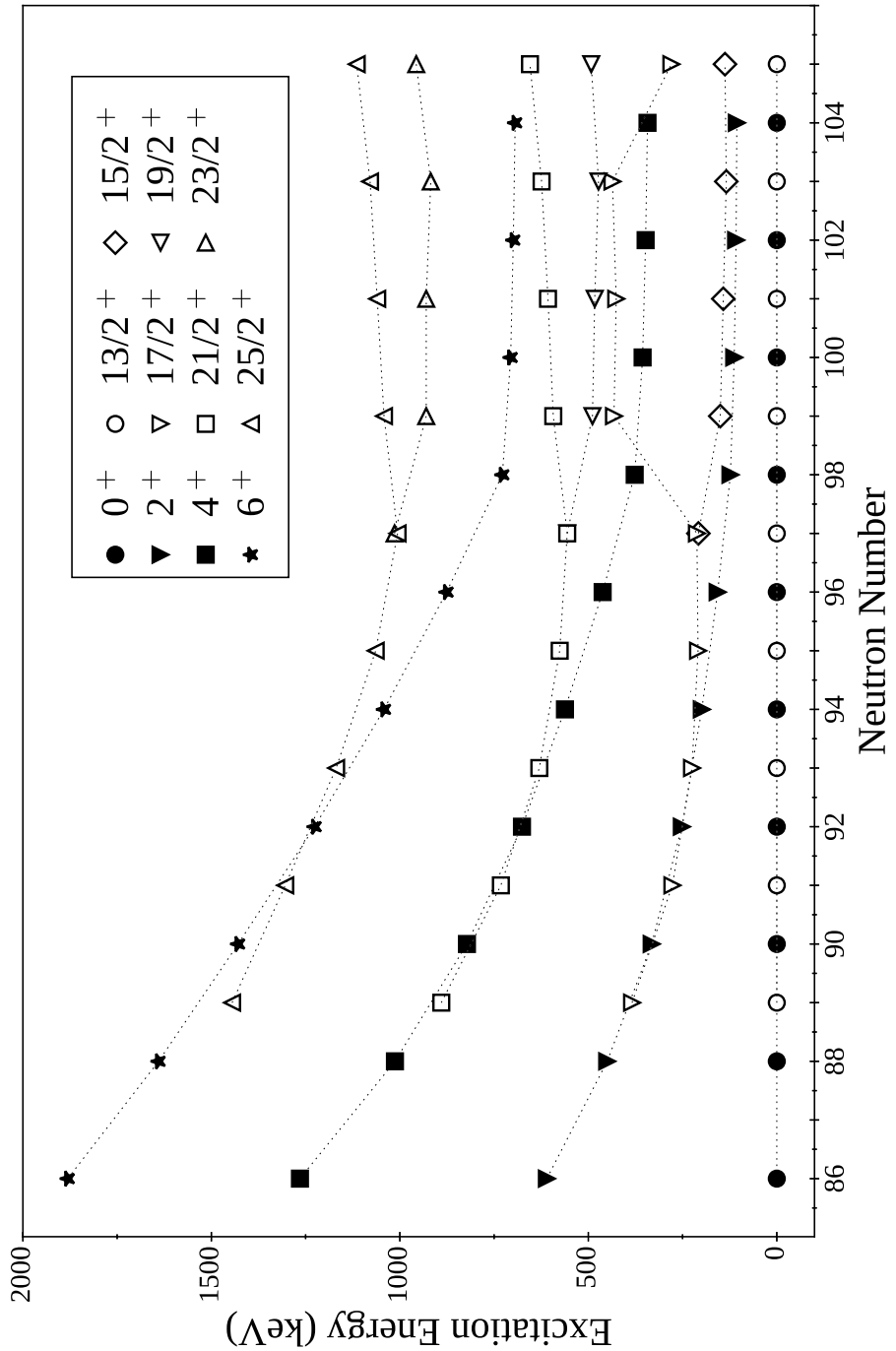

FIGURE 4.16: Systematics for the neutron-deficient even-N (filled symbols) and odd-N (open symbols) tungsten isotopes. The levels for the odd-N isotopes are plotted relative to the $13/2^+$ level. The bands in the odd-N isotopes transition from being strongly coupled at $N \geq 97$ to decoupled at $N < 97$ [13, 73, 89, 90].

to zero. Hence the $B(E2)$ values are expected to show the same behaviour as even-even nuclei and are compared with the theoretical value of 1.43.

The $B(E2)$ ratio for ^{163}W is within 2σ of the collective model value. The ratio obtained from the measurements by Li *et al.* is also in close agreement with the collective model. An odd-N nucleus can be considered as an even-even core coupled to an odd neutron or hole. The $B(E2)$ ratios for ^{162}W and ^{164}W are not known, however the ratio for ^{166}W can still give some insight into the behaviour of the even-even core, and corresponds to the core for the ^{167}W nuclide. It is clear in Fig. 4.15(b) that ^{166}W has an anomalously low $B(E2)$ ratio. It has previously been suggested that the anomalous ratios in this region of the nuclear chart could be due to a quantum phase transition between non-collective seniority and collective excitations [21]. However, as stated by Cederwall *et al.*, seniority structures are not expected in these nuclides as they are not close to a closed shell. Since the $B(E2\text{: } 2^+ \rightarrow 0^+)$ value for ^{166}W is in excess of 100 W.u. the behaviour appears to be collective, and so alternative explanations should be considered.

The collective model predicts that the $B(E2\text{: } 6^+ \rightarrow 4^+)/B(E2\text{: } 2^+ \rightarrow 0^+)$ ratio in even-even nuclei is 1.57. The $B(E2\text{: } 25/2^+ \rightarrow 21/2^+)/B(E2\text{: } 17/2^+ \rightarrow 13/2^+)$ ratio in ^{163}W is expected to be consistent with this prediction, as the $B(E2)$ values for ^{163}W are expected to show the same behaviour as those in the even-even nuclei. As an upper limit was measured for the lifetime of the $25/2^+$ level, the extracted $B(E2)$ value shown in Tab. 4.2 represents a lower limit. A ratio of $B(E2\text{: } 25/2^+ \rightarrow 21/2^+)/B(E2\text{: } 17/2^+ \rightarrow 13/2^+) \geq 0.9(2)$ was extracted, consistent with the ratio expected from the collective model.

4.5.2 Triaxiality in Transitional Even-Even Tungsten Isotopes

An impression of the nature of the nuclear deformation in the transitional tungsten isotopes can be gained by considering the proton and neutron orbitals close to the

Fermi surface. It is known that γ-soft triaxial deformations are induced by the spatial density distributions of protons and neutrons occupying the top and bottom of their shells, respectively, or vice versa [8]. The $N \sim 90$ tungsten isotopes have protons that occupy the high-Ω $h_{11/2}$ orbitals and neutrons in the low-Ω $f_{7/2}$, $h_{9/2}$ and $i_{13/2}$ orbitals, where Ω is the projection of the intrinsic angular momentum on the symmetry axis. Therefore these isotopes would be expected to have triaxial deformations.

Some information on the character of an even-even nuclide can be gained from the excitation energies of the 2^+ and 4^+ states in the ground-state band. The known $E(4^+)/E(2^+)$ ratios for the even-N tungsten isotopes are shown in Fig. 4.17(a). Isotopes close to the $N = 82$ closed shell have ratios that approximate to that of a near spherical pure vibrator with $E(4^+)/E(2^+) = 2.0$. Increasing N introduces a shape deformation, which increases to a maximum around the midshell at $N = 104$. Isotopes in the vicinity of the midshell are characteristic of strongly deformed pure rotors, for which $E(4^+)/E(2^+) = 3.33$. The $E(4^+)/E(2^+)$ values for ^{162}W, ^{164}W and ^{166}W are 2.25, 2.48 and 2.68, respectively [13, 14]. These are close to the predicted γ-soft limit of 2.5 [15]. Therefore, these isotopes are not expected to have rigid axially symmetric shapes.

Further support for γ softness in the nuclides ^{162}W, ^{164}W, and ^{166}W can be obtained by studying the evolution of the γ band in the heavier tungsten isotopes. Gamma bands refer to those in which the nucleus vibrates such that there is an oscillation in the γ parameter upon which a rotational band is formed above a bandhead with spin 2^+. This bandhead is typically the second lowest 2^+ state in energy in even-even nuclei in this region of the nuclear chart, and the position of the bandhead relative to states in the ground-state band depends on the degree of triaxiality. The evolution of the energy of the second 2^+ state with neutron number is commonly studied using the quantity

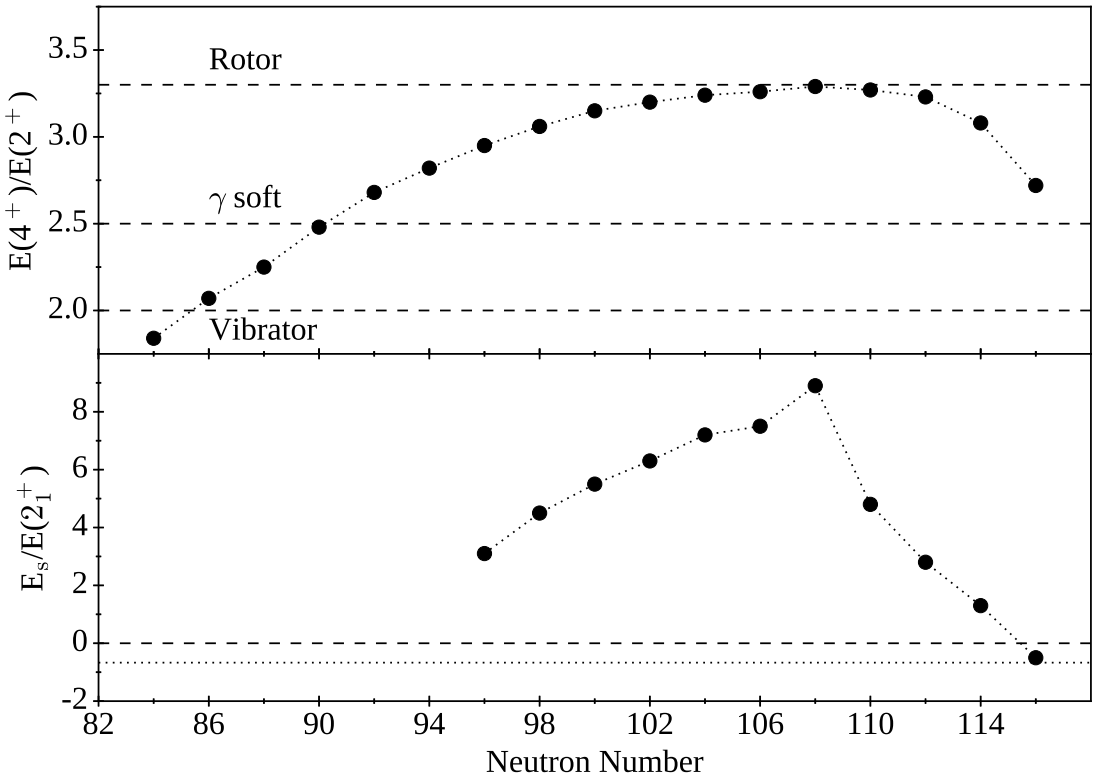

FIGURE 4.17: (a) Experimental values of $E(4^+)/E(2^+)$ for the even-N tungsten isotopes. (b) $E_s/\mathrm{E}(2_1^+)$ for even-N tungsten isotopes. The limits for γ-unstable (dashed line) and $\gamma = 30°$, rigid-triaxial (dotted line) nuclei are shown. The data are taken from Refs. [68, 90, 93]

$$\frac{E_s}{E(2_1^+)} = \frac{(E(2_2^+) - E(4_1^+))}{E(2_1^+)}. \tag{4.3}$$

The largest degree of triaxiality corresponds to $\gamma = 30°$. A nucleus that adopts a rigid triaxial shape with $\gamma = 30°$ has $E_s/E(2_1^+)$ = -0.67, according to the Davydov-Filippov model [94]. A nucleus with a flat potential with respect to γ is γ unstable and follows the Wilets-Jean limit of $E_s/E(2_1^+) = 0$, i.e. the 2_2^+ and 4_1^+ levels are degenerate [95]. In the case of axial symmetry, $E_s/E(2_1^+)$ becomes positive.

Yang *et al.* studied the trend of $E_s/E(2_1^+)$ values in the known even-even tungsten isotopes up to $N = 116$ [96], the data points for which have been reproduced in Fig. 4.17(b). The $E_s/E(2_1^+)$ value peaks at $N = 108$ and decreases towards the shell closure at $N = 82$. The γ band has only been observed down to $N = 96$. This

is because the known γ bands in the tungsten isotopes were populated via β^+ decay, whereas the lighter isotopes were produced using fusion-evaporation reactions in which the non-yrast γ band is not strongly populated. Although $E_s/E(2_1^+)$ has not been measured for $N < 96$, the decreasing trend of $E_s/E(2_1^+)$ with decreasing neutron number below $N = 108$ suggests that the $^{162-166}$W isotopes are potentially in the γ-unstable region.

The above evidence raises the question of whether γ softness could provide an explanation for the anomalous $B(E2)$ ratios observed in nearby even-even nuclei. If these nuclei are indeed γ soft then K will not be well defined. Rotational wavefunctions (2.11) depend on K, therefore a triaxial nucleus may display behaviour different from that predicted by the collective model. The Davydov model predicts $B(E2)$ values as a function of γ [94, 97]. The variation of the $B_{4/2}$ value with γ does not vary significantly from the collective model prediction of 1.43 and does not reach values as low as that of ^{166}W [98]. Therefore, the anomalous $B_{4/2}$ value measured in ^{166}W cannot be explained by a fixed γ deformation. However, the $B_{4/2}$ value may still vary significantly if the γ value is not fixed, as in a γ-soft nucleus. Hence, γ softness may be the cause of the anomalous $B(E2)$ ratios in ^{166}W.

4.5.3 Core Polarisation in ^{163}W

Despite the anomalous $B(E2)$ ratios observed in ^{166}W, the ratios for the odd-N isotopes ^{163}W and ^{167}W are consistent with the collective model. The result is therefore consistent with these nuclei being axially symmetric. This in turn implies that the odd neutron and the properties of the orbital that it occupies play a significant role in determining the shape of the nucleus.

The properties of the $\pi h_{11/2}$ and $\nu i_{13/2}$ orbitals have been studied previously in the neighbouring even-N Ta ($Z = 73$) [16, 17] and Re ($Z = 75$) [18] isotones. The rotational bands in these nuclides are coupled bands based on the unpaired

$\pi h_{11/2}$ orbital. In Ta and Re isotopes close to the $N = 104$ midshell, the states associated with each $h_{11/2}$ signature partner are equally spaced between each other in energy; there is no signature splitting present [99–103]. However, near $N = 92$ the bands exhibit clear signature splitting [16–18]. Assuming axially symmetric shapes, the theoretical quasiparticle energies for each signature of the high-Ω $h_{11/2}$ orbital calculated by Bengtsson and Frauendorf are degenerate at low rotational frequencies [104]. As such, an observed absence of signature splitting is consistent with axially symmetric deformations. The appearance of signature splitting near $N = 92$ has been interpreted as being due to the triaxiality of these nuclei since, in the cranked shell model, triaxial deformations remove the signature degeneracy of the $h_{11/2}$ orbital.

In the yrast bands in ^{161}Ta [16] and ^{163}Ta [17], a transition from a one-quasiparticle structure based on the $h_{11/2}$ proton to a three-quasiparticle structure at high spin has been established. In ^{163}Ta the three-quasiparticle structure was interpreted as being formed from the coupling of the odd proton to a pair of $i_{13/2}$ neutrons which have become aligned following a band crossing. In ^{161}Ta a pair of $h_{9/2}$, $f_{7/2}$ neutrons are the first pair to undergo a rotational alignment. Following the transition to a three-quasiparticle structure, Lagergren *et al.* showed that in bands where the $i_{13/2}$ neutron pair are the first to rotationally align, the signature splitting disappears, whereas in bands in which an $h_{9/2}$, $f_{7/2}$ neutron alignment takes place first, the signature splitting remains. It was concluded that the $\nu i_{13/2}$ orbitals strongly polarise the core while the $\nu h_{9/2}$, $f_{7/2}$ orbitals have a much weaker affect on the core.

In ^{163}Ta [17], the experimentally measured $B(M1)/B(E2)$ values for the yrast band were best described assuming γ = -15° at low spin and $\gamma = 0°$ above the back-bend in calculations based on the semi-classical formalism of Dönau and Frauendorf [105, 106]. This demonstrates a transition from triaxial deformation at low spin to an axially symmetric shape at high spin following the alignment of an $i_{13/2}$

neutron pair. The interpretation of triaxial deformation at low spin has gained further support through lifetime measurements of the yrast $15/2^-$ and $19/2^-$ states in ^{163}Ta [107]. The extracted $B(E2)$ values were applied to the particle rotor model to determine a γ value of -40°. The $B(E2)$ ratio measured for these states is inconsistent with the expectation of the collective model, which was attributed to the triaxial deformation of these states.

The same core-polarising properties of the $\nu i_{13/2}$ orbital established in the studies of the Ta and Re isotones are expected for the unpaired $i_{13/2}$ neutron in ^{163}W and in ^{167}W. An explanation for the behaviour of the $B(E2)$ ratios in the light tungsten isotopes may then be provided by considering the triaxial nature of the core and the core polarising properties of unpaired low-Ω $i_{13/2}$ neutrons. The triaxial deformation in ^{166}W which results in anomalous $B(E2)$ ratios is not present in ^{163}W, as the $i_{13/2}$ neutron forces the γ-soft core into an axially symmetric prolate shape due to its spatial orientation in the equatorial plane. The precession of **j** about the rotation axis results in an average K of zero and consequently the collective model predictions for even-even nuclei become applicable to ^{163}W and ^{167}W.

4.6 Summary

Using the recoil-distance Doppler-shift method, lifetimes of excited states in the $i_{13/2}$ band in ^{163}W have been measured for the first time. The corresponding $B(E2)$ reduced transition probabilities have been extracted, allowing $B(E2)$ ratios to be calculated and interpreted in terms of the collective model of Bohr and Mottelson [7]. The ratios were found to be consistent with the predictions of the collective model for even-even nuclei.

The $B(E2\text{: } 21/2^+ \rightarrow 17/2^+)/B(E2\text{: } 17/2^+ \rightarrow 13/2^+)$ ratio was compared to the established $B_{4/2}$ ratios in the neighbouring even-N tungsten isotopes. The $B(E2)$ ratio of ^{163}W and that measured previously for ^{167}W [88] are in stark

contrast to that of ^{166}W, which has an apparently anomalous ratio [20]. The $E(4^+)/E(2^+)$ ratios and $E_s/E(2_1^+)$ systematics of light tungsten isotopes suggest that the ^{162,164,166}W nuclides have γ-soft deformations [96]. As the K quantum number is not a well-defined quantity for γ-soft nuclei, the $B(E2)$ ratio predicted by the collective model is not applicable for these nuclides. Gamma-soft deformations may be the cause of apparently anomalous $B(E2)$ ratios observed in other nuclei in this region of the chart of nuclides.

The consistency of $B(E2)$ ratios in the odd-A tungsten isotopes with the collective model can be understood in terms of the properties of the orbital occupied by the unpaired neutron in these nuclides. In the $\nu i_{13/2}$ bands the ^{163,167}W nuclides are strongly influenced by the Coriolis force due to the odd neutron occupying a high-j, low-Ω orbital. The strength of the Coriolis force effectively decouples the odd neutron from the core rotation and excitation of the nucleus proceeds by the rotational excitation of the even-even core. Previous studies of the neighbouring Ta [16, 17] and Re [18] isotones have indicated that the $i_{13/2}$ neutron orbital is strongly polarising. Therefore, it is inferred that the $i_{13/2}$ neutron in ^{163}W polarises the γ-soft core, resulting in an axially symmetric prolate shape. The rotational alignment of the odd neutron and the axial symmetry of the nucleus lead to a $B(E2)$ ratio that is consistent with the ratio predicted for an even-even nuclide.

Chapter 5

Decay of a 19^- Isomeric State in ^{156}Lu

5.1 Introduction

The transitional nuclei studied in the previous chapter display a combination of single-particle and collective behaviour. The structure of nuclei near to closed shells is dictated by the behaviour of a few valence nucleons and therefore provide a better opportunity to study the properties of single-particle orbitals. In heavy nuclei, the valence nucleons can occupy orbitals with large orbital angular momentum. This can lead to multiparticle states with large spins at relatively low energies. A low transition energy and a large spin change between two states can lead to the formation of an isomeric state. For a state to be considered isomeric, it must be long lived in comparison to the other excited states of the considered nuclear species. Long lifetimes are a consequence of a reduced overlap between initial and final wavefunctions, hindering the decay of the state [108]. Multiparticle spin-trap isomers generated by the various angular momentum couplings of valence nucleons provide a useful opportunity for studying how nucleon-nucleon interactions evolve with changing proton or neutron numbers.

Examples of multiparticle spin-trap isomers are found in the odd-odd, proton-rich $N = 85$ isotones [109–113]. The three valence neutrons available in these isotones are able to couple to the valence protons to form multiparticle isomers. The isotone ^{152}Ho features a 19^- isomer, which has been assigned a configuration consisting of three valence neutrons in an $(f_{7/2}h_{9/2}i_{13/2})_{29/2^+}$ state coupled to three protons [111]. The three valence protons appear to be in the j-1 state, as the assumption of a seniority 1 $(\pi h^3_{11/2})_{11/2}$ configuration would result in a spin and parity of 20^- for the isomer, which is incompatible with the observed spin and parity. This is an example of the "J-1" anomaly, which has been observed in a number of cases in this region of the chart of nuclides [114]. Recently, a 19^- isomer has been observed in ^{158}Ta, which has been assigned the same configuration as the 19^- isomer in ^{152}Ho, based on the similarity of the characteristics of these isomers [109, 110]. The isotone ^{156}Lu is two protons lighter than ^{158}Ta, and was expected to have an isomer with the same structure as its neighbouring odd-odd isotones.

Previous studies of ^{156}Lu have focussed on prompt γ-ray transitions. Ding *et al.* established the yrast transitions built upon a high-spin isomer decaying by α emission to which a spin-parity of 10^+ [115] was assigned. The level scheme developed from the coincidence analysis is shown in Fig. 5.1. Additional transitions were observed that could not be placed into the level scheme and were assumed to originate from the decay of nonyrast states built on the lowest-lying 9^+ state.

Following the prompt studies by Ding *et al.*, McPeake identified a 19^- isomer in ^{156}Lu which has similar characteristics to the 19^- isomers observed in ^{152}Ho and ^{158}Ta [116]. This chapter outlines the results of further investigation of the isomer. Additional γ-ray transitions depopulating the isomer have been identified and their path to the α-decaying 10^+ state has been elucidated. The half-life of the isomeric state has been measured, which when compared to Weisskopf estimates for the transitions directly depopulating the isomer support the assignment of the isomer as a 19^- state. The results are discussed in the context of the neighbouring $N = 85$ isotones.

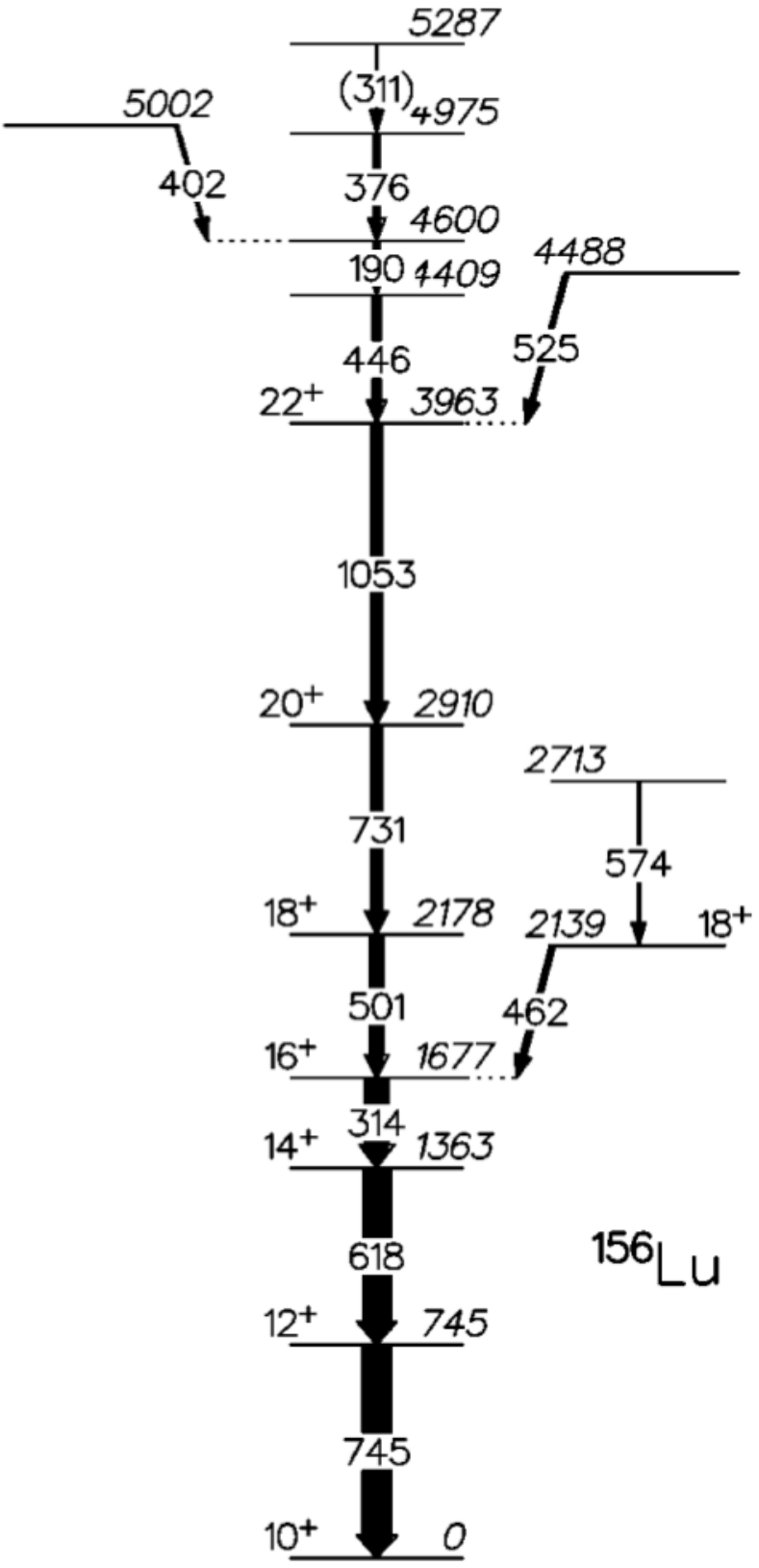

FIGURE 5.1: The level scheme developed by Ding *et al.* above the 10^+ isomer, where the energies are in keV and the widths indicate the intensity of the transition. Taken from Ref. [115].

5.2 Experimental Details

In order to populate excited states in ^{156}Lu, the ^{106}Cd(^{58}Ni,3p1n1α)^{156}Lu fusion-evaporation reaction was employed in an experiment at the Accelerator Laboratory of the University of Jyväskylä. The target was isotopically enriched cadmium with a thickness of 975 μg/cm^2. A beam energy of 318 MeV was used for 292 hours. Fusion-evaporation residues were transported by RITU to the GREAT spectrometer positioned at its focal plane. Three clover type germanium detectors and a planar germanium detector were positioned at the focal plane, which measured γ rays emitted by isomeric decays at the focal plane.

5.3 Results

5.3.1 Gamma-Ray Coincidence Analysis

Delayed emissions caused by isomeric states allow transitions that follow isomeric decays to be observed in the GREAT spectrometer, eliminating the background of prompt transitions observed at the target position. The higher-energy α decay of ^{156}Lu is characterised by a decay energy of 5565(4) keV and a half-life of 198(2) ms [117]. The α decay has been used to select delayed γ rays following the decay of higher-lying isomeric states recorded in the focal-plane germanium detectors. Figure 5.2(a) shows a background subtracted spectrum of γ rays measured by the focal-plane clover detectors within 0.5 μs of the implantation of an evaporation residue into one of the DSSDs that was followed within 576 ms by a ^{156}Lu α decay in the same pixel. Gamma rays from long-lived decays were removed by subtracting a spectrum consisting of γ rays measured in the clover detectors 0.5 – 1.0 μs before a ^{156}Lu implantation. Gamma rays associated with random correlations of evaporation residues with α decays were removed by subtracting a spectrum consisting of γ rays recorded in the clover detectors within 0.5 μs of

TABLE 5.1: Gamma-ray energies and intensities relative to that of the 759.4 keV transition for transitions below the 19^- isomer in ^{156}Lu. Energies are accurate to ±1 keV. Intensities have been corrected for the efficiency of detection. Note that at least one of the 580.5 and 765.0 keV γ rays is a doublet and due to this ambiguity the mean energies and total intensities are listed for these γ-ray peaks.

E_γ (keV)	I_γ (%)
62.3	42(3)
126.0	6.1(5)
130.5	2.3(5)
180.3	3.3(4)
253.5	2.6(5)
279.0	3.7(5)
303.5	17.8(9)
307.1	68.1(16)
310.3	15.3(9)
314.0	33.6(10)
364.7	98.0(17)
371.4	4.1(5)
517.5	6.6(9)
524.0	96.9(15)
580.5	43.3(13)
583.7	72.8(15)
618.3	55.5(11)
642.8	6.6(6)
657.0	5.6(5)
682.4	4.4(4)
744.8	54.0(12)
759.4	100.0(16)
765.0	39.6(11)
776.9	4.5(4)
814.8	4.8(4)
881.7	7.2(5)
923.9	30.8(9)
944.2	7.0(5)

the implantation of an evaporation residue that was *preceeded* within 576 ms by a 5565-keV decay in the same pixel. The energies and relative intensities of the γ-ray transitions observed in this spectrum and the corresponding planar detector spectrum are shown in Tab. 5.1.

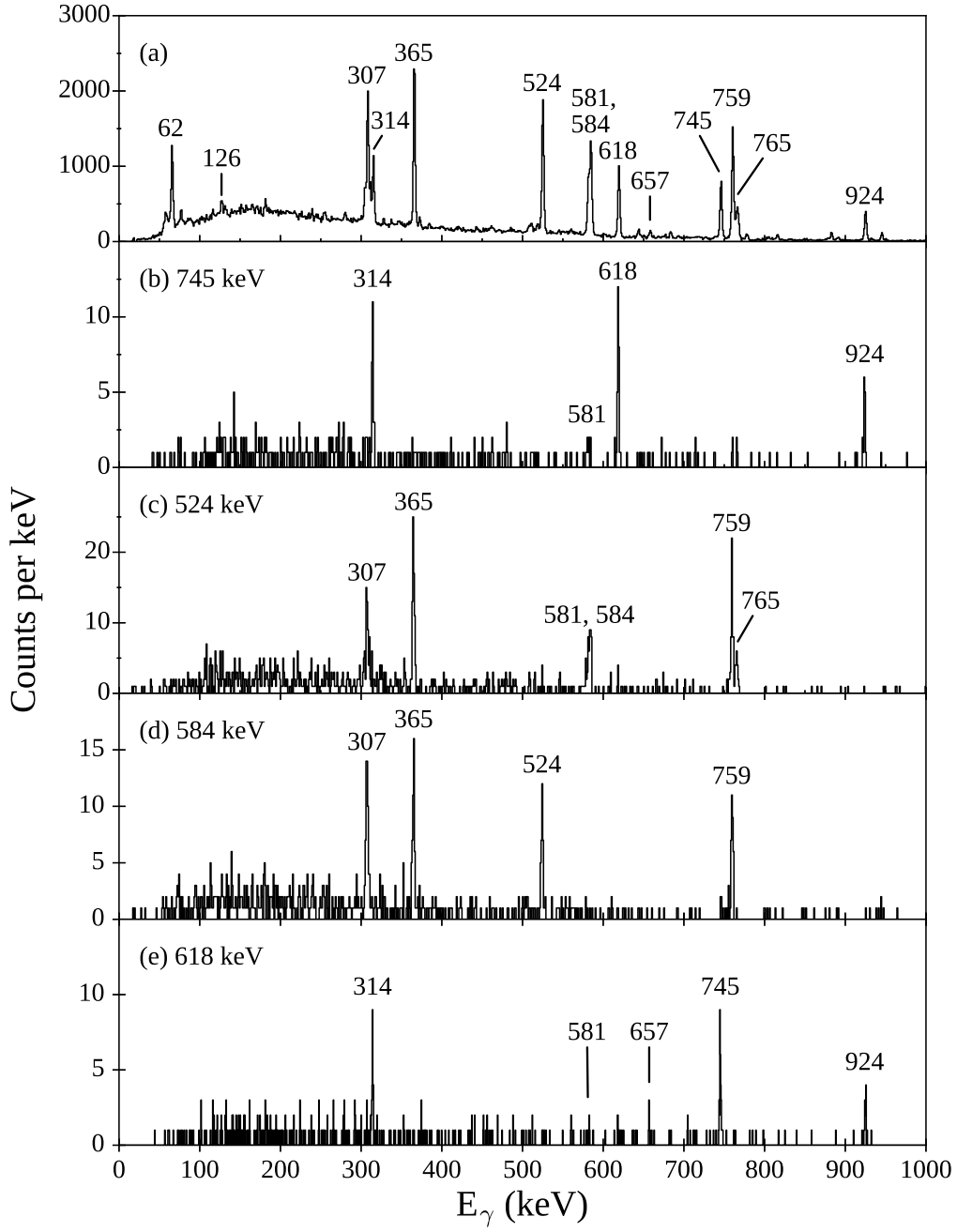

FIGURE 5.2: Energy spectra of γ rays observed in the focal-plane clover detectors. All γ rays were recorded within 0.5 μs of an evaporation-residue implantation into the DSSDs that was followed in the same DSSD pixel by a 5565-keV ^{156}Lu α decay within 576 ms. (a) Background-subtracted singles energy spectrum. Gamma rays in (a) that were detected in coincidence with a γ ray of energy (b) 745 keV, (c) 524 keV, (d) 584 keV and (e) 618 keV.

Figure 5.2(b) shows the energy spectrum of γ rays observed in the clover detectors in coincidence with the 745 keV transition. The 314 and 618 keV transitions observed by Ding *et al.* [115] are present along with the 924 keV transition observed by McPeake [116]. Figure 5.2(c) shows transitions in coincidence with the 524 keV transition. There are no common coincidences between the 745 and 524 keV transitions, indicating the existence of an alternative decay path linking the 19^- state to the α-decaying state which has not previously been placed in the level scheme. Figure 5.2(d) shows γ rays correlated with the 584 keV transition. The spectra shown in figures 5.2(c) and (d) have three γ rays in common: the 307, 365 and 759 keV γ rays. However, Fig. 5.2(c) features peaks at 581 and 765 keV, which are not present in Fig. 5.2(d), indicating that the decay path must branch such that the 584 keV transition forms a separate decay path to the 581 and 765 keV transitions. Figure 5.2(e) shows transitions in coincidence with the 618 keV transition, featuring the weak 657 keV transition and traces of the 581 keV transition, which, although weak can be seen more clearly in Fig. 5.2(b). Therefore the 581 and 657 keV transitions appear to link the isomer to the (314, 618, 745) sequence.

Figure 5.3 shows energy spectra of photons which were observed in the planar detector in coincidence with γ rays recorded by the clover detectors, correlated with a ^{156}Lu ion implantation. Three distinct transitions with energies of 304, 307 and 310 keV can be seen in these spectra. Figure 5.3(a) shows γ rays that were coincident with a 581 keV γ ray, in which there are two peaks in close proximity to each other, one at 304 keV and one at 310 keV. Both of these γ rays are absent in the spectrum of γ rays coincident with a 584 keV γ ray shown in Fig 5.3(b), and are replaced by a single peak at 307 keV. The observed coincidences indicate that the 307 and 584 keV transitions form a parallel path to the 310 and 581 keV transitions. The two paths then recombine to allow coincidences between each of the parallel paths and the γ rays of the (365, 524, 759) sequence. In the level scheme, the ordering of the 307 and 584 keV transitions is based on the 584 keV γ ray being observed at the target position by Ding *et al.* [115] and in the present

study, while the 307 keV γ ray was absent. Figure 5.3(c) shows γ rays coincident with the 765 keV transition, in which a 126 keV γ ray is observed. This transition is absent in figures 5.3(a) and (b) and therefore a (126, 765) sequence forms a third path from the 19$^-$ isomer that is parallel to the (307, 584) and (310, 581) paths.

Figure 5.4 shows further energy spectra of photons measured in the planar detector in coincidence with photons measured in the clover detectors. The 62 keV transition is seen to be coincident with a 759 keV γ ray in Fig. 5.4(a), but not with a 745 keV γ ray in Fig. 5.4(b), suggesting that a 62 keV γ-ray transition exists in parallel to the 745 keV transition. The K$_\beta$ x rays for Lu have energies of $\sim$ 62 keV [118], therefore careful consideration is needed to assign a 62 keV transition to ^{156}Lu. The K$_\beta$ x rays have an intensity that is approximately one quarter of that of the K$_\alpha$ x rays [118]. The intensity of the peak at 62 keV is greater than would be expected if K$_\beta$ x rays were the sole component of the peak. The excess of counts is therefore consistent with a 62 keV γ-ray transition.

Figure 5.5 shows a partial energy level scheme consisting of transitions occurring below the 19$^-$ isomer, constructed from the coincidence analysis. Other transitions listed in Tab. 5.1 could not be placed in the level scheme due to insufficient statistics. The γ-ray coincidences are consistent with a decay path consisting of γ rays with energies 304 and 581 keV connecting the 1836 keV 16$^+$ state to the 952 keV 12$^+$ state, parallel to the (126, 365, 524) path. Equally, there could be a decay path consisting of γ rays with energies 304 and 765 keV connecting the 2021 keV 16$^+$ state to the same 12$^+$ state that would run parallel to the (310, 365, 524) path. It is possible that both paths are present in the level scheme. Hence, at least one of the 581 and 765 keV transitions is a doublet. This ambiguity leads to uncertainties in the branching ratios of the 581 and 765 keV transitions directly depopulating the 19$^-$ isomer. Hence there are also large uncertainties in the reduced transition probabilities for these transitions, which are discussed in section 5.4.5.

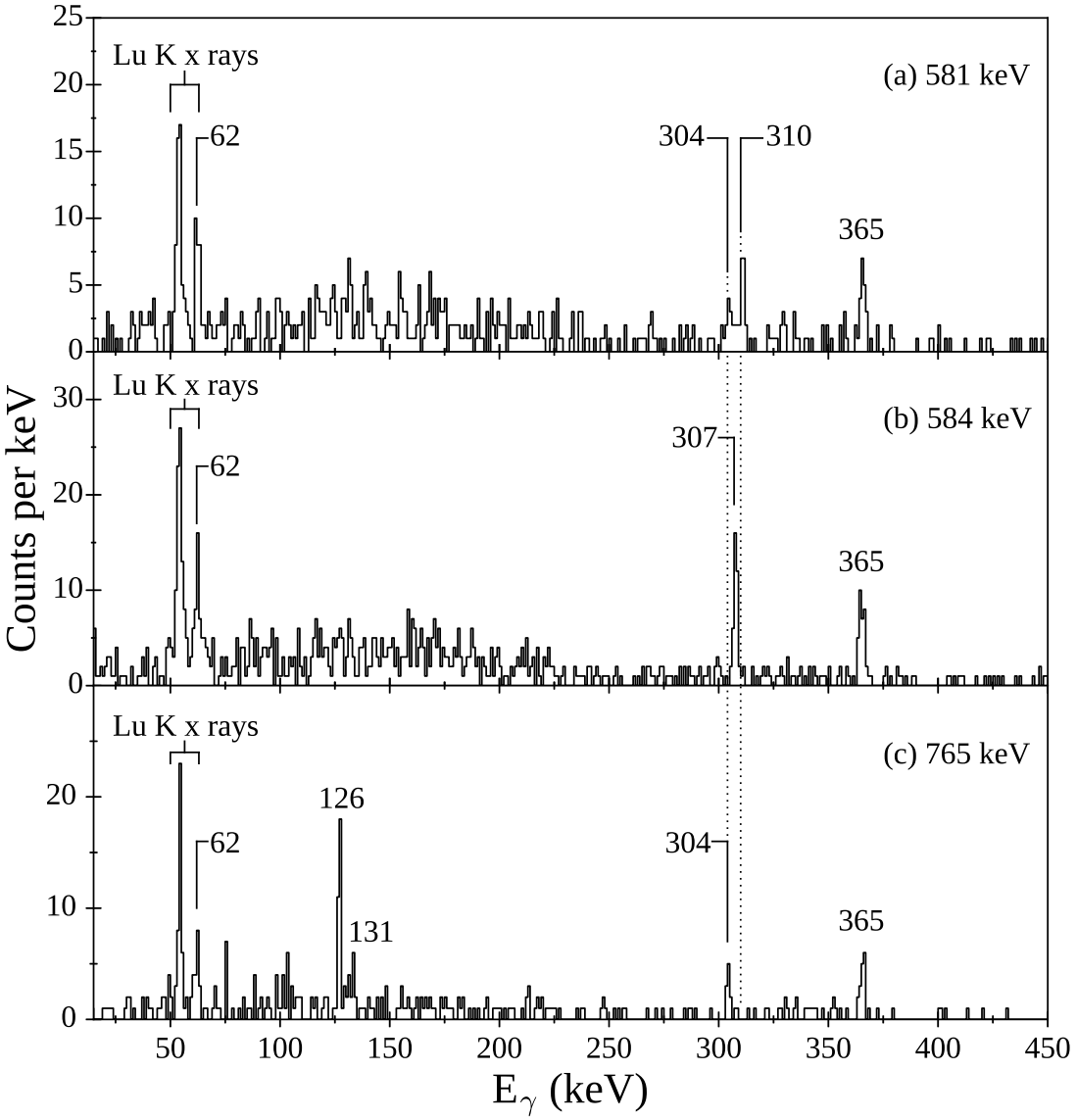

FIGURE 5.3: Energy spectra of γ rays observed in the planar detector coincident with γ rays recorded by the clover detectors. Gamma rays are selected that occur within 0.5 μs of the implantation of an evaporation residue into the DSSDs that was followed in the same pixel by a 5565-keV ^{156}Lu α decay within 576 ms of implantation. Gamma rays coincident with (a) 581 keV, (b) 584 keV and (c) 765 keV γ rays measured by the clover detectors. Three distinct transitions are seen in the 304-311 keV region.

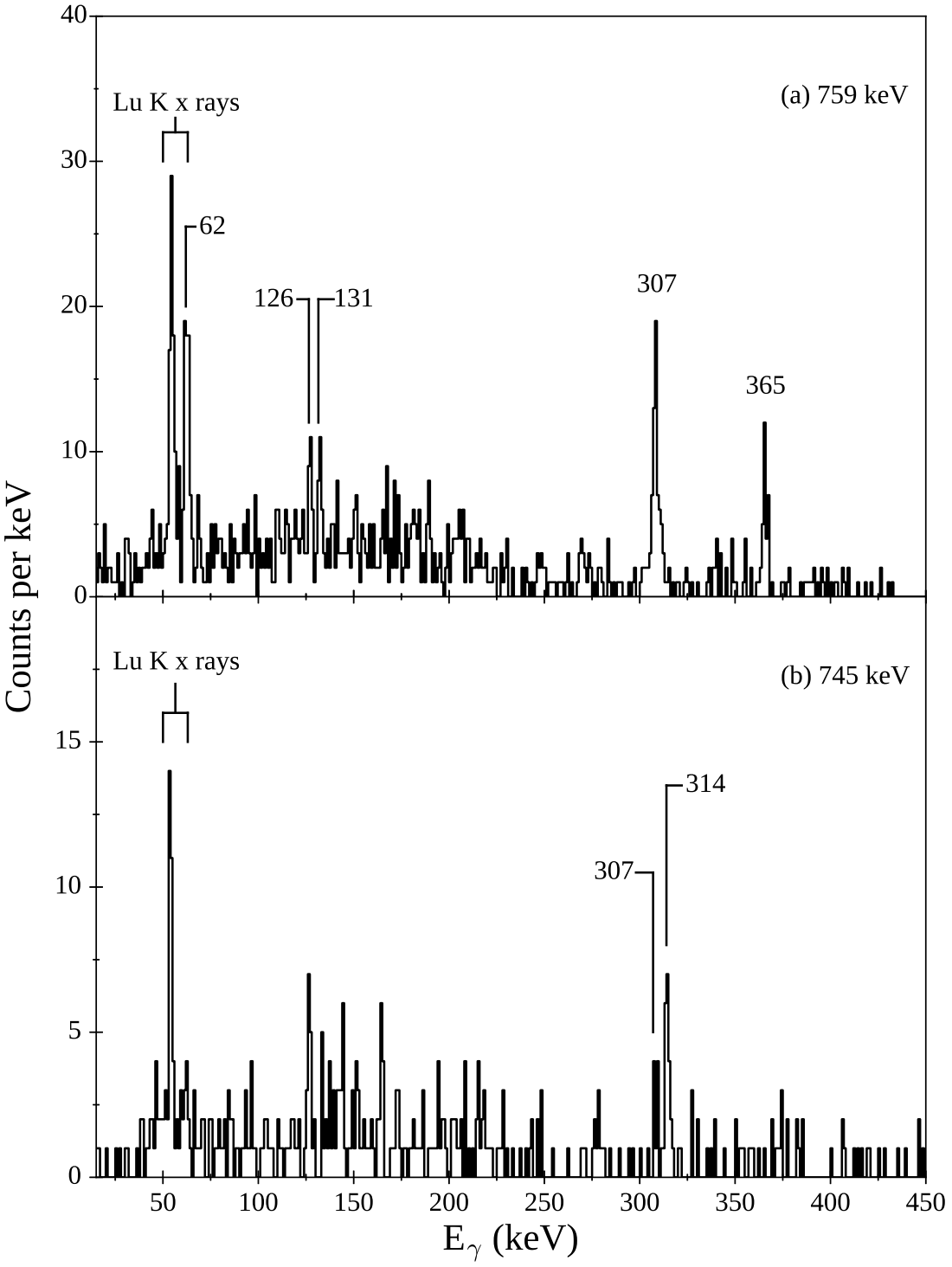

FIGURE 5.4: Energy spectra of photons observed in the planar detector coincident with (a) a 759 keV γ ray or (b) a 745 keV γ ray in the clover detectors. Gamma rays are selected that occur within 0.5 μs of the implantation of an evaporation residue into the DSSDs that was followed in the same pixel by a 5565-keV ^{156}Lu α decay within 576 ms of implantation. The cluster of coincidences at 307 keV in (b) could be explained if a weak decay path exists, missing from Fig. 5.5, which links the 2294 keV level to the 745 keV level.

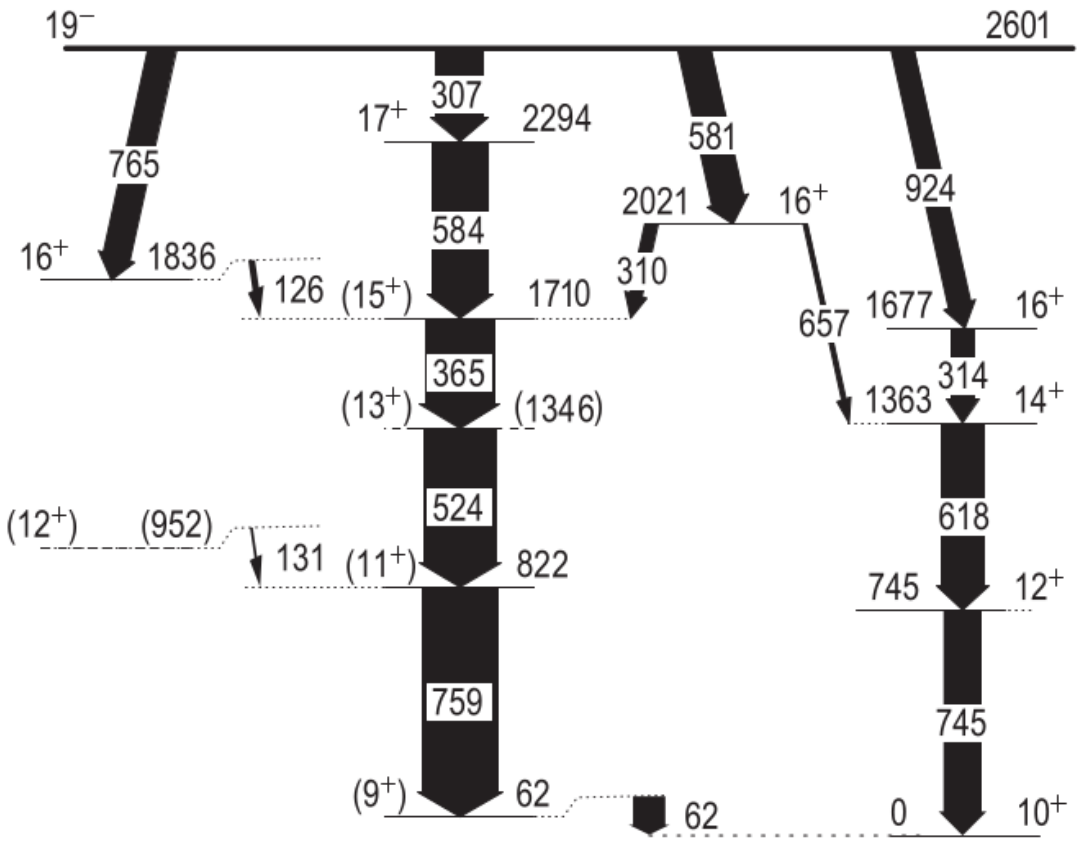

FIGURE 5.5: Partial energy level scheme for ^{156}Lu showing decay paths from the 19^- isomer. Transitions too weak to place are omitted. The widths of the arrows are proportional to the measured γ-ray intensities. Note that at least one of the 581 and 765 keV γ rays is a doublet and due to this ambiguity the widths of these arrows are proportional to the total intensities for each of these γ-ray peaks.

The intensity of the 924 keV transition was used to estimate the isomeric ratio of the 19^- isomer. With $\sim$ 20 million events in the ^{156}Lu α-decay peak in the DSSDs, a ratio of $\sim$ 5% was calculated after correcting for efficiency and in-flight decay losses in RITU.

5.3.2 Contaminants

Some weaker transitions present in Fig. 5.2(a) could not be placed. These include transitions at 254 keV and 777 keV, which are close in energy to the 253 keV

$16^+ \rightarrow 14^+$ transition and the 778 keV transition to the 9^+ state in ^{158}Ta, respectively (see Fig. 5.6 for the level scheme developed by Carroll *et al.* [110]). The reaction ^{106}Cd(^{58}Ni,1p1n1α)^{158}Ta has a significant production cross section at the beam energy employed in the experiment. The 9^+ state in ^{158}Ta has a 100(8)% α-decay branching ratio with a decay energy of 6048(5) keV and half-life of 37.7(15) ms [119]. It is possible that some α decays from the 9^+ state in ^{158}Ta met the criteria intended to identify ^{156}Lu decays, which would allow some γ decays from ^{158}Ta to appear in Fig. 5.2(a). The 746 keV $12^+ \rightarrow 10^+$ transition in ^{158}Ta has the potential to make a contribution to the intensity of the 745 keV peak identified in Fig. 5.2(a), however the absence of a peak at 598 keV suggests that ^{158}Ta γ rays do not contribute a significant number of counts to the spectrum.

Figure 5.7(a) shows an energy spectrum of decay events in the DSSDs. The region indicated by the dotted lines consists of higher-energy α particles whose energy is partially deposited in the DSSDs, which may include α particles from the decay of the 9^+ state in ^{158}Ta. The region gives an indication of the contribution of γ rays correlated with higher-energy α decays to the spectrum shown in Fig. 5.2(a). Figure 5.7(b) shows the energy spectrum of γ rays detected within 0.5 μs of the implantation of an evaporation residue that was followed by a decay in the same pixel within 576 ms, with a decay energy within the limits indicated in Fig. 5.7(a). The 253, 598, 746 and 1002 keV γ rays correspond to transitions in ^{158}Ta following the decay of a 19^- isomer. The 746 keV peak is close to the background level and therefore is unlikely to make a significant contribution to the measured intensity for the 745 keV transition in ^{156}Lu listed in Tab. 5.1. The intensity of the 253 keV peak in Fig. 5.7(b) suggests that the transition in ^{158}Ta could contribute to the 254 keV peak in Fig. 5.2 but cannot account for the full intensity of the peak, and the 778 keV transition is absent. Therefore the 254 and 777 keV γ ray peaks observed in Fig. 5.2(a) are assigned as ^{156}Lu transitions.

The ^{156}Lu α-decay peak in Fig 5.7(a) also rests on the low-energy tails of α decays originating from two states in ^{155}Lu and one in ^{157}Hf. Known transitions

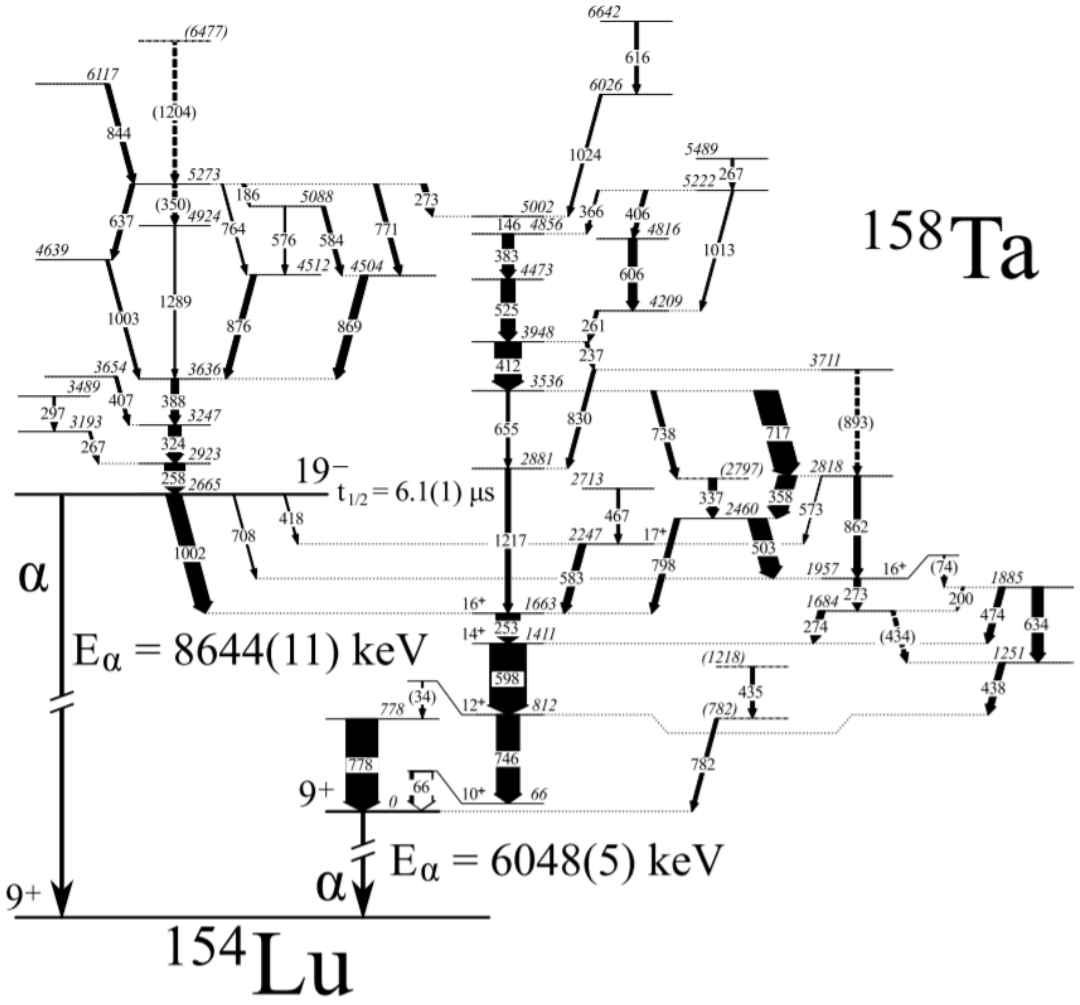

FIGURE 5.6: The level scheme developed by Carroll *et al.* for transitions above the 9^+ isomer in ^{158}Ta, where the energies are in keV and the widths indicate the intensity of the transition. Taken from Ref. [110].

following the decay of isomers in these nuclei are not present in Fig. 5.2(a).

5.3.3 Half-Life of the 19^- Isomeric State

Decay curves were produced for the strongest transitions identified in Fig. 5.2(a). Figure 5.8 shows a selection of the decay curves. For each decay curve the half-life was extracted by a weighted fit of an exponential plus a constant background. Figure 5.9 shows the extracted half-lives as a function of γ-ray energy. The measured half-lives are mutually consistent, therefore the measurements are consistent with these transitions following the decay of a common isomeric state. The statistics

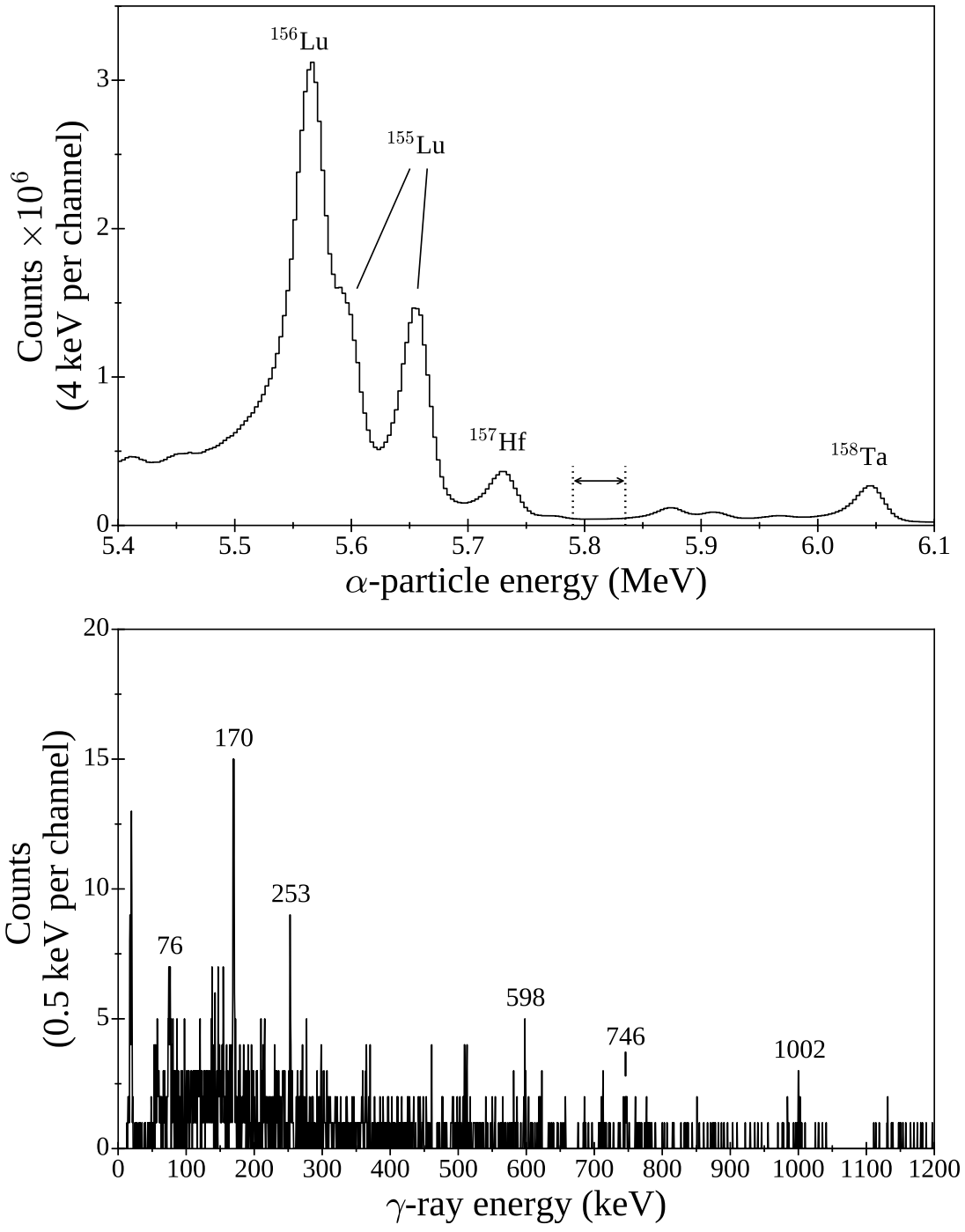

FIGURE 5.7: (a) Energy spectrum of decay events (no signal in the MWPC) in the DSSDs. (b) Energy spectrum showing γ rays observed in the clover detectors within 0.5 μs of an evaporation-residue implantation followed by a decay in the same pixel within 576 ms with a decay energy within the limits indicated by the dotted lines shown in (a).

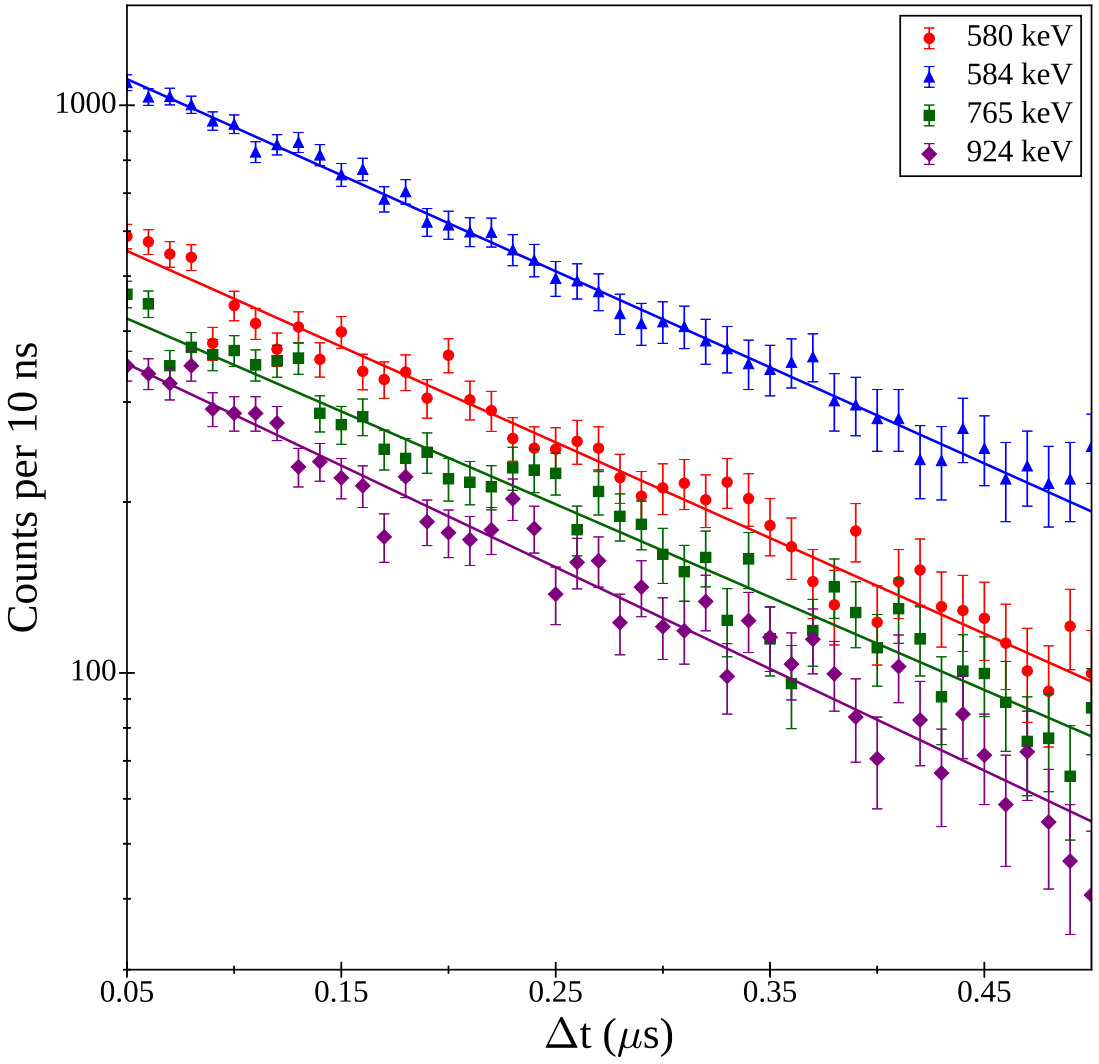

FIGURE 5.8: Selected decay curves for transitions below the 19⁻ isomer measured in the clover detectors. A constant background has been subtracted. The fitted line is shown for each of the listed γ ray energies.

of the strongest peaks were combined and a half-life of $t_{1/2} = 179 \pm 4$ ns was extracted from the decay curve shown in Fig. 5.10. If multiple isomeric states exist with distinct half-lives, the Compton background will consist of γ rays with different half-lives, adding multiple components to each decay curve. Hence, to minimise the contribution from the Compton background, only transitions with an energy greater than 500 keV have been used to determine the half-life of the isomer.

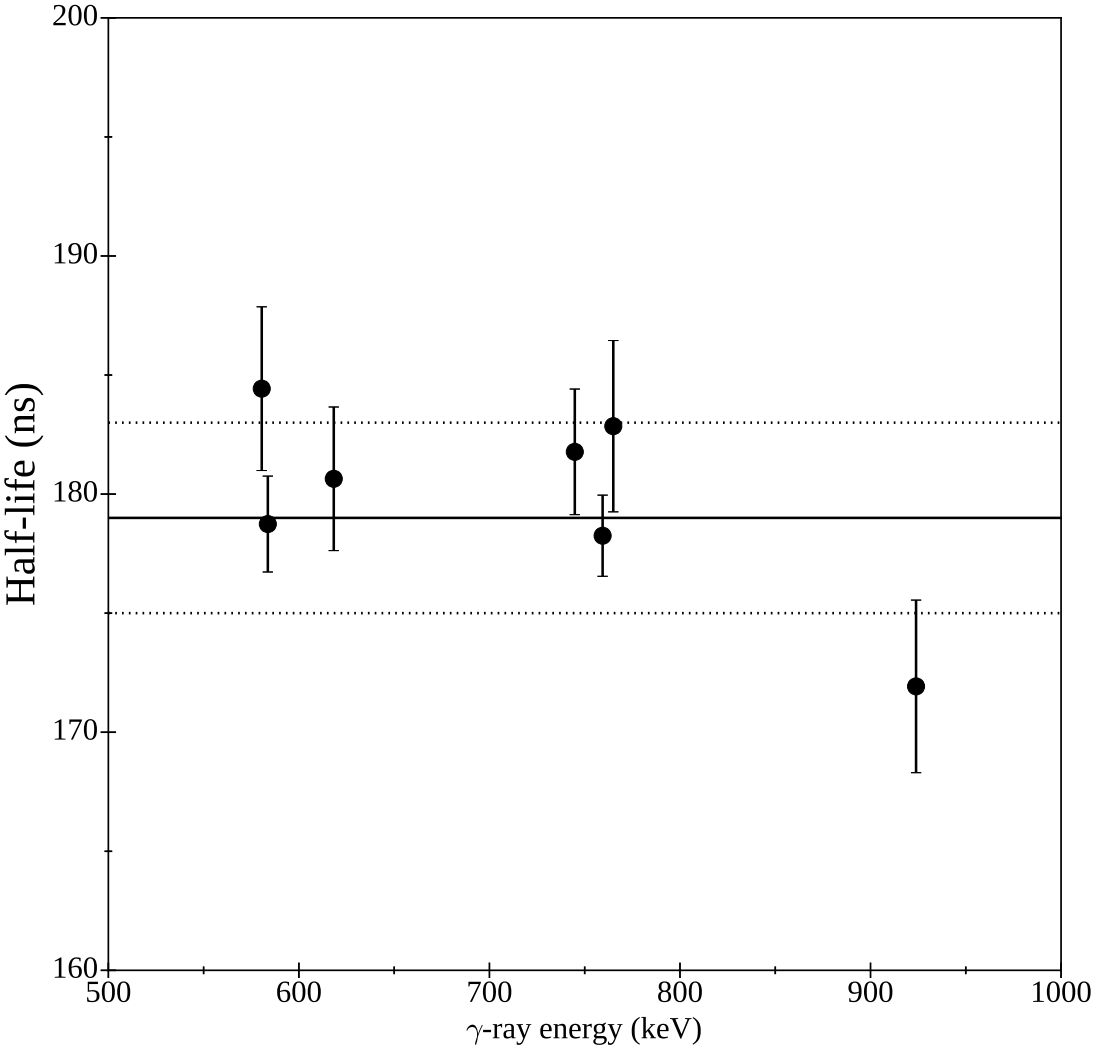

FIGURE 5.9: Half-lives extracted for γ-ray transitions occurring below the 19^- isomer. The solid line indicates the half-life extracted from the sum of the decay curves of each γ ray plotted (see Fig. 5.10) while the dotted lines indicate the experimental uncertainty.

5.4 Discussion

5.4.1 Spin-Parity Assignments

The multipolarity of a transition can be determined through the measurement of the intensities of conversion electrons emitted from different atomic shells. Spin-parity assignments can then be made for excited states if that of the ground state is known. The PIN detectors of the GREAT spectrometer are sensitive to

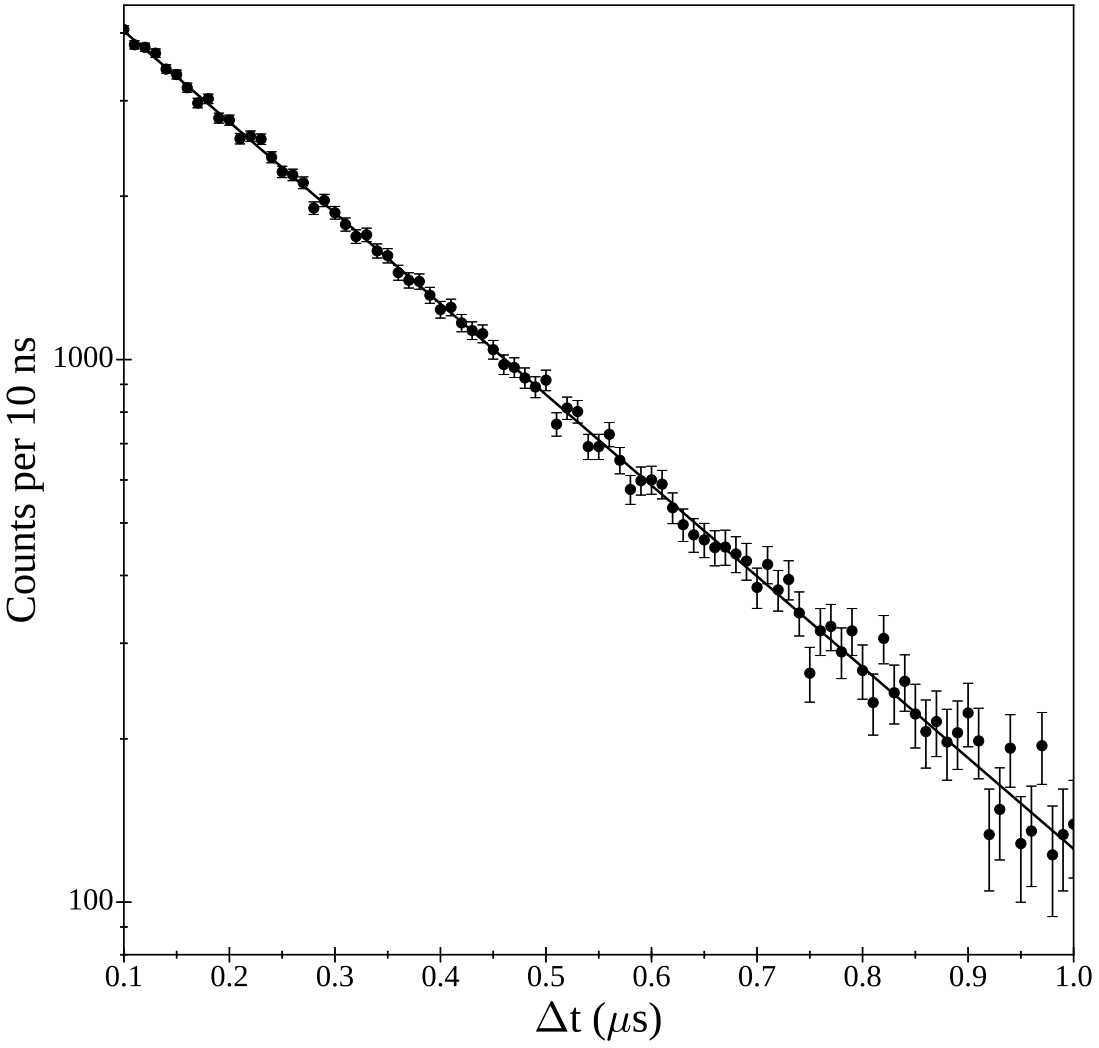

FIGURE 5.10: Decay curve for γ rays of energy 581, 584, 618, 745, 759, 765 or 924 keV in the clover detectors. A constant background has been subtracted.

conversion electrons, however a reliable calibration of these detectors could not be performed in the present analysis due to the non-linear relation between PIN detector channels and energy in the region under consideration. Hence, a direct measurement of the multipolarity of each transition was not always possible.

Nonetheless, the multipolarity of transitions directly depopulating the isomer could be determined by comparison of the measured lifetimes to the lifetimes predicted by Weisskopf single-particle estimates for different multipolarities. The 924 keV transition had previously been assigned as an $E3$ transition by McPeake

[116], who assigned a spin-parity of 19^- to the isomeric state. The lifetime measured in the present analysis is consistent with the Weisskopf estimate for an $E3$ transition. The level fed by the 924 keV transition was previously assigned as 16^+ by Ding *et al.*, hence the assignment of 19^- to the isomer. In the present analysis, Weisskopf estimates suggest that the 581 and 765 keV transitions are $E3$ transitions while the 307 keV transition is assigned as an $M2$ transition.

5.4.2 Multiparticle Configurations

The proton Fermi surface in ^{156}Lu is in the vicinity of the $h_{11/2}$ orbital. Seven valence protons are available above the ^{146}Gd core, which is known to show properties of a doubly magic nucleus [33, 120]. The orbitals available to the three valence neutrons are the $f_{7/2}$, $h_{9/2}$ and $i_{13/2}$ orbitals.

Previously, McPeake assigned a configuration of $\pi h_{11/2}^{-3} \otimes \nu f_{7/2} h_{9/2} i_{13/2}$ to the 19^- isomer [116], analogous to the assignments for the 19^- isomer in ^{152}Ho and in ^{158}Ta [109–111]. The configurations $\pi h_{11/2} \otimes \nu f_{7/2}$ and $\pi h_{11/2} \otimes \nu h_{9/2}$ were also suggested for the 9^+ and 10^+ states, respectively. Possible maximally aligned configurations involving a single $h_{11/2}$ proton coupled to three neutrons in the $f_{7/2}$ and/or the $h_{9/2}$ orbitals are $[\pi h_{11/2} \otimes \nu f_{7/2}^3]13^+$, $[\pi h_{11/2} \otimes \nu f_{7/2}^2 h_{9/2}]16^+$, $[\pi h_{11/2} \otimes \nu h_{9/2}^3]16^+$ and $[\pi h_{11/2} \otimes \nu f_{7/2} h_{9/2}^2]17^+$. The last configuration can form a 16^+ state if the nucleons' angular momenta are not fully aligned. Hence, the three 16^+ states in Fig. 5.5 are accounted for by three of the four maximally aligned configurations.

5.4.3 The 9^+ and 10^+ States

The multipolarity has not been measured for the 62 keV transition, however a tentative spin assignment can be made based on considerations of the character of the possible multipolarities. The 62 keV γ rays are observed in prompt coincidence with the 759 keV transition. Weisskopf estimates suggest that a 62 keV $M1$ transition would be fast enough to provide such coincidences. The intensity of the

62 keV transition calculated under the assumption of an $M1$ transition balances well with the intensity of the 759 keV transition. Therefore an $M1$ assignment is consistent with the observations.

Transitions with a spin change of more than one unit for the 62 keV transition can be excluded as this would most likely result in a delayed decay for such a low transition energy. If the transition is assumed to be an $E1$ transition, the intensity would be a factor of two too low to balance the intensity of the 759 keV transition. A 10^+ assignment for the 62 keV level would mainly decay via an $E0$ transition in the form of conversion electrons, however the angular momentum selection rules allow for weaker γ-ray transitions from the higher multipolarities. In this scenario, the intensity of the γ-ray components would have to match the observed γ-ray intensity. The intensity of the $E0$ conversion electrons would then be even greater, such that the intensity of the transition overall would be too great to balance the intensity of the 759 keV transition. Hence an $M1$ multipolarity is the most compatible assignment for the 62 keV transition.

A stretched $M1$ transition to the 10^+ state can originate from either a 9^+ state or an 11^+ state. The $N = 85$ systematics suggest that an 11^+ state in ^{156}Lu would lie at least 700 keV above the lowest-lying 9^+ state. Transitions between these two states would be observed in Ref.[115] and in the present study. However, if the 62 keV level were an 11^+ state, this would place the 9^+ state at a lower energy than the 10^+ state and would be a poor fit with the systematics shown in Fig. 5.11. Therefore the 62 keV state is unlikely to be 11^+ and is assigned a spin-parity of 9^+.

It is possible that the 62 keV 9^+ state is not the lowest-lying 9^+ state, which could lie just below or within $\sim$ 1 keV of the 10^+ state. In this case, transitions from the 822 keV 11^+ state to the lowest-lying 9^+ state would occur, however no γ rays of $\sim$ 822 keV have been observed.

The assignment of the 62 keV level as the lowest-lying 9^+ state has since been supported by the recent study by Parr *et al.* of α-decay hindrance factors from

high-spin states in ^{156}Lu and ^{158}Ta. The decay of the $\pi h_{11/2}$ coupled state in ^{156}Lu to a $[\pi h_{11/2} \otimes \nu f_{7/2}]_{8^+}$ state was noted to have a greater hindrance factor than the corresponding decays in the isotones ^{152}Ho and ^{158}Ta. This was reasoned to be consistent with the assignment of $[\pi h_{11/2} \otimes \nu h_{9/2}]_{10^+}$ for the α-decaying state in ^{156}Lu in contrast with the α decay of the $[\pi h_{11/2} \otimes \nu f_{7/2}]_{9^+}$ state assigned in ^{152}Ho and ^{158}Ta.

The relative energies of the states below the 19^- isomer in ^{156}Lu have been placed in the energy systematics of the odd-odd $N = 85$ isotones as shown in Fig. 5.11. The energy of the 19^- isomeric state above the lowest-lying 10^+ state is similar to those of the neighbouring isotones, which supports the spin-parity assignment for this level. There is a lowering of the 10^+ state relative to the lowest-lying 9^+ state as protons are added to the $\pi h_{11/2}$ orbital towards $Z = 71$. This has previously been explained as a consequence of the strong attractive interaction between $h_{11/2}$ protons and $h_{9/2}$ neutrons [115]. The order of the lowest-lying 9^+ and 10^+ states is inverted in ^{156}Lu compared to the neighbouring isotopes. Previous measurements of reduced transition probabilities in $N = 82$ isotones have shown that the half filling of the $\pi h_{11/2}$ orbital occurs just below $Z = 71$ [122, 123]. Hence, this inversion appears to be an instance of the interaction being at its strongest in the lutetium isotopes.

5.4.4 Position of the 18^+ State

The results presented here provide clarification of some ambiguities raised in previous studies. Ding *et al.* proposed a level scheme in which the yrast 16^+ state is populated by a 462 keV transition and a 501 keV transition [115]. This places the feeding states lower in energy than the 19^- isomer, in which case transitions from the 19^- isomer to these states become possible. However, no such transitions have been found in this analysis. As noted in Ref. [115], the order of the 501, 731 and 1053 keV transitions in Ding's level scheme is ambiguous due to the similarities

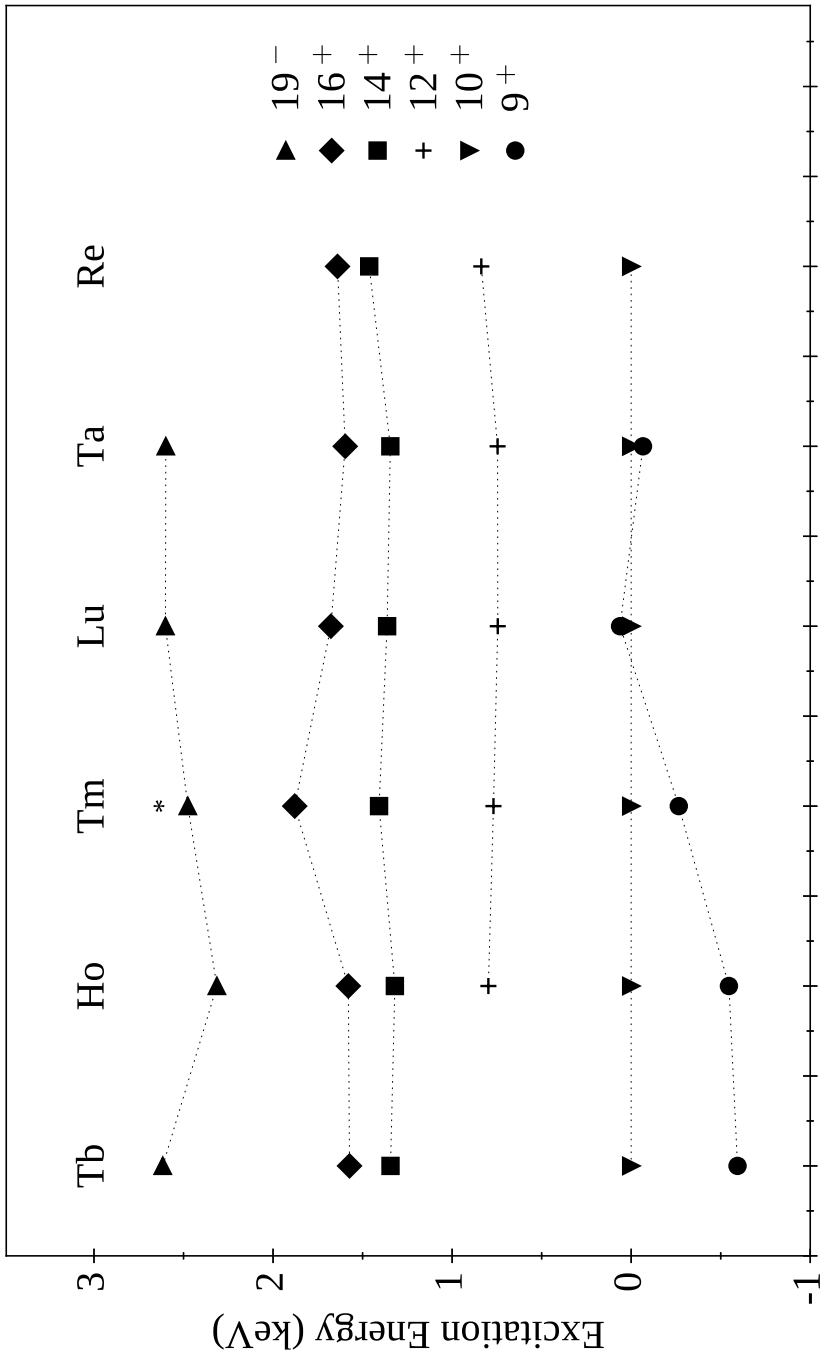

FIGURE 5.11: Systematics of energy levels in the odd-odd $N = 85$ isotones relative to the lowest-lying 10^+ state. The level marked with an asterisk has been proposed as a $(19)^+$ isomer in ^{154}Tm. Dotted lines connect states of the same spin. Data are taken from Refs. [110–113, 115, 121].

in the intensities of these three transitions in the in-beam study. Based on the current analysis, the 1053 keV transition is likely to directly populate the 16^+ state, as this would place the 18^+ state at a greater excitation energy than the 19^- isomer, making the 19^- state an yrast trap.

5.4.5 Reduced Transition Probabilities

Reduced transition probabilities were calculated for the 307 and 924 keV transitions, with values of $B(M2) = 0.73(3)$ W.u. and $B(E3) = 1.22(5)$ W.u., respectively. The value for the 924 keV transition is similar to the values published for the corresponding transitions in the isotones ^{152}Ho ($B(E3) = 0.92(3)$ W.u. for the 734 keV transition [111]) and ^{158}Ta ($B(E3) = 0.101(4)$ W.u. for the 1002 keV transition [109]). It was not possible to accurately determine the $B(E3)$ values for the 581 and 765 keV transitions due to the uncertainty in the branching ratios for these transitions, as explained in section 5.3.1. The quoted reduced transition probabilities for the 307 and 924 keV transitions are based on the assumption that only one of the 581 and 765 keV transitions is a doublet.

5.4.6 Charged-Particle Decay Branches from the 19$^-$ Isomer

Charged-particle decay branches may compete with γ-ray emissions from the 19^- isomer. For an α decay from the 19^- isomer of ^{156}Lu to the 9^+ state in ^{152}Tm [124], the Q_α value would be 8311(4) keV, based on the known E_α value for the 10^+ state [117] and the excitation energy of the 19^- isomer relative to the 10^+ state determined in this work. This Q_α value corresponds to a partial half-life of $\sim$ 2 ms based on the WKB approximation, allowing for a spin change of 11 and assuming a hindrance factor of 5 [109]. A partial half-life of this magnitude equates to an α decay with a branching ratio of $\sim$ 0.01% for the isomer. Any α

decays during the present experiment would not have been observed in the DSSDs due to a strip dead time of 7 μs.

A further possible decay branch is that of a proton decay. The ground state of ^{156}Lu is expected to be bound by 540(80) keV against proton emission [125], in which case the 19$^-$ isomer is expected to be unbound by $\sim$ 2.1 MeV [126]. Despite the large Q_α value, it is unlikely that proton emission from this state would be observed in this experiment since the large orbital angular momentum change and the short half-life would make the branching ratio very low.

5.5 Summary

Gamma-ray transitions linking a 19$^-$ isomer to the yrast 10$^+$ state have been observed in an experiment employing the gas-filled separator RITU in conjunction with the GREAT spectrometer. Electromagnetic decay paths were ascertained based on a γ-ray coincidence analysis. The half-life and the excitation energy of the isomer above the 10$^+$ yrast state have been measured as 179(4) ns and 2601 keV, respectively. Multipolarity assignments have been made for the transitions directly depopulating the isomeric state.

The γ-ray coincidence analysis has established the relative positions of the $[\pi h_{11/2} \otimes \nu f_{7/2}]_{9^+}$ and $[\pi h_{11/2} \otimes \nu h_{9/2}]_{10^+}$ states in ^{156}Lu for the first time. An inversion in the relative ordering of the lowest-lying 9$^+$ and 10$^+$ states is observed when compared to the neighbouring odd-odd isotones, with the 9$^+$ state lying 62 keV above the 10$^+$ state in ^{156}Lu. Hence, it is most likely the 10$^+$ state which α decays in ^{156}Lu, in contrast to the α-decaying 9$^+$ state observed in the other odd-odd isotones. The trend in the odd-odd $N = 85$ isotones of the lowering of the $[\pi h_{11/2} \otimes \nu h_{9/2}]_{10^+}$ state relative to the $[\pi h_{11/2} \otimes \nu f_{7/2}]_{9^+}$ state has previously been interpreted as a consequence of the attractive interaction between $h_{11/2}$ protons and $h_{9/2}$ neutrons. The half filling of the $\pi h_{11/2}$ orbital is expected to occur just below $Z = 71$ [122, 123], therefore the inversion of the lowest-lying 9$^+$ and 10$^+$

states in ^{156}Lu appears to be an instance of the interaction being at its strongest in the lutetium isotopes.

Chapter 6

Conclusions and Future Work

This thesis presents the results of lifetime measurements of excited states in the $\nu i_{13/2}$ band of the transitional nucleus ^{163}W using the recoil-distance Doppler-Shift method, in an experiment using the JUROGAM II γ-ray spectrometer in conjunction with the DPUNS differential plunger device. The lifetimes of the $17/2^+$ and $21/2^+$ levels have been measured to be $\tau = 22(2)$ ps and $\tau = 3.0(4)$ ps, respectively. An upper limit for the lifetime of the $25/2^+$ level of $\tau \leq 3.9(7)$ ps was also measured. $B(E2)$ reduced transition probabilities have been extracted from the lifetimes.

The $B(E2)$ ratios in ^{163}W were found to be consistent with the expectations of the collective model. The result can be understood as a consequence of the polarising effects of the unpaired neutron. The occupation of high-j, low-Ω orbitals by the unpaired neutron leads to the adoption of an axially symmetric prolate shape with an average K of zero, reproducing the conditions described by the collective model.

The result for ^{163}W is in sharp contrast to the apparently anomalous $B(E2)$ ratios of the nearby even-N isotope ^{166}W [20]. The conditions for γ-soft deformations occur in the even-even $N \sim 90$ tungsten isotopes. Previously measured $E(4^+)/E(2^+)$ ratios for these isotopes are consistent with the ratios predicted for

γ-soft rotors [15]. The $E_s/E(2_1^+)$ systematics for the light tungsten isotopes also suggest that the ^{162,164,166}W nuclides have γ-soft deformations [96]. The $B(E2)$ ratios of γ-soft nuclei may not follow the collective model, as $B(E2)$ values are sensitive to the nuclear geometry and K is poorly defined for triaxial deformations. It has been proposed that the anomalous $B(E2)$ ratios in ^{166}W are due to the triaxial geometry of the nuclide. This explanation may also apply to anomalous $B(E2)$ ratios measured in other nearby osmium and platinum transitional nuclei.

Experiments are currently being planned in which the lifetimes of excited states in ^{162}W and ^{164}W will be measured. The recently developed Triple-foil differential Plunger for lifetime measurements of excited states in Exotic Nuclei (TPEN) [127] will provide a means of reducing the experimental errors of the previously measured lifetimes of the 2^+ states in these nuclides [77]. The measurement of further yrast states in these nuclides would allow $B(E2)$ ratios to be extracted, testing the expectation that these nuclides will have anomalous $B(E2)$ ratios. The hypothesised geometrical origin of anomalous $B(E2)$ ratios in nearby even-even nuclei could also act as a test for the predictions of fully self-consistent mean field models that do not assume axial symmetry.

This work also presents the results of spectroscopic measurements of an isomeric decay in ^{156}Lu. Gamma-ray transitions linking a 19^- isomer to the yrast 10^+ state have been observed in an experiment employing the gas-filled separator RITU in conjunction with the GREAT spectrometer. Electromagnetic decay paths were determined based on a γ-ray coincidence analysis. The half-life and the excitation energy of the isomer above the 10^+ yrast state have been measured as 179(4) ns and 2601 keV, respectively.

The γ-ray coincidence analysis has established the relative positions of the $[\pi h_{11/2} \otimes \nu f_{7/2}]_{9^+}$ and $[\pi h_{11/2} \otimes \nu h_{9/2}]_{10^+}$ states in ^{156}Lu for the first time. An inversion in the relative ordering of the lowest-lying 9^+ and 10^+ states is observed when compared to the neighbouring odd-odd isotones, with the 9^+ state lying 62 keV above the 10^+ state in ^{156}Lu. Hence, it is most likely the 10^+ state which

α decays in ^{156}Lu, in contrast to the α-decaying 9^+ state observed in the other odd-odd isotones. The trend in the odd-odd $N = 85$ isotones of the lowering of the $[\pi h_{11/2} \otimes \nu h_{9/2}]_{10^+}$ state relative to the $[\pi h_{11/2} \otimes \nu f_{7/2}]_{9^+}$ state has previously been interpreted as a consequence of the attractive interaction between $h_{11/2}$ protons and $h_{9/2}$ neutrons. The half filling of the $\pi h_{11/2}$ orbital is expected to occur just below $Z = 71$ [122, 123], therefore the inversion of the lowest-lying 9^+ and 10^+ states in ^{156}Lu appears to be an instance of the interaction being at its strongest in the lutetium isotopes.

The nuclides ^{163}W and ^{156}Lu studied in this thesis display markedly different γ-ray spectra, each of which can be broadly understood by considering the collective model [7] and the shell model [2–4]. However, trends across the neighbouring nuclei require a deeper understanding. The $B(E2)$ ratios in ^{163}W were found to be consistent with the collective model, which was in contrast to those measured previously in ^{166}W [20]. A more detailed consideration of the geometry of these nuclides provides an explanation for this behaviour. Likewise, the shell model alone was insufficient to explain the behaviour of the lowest-lying 9^+ and 10^+ states in the odd-odd $N = 85$ isotones. It was by considering the interaction between $h_{11/2}$ protons and $h_{9/2}$ neutrons that this behaviour could be understood. This thesis has therefore demonstrated the importance of the nuclear geometry and of nucleon-nucleon interactions in understanding the properties of heavy nuclei.

Bibliography

[1] E. Rutherford, Lond. Edinb. Dubl. Phil. Mag. **21**, 669 (1911).

[2] M. G. Mayer, Phys. Rev. **74**, 235 (1948).

[3] M. G. Mayer, Phys. Rev. **78**, 16 (1950).

[4] M. G. Mayer, Phys. Rev. **78**, 22 (1950).

[5] N. Bohr, Lond. Edinb. Dubl. Phil. Mag. **26**, 1 (1913).

[6] E. Schrödinger, Ann. Phys. (Berlin) **386**, 109 (1926).

[7] A. Bohr and B. R. Mottelson, *Nuclear Structure Volume 2: Nuclear Deformation* (W. A. Benjamin Inc, New York, USA, 1975).

[8] Y. S. Chen, S. Frauendorf, and G. A. Leander, Phys. Rev. C **28**, 2437 (1983).

[9] S. G. Nilsson and I. Ragnarsson, *Shapes and Shells in Nuclear Structure* (Cambridge University Press, 1995).

[10] F. Crespi *et al.*, Nucl. Instrum. Meth. A **620**, 299 (2010).

[11] P. Lecoq *et al.*, IEEE Trans. Nucl. Sci **57**, 2411 (2010).

[12] A. Dewald, O. Möller, and P. Petkov, Prog. Part. Nucl. Phys. **67**, 786–839 (2012).

[13] D. T. Joss *et al.*, Phys. Rev. C **93**, 024307 (2016).

[14] J. Simpson *et al.*, J. Phys. G **18**, 1207 (1992).

[15] A. Arima and F. Iachello, Ann. Rev. Nucl. Part. Sci. **31**, 75 (1981).

[16] K. Lagergren *et al.*, Phys. Rev. C **83**, 014313 (2011).

[17] M. Sandzelius *et al.*, Phys. Rev. C **80**, 054316 (2009).

[18] T. R. Davis-Merry *et al.*, Phys. Rev. C **91**, 034319 (2015).

[19] T. Grahn *et al.*, Phys. Rev. C **94** (2016), 044327.

[20] B. Sayğı *et al.*, Phys. Rev. C **96**, 021301 (2017).

[21] B. Cederwall *et al.*, Phys. Rev. Lett **121**, 022502 (2018).

[22] P. Bringel *et al.*, Eur. Phys. J. A **24**, 167 (2005).

[23] D. Jensen *et al.*, Nucl. Phys. A **703**, 3 (2002).

[24] G. Schönwaßer *et al.*, Phys. Lett. B **552**, 9 (2003).

[25] H. Amro *et al.*, Phys. Lett. B **553**, 197 (2003).

[26] S. Törmänen *et al.*, Phys. Lett. B **454**, 8 (1999).

[27] P. Bringel *et al.*, Eur. Phys. J. A **16**, 155 (2003).

[28] H. Schnack-Petersen *et al.*, Nucl. Phys. A **594**, 175 (1995).

[29] W. Schmitz *et al.*, Nucl. Phys. A **539**, 112 (1992).

[30] W. Schmitz *et al.*, Phys. Lett. B **303**, 230 (1993).

[31] S. A. Giuliani *et al.*, Rev. Mod. Phys. **91**, 011001 (2019).

[32] R. Broda *et al.*, Phys. Rev. Lett. **74**, 868 (1995).

[33] M. Ogawa *et al.*, Phys. Rev. Lett. **41**, 289 (1978).

[34] M. G. Mayer, Phys. Rev. **75**, 1969 (1949).

[35] O. Haxel, J. H. D. Jensen and H. E. Suess, Phys. Rev. **75**, 1766 (1949).

[36] R. D. Woods and D. S. Saxon, Phys. Rev. **95**, 577 (1954).

[37] S. G. Nilsson, Kgl. Danske Videnskab. Selskab, Mat-fys. Medd. **29**, 16 (1955).

[38] K.E.G. Löbner and M. Vetter and V. Hönig, Atom. Data Nucl. Data Tabl. **7**, 495 (1970).

[39] F.S. Stephens, Rev. Mod. Phys. **47**, 43 (1975).

[40] F. S. Stephens, R. M. Diamond, J. R. Leigh, T. Kammuri, and K. Nakai, Phys. Rev. Lett. **29**, 438 (1972).

[41] F. Stephens, R. Diamond, and S. Nilsson, Phys. Lett. B **44**, 429 (1973).

[42] D.L. Hill and J.A. Wheeler, Phys. Rev. **89**, 1102 (1953).

[43] G. Andersson *et al.*, Nucl. Phys. A **268**, 205 (1976).

[44] K. S. Krane, *Introductory Nuclear Physics* (John Wiley & Sons, 1988).

[45] J. M. Blatt and V. F. Weisskopf, *Theoretical Nuclear Physics* (Dover Publications Inc, New York, USA, 1952).

[46] M. A. Bentley *et al.*, Phys. Rev. Lett. **59**, 2141 (1987).

[47] G. Gamow, Z. Phys. **51**, 204 (1928).

[48] R. W. Gurney and E. U. Condon, Nature **122**, 439 (1928).

[49] N. Bohr, Nature **137**, 344 (1936).

[50] C. W. Beausang and J. Simpson, J. Phys. G: Nucl. Part. Phys. **22**, 527 (1996).

[51] G. Duchêne *et al.*, Nucl. Instrum. Methods Phys. Res. A **432**, 90 (1999).

[52] M. Leino *et al.*, Phys. Res. B **99**, 653 (1995).

[53] B. L. Cohen and C. B. Fulmer, Nucl. Phys. **6**, 547 (1958).

[54] R. D. Page *et al.*, Nucl. Instrum. Methods. Phys. Res. B **204**, 634 (2003).

[55] I. H. Lazarus *et al.*, IEEE Trans. Nucl. Sci. **48**, 567 (2001).

[56] E. S. Paul *et al.*, Phys. Rev. C **51**, 78 (1995).

[57] L. Cleemann, J. Eberth, W. Neumann, N. Wiehl, and V. Zobel, Nucl. Instrum. Methods **156**, 477 (1978).

[58] M. J. Taylor *et al.*, Nucl. Instrum. Methods. Phys. Res. A **707**, 143 (2013).

[59] A. Z. Schwarzschild and E. K. Warburton, Ann. Rev. Nucl. Sci. **18**, 265 (1968).

[60] A. Dewald, S. Harissopulos, and P. von Brentano, Z. Phys. A **334**, 163 (1989).

[61] G. Böhm, A. Dewald, P. Petkov, and P. von Brentano, Nucl. Instrum. Methods. Phys. Res. A **329**, 248 (1993).

[62] S. Harissopulos *et al.*, Nucl. Phys. A **467**, 528 (1987).

[63] G. Goldring, *Heavy Ion Collisions* Vol. 3 (North-Holland, Amsterdam, 1982).

[64] P. Petkov *et al.*, Nucl. Phys. A **589**, 341 (1995).

[65] P. Petkov *et al.*, Nucl. Phys. A **543**, 589 (1992).

[66] P. Petkov, A. Dewald, and P. von Brentano, Nucl. Instrum. Methods. Phys. Res. A **457**, 527 (2001).

[67] D. T. Joss *et al.*, Phys. Lett. B **772**, 703 (2017).

[68] N. Alkhomashi *et al.*, Phys. Rev. C **80**, 064308 (2009).

[69] J. Simpson, M. A. Riley, A. Alderson, M. A. Bentley, A. M. Bruce, D. M. Cullen, P. Fallon, F. Hanna, and L. Walker, J. Phys. G **17**, 511 (1991).

[70] K. Theine *et al.*, Nucl. Phys. A **548**, 71 (1992).

[71] G. D. Dracoulis *et al.*, Proceedings of the International Conference on Nuclear Structure at High Angular Momentum, Ottawa, AECL Report No. 10613 (unpublished) **2**, p. 94 (1992).

[72] C. Scholey *et al.*, Phys. Rev. C **81**, 014306 (2010).

[73] J. Thomson *et al.*, Phys. Rev. C **81**, 014307 (2010).

[74] A. Gavron, Phys. Rev. C **21**, 230 (1980).

[75] O.B. Tarasov and D. Bazin, Nucl. Instrum. Methods. Phys. Res. B **266**, 4657 (2008).

[76] Pace4, http://lise.nscl.msu.edu/pace4.

[77] M. Doncel *et al.*, Phys. Rev. C **95**, 044321 (2017).

[78] C. M. Baglin, Nucl. Data. Sheets **111**, 1807 (2010).

[79] C. M. Baglin, E. A. McCutchan and S. Basunia, Nucl. Data. Sheets **153**, 1 (2018).

[80] B. Singh, Nucl. Data. Sheets **75**, 199 (1995).

[81] E. Browne and Huo Junde, Nucl. Data. Sheets **87**, 15 (1999).

[82] J. M. Regis *et al.*, Nucl. Instrum. Methods. Phys. Res. A **606**, 466 (2009).

[83] M. Rudigier, J.-M. Régis, J. Jolie, K. Zell, and C. Fransen, Nucl. Phys. A **847**, 89 (2010).

[84] E. A. McCutchan, Nucl. Data. Sheets **126**, 151 (2015).

[85] B. Singh, Nucl. Data. Sheets **130**, 21 (2015).

[86] C. M. Baglin, Nucl. Data. Sheets **111**, 275 (2010).

[87] C. M. Baglin, Nucl. Data. Sheets **99**, 1 (2003).

[88] C. B. Li *et al.*, Phys. Rev. C **94**, 044307 (2016).

[89] A. Keenan *et al.*, Phys. Rev. C **63** (2001).

[90] Data extracted using the NNDC On-Line Data Service from the ENSDF database, file revised as of 15 Mar 2019. M. R. Bhat, *Evaluated Nuclear Structure Data File (ENSDF), Nuclear Data for Science and Technology*, page 817, edited by S. M. Qaim (Springer-Verlag, Berlin, Germany, 1992).

[91] B. Sayğı, *Anomalous $B(E2)_{4^+/2^+}$ Ratios in the Neutron-Deficient Nuclide ^{168}Os and ^{166}W*, PhD thesis, Department of Physics, University of Liverpool. Available at ⟨http://repository.liv.ac.uk/15355/4/SaygiBah_Sep2013_15355.pdf⟩ [Accessed 19/09/2016], 2013.

[92] G. Alaga, K. Alder, A. Bohr and B.R. Mottelson, Dan. Mat. Fys. Medd. **29**, 1 (1955).

[93] T. Kibedi, G.D. Dracoulis, A.P. Byrne, and P.M. Davidson, Nucl. Phys. A **688**, 669 (2001).

[94] A. S. Davydov and G. F. Filippov, Nucl. Phys. B **8**, 237 (1958).

[95] L. Wilets and M. Jean, Phys. Rev. **102**, 788 (1956).

[96] Q. Yang, H.-L. Wang, M.-L. Liu, and F.-R. Xu, Phys. Rev. C **94**, 024310 (2016).

[97] A. Davydov and V. Rostovsky, Nuclear Physics **12**, 58 (1959).

[98] S. SHARMA and R. Kaushik, Test of asymmetry rotor model for the b(e2; 4g→2g)/ b(e2;2g→0g) branching ratio in medium mass region, 2015.

[99] T. Kibédi, G. D. Dracoulis, B. Fabricius, A. P. Byrne, and A. E. Stuchbery, Nucl. Phys. A **539**, 137 (1992).

[100] R. A. Bark *et al.*, Nucl. Phys. A **591**, 265 (1995).

[101] T. Venkova *et al.*, Z. Phys. A **334**, 385 (1989).

[102] F.G. Kondev, G.D. Dracoulis, A.P. Byrne, M. Dasgupta, T. Kibédi, and G.J. Lane, Nucl. Phys. A **601**, 195 (1996).

[103] D.E Archer *et al.*, Phys. Rev. C **52**, 1326 (1995).

[104] R. Bengtsson, and S. Frauendorf, Nucl. Phys. A **327**, 139 (1979).

[105] F. Dönau and S. Frauendrof, Proceedings of the Conference on High Angular Momentum Properties of Nuclie, Oak Ride, 1982, edited by N. R. Johnson (Harwood Academic, New York) , 143 (1983).

[106] F. Dönau, Nucl. Phys. A **471**, 469 (1987).

[107] L. Barber *et al.*, Submitted to Phys. Rev. Lett. (2019).

[108] G.D. Dracoulis, P.M. Walker, and F.G. Kondev, Rep. Prog. Phys. **79**, 076301 (2016).

[109] R. J. Carroll *et al.*, Phys. Rev. Lett. **112**, 092501 (2014).

[110] R. J. Carroll *et al.*, Phys. Rev. C **93**, 034307 (2016).

[111] S. André *et al.*, Nucl. Phys. A **575**, 155 (1994).

[112] C. Foin *et al.*, Eur. Phys. J. A **14**, 7 (2002).

[113] P. J. Sapple *et al.*, Phys. Rev. C **84**, 054303 (2011).

[114] P. Kemnitz, L. Funke, E. Will, and G. Winter, Phys. Scr. **24**, 253 (1981).

[115] K. Y. Ding *et al.*, Phys. Rev. C **64**, 034315 (2001).

[116] C. G. McPeake, *Excited states in the exotic nuclei* ^{156}Lu *and* ^{158}Lu, PhD thesis, Department of Physics, University of Liverpool. Available at ⟨http://livrepository.liverpool.ac.uk/3007704/⟩ [Accessed 28/03/2016], 2017.

[117] R. D. Page *et al.*, Phys. Rev. C **53**, 660 (1996).

[118] J. A. Bearden, Rev. Mod. Phys. **39**, 78 (1967).

[119] C. N. Davids *et al.*, Phys. Rev. C **55**, 2255 (1997).

[120] P. Kleinheinz, S. Lunardi, M. Ogawa, and M. R. Maier, Z. Phys. A **284**, 351 (1978).

[121] G. Duchêne *et al.*, Z. Phys. A **350**, 39 (1994).

[122] J. H. McNeill *et al.*, Phys. Rev. Lett. **63**, 860 (1989).

[123] J. H. McNeill *et al.*, Z. Phys. A **344**, 369 (1993).

[124] J. McNeill *et al.*, Z. Phys. A **325**, 27 (1986).

[125] G. Audi *et al.*, Chinese Phys. C **36**, 1157 (2012).

[126] R. D. Page, Phys. Rev. C **83**, 014305 (2011).

[127] M. Giles *et al.*, Nucl. Instrum. Meth. A **923**, 139 (2019).